

DISSERTATION

Coincidence measurements of electrons emitted from solid surfaces irradiated with electrons, photons and ions

ausgeführt zum Zwecke der Erlangung des akademischen Grades eines Doktors
der technischen Wissenschaften unter der Leitung von

Dr. Wolfgang Werner

134

Institut für Allgemeine Physik

eingereicht an der Technischen Universität Wien

Fakultät für Physik

von

Dipl. Ing. Werner Smekal

9325866

Weinberggasse 12/12, 2100 Leobendorf

Wien, am 29. Oktober 2007

Kurzfassung

Bei der Elektronenkoinzidenzspektroskopie an Oberflächen wird die Energie und die Emissionsrichtung von emittierten Elektronen von zwei Spektrometern gemessen. Die Elektronen werden dabei auf Grund der Anregung durch Photonen-, Elektronen- oder Ionenbeschuss emittiert. Durch die zusätzliche Aufzeichnung der Ankunftszeiten der Elektronen in den beiden Spektrometern ist es möglich, korrelierte Elektronenemission zu studieren. Hierdurch eröffnet sich ein neues Feld der Elektronenspektroskopie, wobei vor allem die Elektronenstruktur in Festkörpern, wie auch der Emissionsprozess der Elektronen untersucht werden können.

Im Rahmen dieser Disseration wurden Koinzidenzexperimente bei photonen-, elektronen- und ioneninduzierter Elektronenemission durchgeführt:

- Bei der Auger-Photoelectron coincidence spectroscopy (APECS) werden Auger-elektronen und Photoelektronen, welche im selben Photoionisationsprozess entstanden sind, in Koinzidenz gemessen. Dabei können die Elektronenzustände während der Photoionisation, Satellitenstrukturen und Shake-up und Shake-Down Prozesse genauer untersucht werden.

Gegenüber der gewöhnlichen Elektronenspektroskopie kann bei APECS eine verstärkte Oberflächensensitivität festgestellt werden. Das folgt daraus, dass bei einem Koinzidenzevent das Auger- wie auch das Photoelektron den Festkörper verlassen müssen, ohne dass diese inelastisch gestreut werden, wobei die Wahrscheinlichkeit dafür mit der Tiefe empfindlich sinkt.

Um die Oberflächensensitivität von APECS genauer zu untersuchen, wurden am Synchrotron in Triest (ELETTRA) Koinzidenzmessungen durchgeführt. Hierbei wurde der Si-2*p* Photopeak mit dem Si-LVV Augerpeak und mit inelastisch gestreuten Si-LVV Augerelektronen in Koinzidenz gemessen. Die experimentellen Resultate wurden mit einem theoretischen Modell verglichen. Dabei wurde gezeigt, dass man die Entstehungstiefe der einzelnen Photoelektronen selektieren kann, indem man sie in Koinzidenz mit Augerlelektronen, die einen gewissen Energieverlust erfahren haben, misst.

- Sekundärelektronen (SE) sind langsame (< 50 eV) Elektronen, die von einem Festkörper emittiert werden, wenn dieser mit Elektronen, Photonen oder Ionen bestrahlt wird. Die SE werden entweder direkt durch die einfallende Strahlung erzeugt oder bei der darauffolgenden Kaskade. In vielen Gebieten in der Physik, wie z.B. Sekundärelektronenmikroskopie, Kernfusion oder Raumfahrttechnik, ist ein genaues Verständnis der Emission der SE und deren Eigenschaft sehr wichtig. Auf Grund der komplizierten Theorie der SE und der schwierigen Experimente, um die SE zu vermessen, ist auf dem Gebiet der SE noch viel zu erforschen.

Die Energie- und Impulsdichten von Festkörperelektronen können mittels ($e, 2e$)-Koinzidenzspektroskopie untersucht werden, bei der reflektierte und emittierte

Elektronen in Koinzidenz gemessen werden. Dabei kann man auch die SE-Emission genauer untersuchen. Bei dem hier beschriebenen Experiment wurde der Zerfall von Plasmonen in Al (100)-Einkristallen untersucht, indem SE mit rückgestreuten Elektronen, die über einen inelastischen Stoß Energie verloren haben, koinzident vermessen wurden. Der Al (100)-Einkristall war auf Grund seiner ausgeprägten Struktur im inelastischen Bereich des rückgestreuten Energiespektrums ausgewählt worden.

Aus der Position und Struktur der Peaks in den so erhaltenen Koinzidenzspektren kann der Schluss gezogen werden, dass die emittierten SE hauptsächlich aus dem Zerfall von Oberflächen- und Volumsplasmonen stammen, die jeweils in einzelne Elektron-Lochpaare zerfallen. Nur ein kleiner Teil der emittierten SE sind auf Grund der SE-Kaskade entstanden.

Um den SE-Emissionsprozess für Materialien mit komplizierterer Elektronenstruktur als Al (100) zu entschlüsseln, muss man das SE-Spektrum mit einer Vielzahl an Verlustenergien von 0 bis ~ 50 eV in Koinzidenz messen. Da ein konventionelles Koinzidenzspektrometer alleine für eine Koinzidenzmessung mit einer Verlustenergie über ein Monat benötigt, müssen neue experimentelle Strategien entwickelt werden, die das beschriebene Vorhaben ermöglichen.

- Elektronenemission aus Festkörpern durch Ionenbeschuss ist wesentlich schwerer zu beschreiben, da die Ionenstruktur im Vergleich zu Elementarteilchen wie Photonen oder Elektronen sehr kompliziert ist. Man unterscheidet dabei zwei Prozesse, die zur Emission von Elektronen führen: der kinetische Emissionsprozess (KE) und der Potentialemissionsprozess (PE). Der KE kann dabei nur auf die kinetischen Eigenschaften der einfallenden Ionen zurückgeführt werden, wohingegen die PE auf das Coulombpotential des Ions basiert.

Diese Prozesse wurden mittels eines neu konstruierten Magnetfeld-Flugzeit Elektronenspektrometers untersucht. Das Spektrometer ist in der Lage den Impuls der emittierten Elektronen zu ermitteln, womit die emittierten Elektronen vollständig bestimmt werden. Weiters kann das Spektrometer die Eigenschaften von bis zu 14 Elektronen pro Puls bestimmen, wodurch Elektronenkoinzidenzexperimente ermöglicht werden. Die Hemisphäre über der der Probe wird auf einen (kreisrunden) MCP-Detektor abgebildet, wodurch im Prinzip jedes emittierte Elektron erfasst wird, was zu einer beträchtlichen Steigerung der Koinzidenzrate führt, welche bei herkömmlichen Koinzidenzmessungen limitierend gering sein kann (typischerweise 0.1–0.001 Hz). Dieses Spektrometer wurde "Momentum Vector Electron Spectrometer" benannt und wird in dieser Arbeit genau beschrieben.

Für die Experimente musste auch eine Ionenquelle konstruiert werden, die in der Lage ist, ultrakurze Pulse zu erzeugen. Dabei wird ein kontinuierlicher Strahl einer thermionischen Cs⁺-Ionenkanone mittels elektrischer Felder über eine Blende gelenkt um Nanosekundenpulse zu erzeugen. Bei ersten Testversuchen wurde die Cs⁺ induzierte Elektronenemission von einer polykristallinen Goldprobe untersucht.

Abstract

In electron coincidence spectroscopy of solid surfaces energy and emission direction of emitted electrons are commonly measured by two spectrometers. The emission of electrons can be induced by either photons, electrons or ions. The time of arrival of the electrons in the spectrometers is recorded by high resolution timing electronics. In this way, it is possible to study correlated electron emission. This opens new fields of applications in electron spectroscopy, especially regarding the electron band structure in solids and electron emission processes.

In this work coincidence spectroscopy experiments for photon-, electron- and ion-induced emission of electrons were conducted:

- In Auger-Photoelectron coincidence spectroscopy (APECS) an Auger and a photoelectron created in the same ionization process are measured in coincidence. Such coincidence experiments therefore provide deeper insight into initial and final state effects, satellite structures, shake-up and shake-down processes and other effects.

One of the most interesting properties of APECS is the enhanced surface sensitivity compared to conventional non-coincident spectra. This is easy to understand, since for a coincidence event both the Auger and photoelectron need to escape the solid without being inelastically scattered. The possibility that this happens for an ionization event decreases rapidly with the depth.

At the synchrotron in Trieste (ELETTRA) coincidence measurements were conducted in order to investigate the enhanced surface sensitivity of APECS. The Si-2*p* photopeak was measured in coincidence with the Si-LVV Augerpeak as well as its inelastic features and the results were compared to a theoretical model. It was proven that if photoelectrons are measured in coincidence with Augerelectrons that have lost a certain fraction of their original energy, one can select the depth range of individual photoelectrons.

- Electrons emitted from a solid due to irradiation of electrons or ions are referred to as "Secondary electrons". Secondary electrons (SE) can either be excited directly by the incident radiation or due to the following collision cascade.

Furthermore, many other fields in physics like secondary electron microscopy, nuclear fusion, or space technology depend on the knowledge of SE emission and their properties. Hence, it is of vital interest to gain more insight in the field of SE. Due to the involved theory of the excitation and transport of SE and difficult experimental aspects for the energy range of SE, the physics of SE is still a challenging field.

(*e, 2e*) coincidence spectroscopy experiments are a suitable technique to improve the understanding of the SE emission process. (*e, 2e*) coincidence spectroscopy enables one to measure electron energy-momentum densities in solid targets by measuring the reflected electrons and the excited electrons in coincidence.

To investigate the decay of electron excited plasmons in an Al (100) single crystal SE were measured in coincidence with the inelastic features of the elastic peak. The Al (100) single crystal was chosen due its pronounced features in the inelastic tail of the elastic peak. An apparatus developed at the Department of Physics of the Università di Roma Tré was used to conduct these $(e, 2e)$ -experiments.

The shape and position of the peaks in the resulting coincidence spectra of the SE and from comparison of Monte Carlo simulations to experimental results directly demonstrate, that the SE emitted from the solid stem from surface and bulk plasmons which decay into single electron-hole pairs. Only a small part of the spectra can be attributed to electrons excited by the collision cascade of secondary electrons.

For materials with a more complicated electronic structure as Al (100), unravelling the secondary electron emission process would imply coincident energy resolved measurements of the secondary electron spectrum, for many loss energies from 0 to ~ 50 eV. With a conventional coincidence spectrometer with two separate analyzers acquiring the required statistics at *one* loss energy takes about a *month* of net measurement time. Therefore, new experimental approaches need to be developed in order to achieve the stated goal.

- The underlying processes of the ion-solid interaction which leads to electron emission are very complicated due to the structure of the ion compared to the fundamental particles like photons or electrons. Two different processes which lead to electron emission due to ion–solid interactions are described: the kinetic emission (KE) and the potential emission (PE) process. KE is caused purely by the kinetic properties of the incoming projectile. PE on the other hand is due to the Coulomb potential of the incoming ion.

In order to study these emission processes a new kind of magnetic–field time–of–flight electron spectrometer was designed and built in the process of this thesis. This spectrometer is able to determine the momenta of the emitted electrons from a solid surface and is therefore kinematically complete. Since the spectrometer consists of a detector with a solid angle of detection of 2π for up to 14 emitted electrons, coincidence measurements with unprecedented high coincidence count rates are achievable in this way. This spectrometer is called “Momentum Vector Electron Spectrometer” and the aspects of this spectrometer are presented in this thesis in great detail.

In addition, an ultra–short pulsed ion source had to be designed and built as well. Here, a Cs^+ thermionic ion gun was chosen as ion source. The continuous ion beam was chopped by a electric–field ion chopper in order to produce nano–second pulses. For first test experiments a polycrystalline Au sample was chosen to investigate Cs^+ induced electron emission on Au.

Contents

Kurzfassung	I
Abstract	III
1. Auger Photoelectron Coincidence Spectroscopy on Silicon	3
1.1. Theory of APECS	4
1.1.1. The photoionization process	4
1.1.2. The Auger process	5
1.1.3. Principles of APECS	7
1.1.4. Surface sensitivity of APECS	7
1.1.5. Considerations about the coincidence rate	12
1.2. Emission–Depth–Selective APECS	16
1.2.1. Experimental aspects	16
1.2.2. ALOISA Beamline at ELETTRA	18
1.2.3. Experiments and results	19
2. Electron induced Electron Emission from Surfaces	24
2.1. Emission of secondary electrons	25
2.2. (e,2e)-coincidence spectroscopy	29
2.3. Experiment	33
2.4. Results	36
2.5. Comparison to Monte Carlo simulation	37
2.6. Summary	39
3. Ion induced Emission of Electrons from Surfaces	41
3.1. Theory of ion–induced electron emission	42
3.1.1. Kinetic emission	42
3.1.2. Potential emission	47
3.1.3. Energy distribution of the emitted electrons	50
3.1.4. Influence of surface contamination	51
3.2. General considerations about electron coincidence experiments with ion pulses	51
3.2.1. Ion pulse generation	51
3.2.2. True and false coincidences	52
3.3. Aspects and Design of the Momentum Vector Electron Spectrometer	55
3.3.1. Principle of Operation	55

3.3.2.	Specifications	57
3.3.3.	Creation of the axial magnetic field	59
3.3.4.	Compensation of the earth magnetic field and noise	62
3.3.5.	Creation of the axial electric field	64
3.3.6.	Electron trajectories in the spectrometer	65
3.3.7.	Determination of the electron momentum	67
3.3.8.	Energy- and Angle Resolution	71
3.3.9.	Transmission Function	72
3.4.	Analysis of recorded Data	82
3.4.1.	Resort algorithm	82
3.4.2.	Calibration of detector parameters	89
3.4.3.	Determination of the time of ion-solid impact	91
3.4.4.	Determination of the spectrometer axis	96
3.4.5.	Influence of misalignment between magnetic and electric field - the $\mathbf{E} \times \mathbf{B}$ drift	98
3.5.	Aspects and Design of a Pulsed Ion Source	99
3.5.1.	Principle of Operation	99
3.5.2.	Specifications	99
3.5.3.	Time resolution of Ion Pulses	100
3.6.	First Experiments with MoVES	109
3.6.1.	Cs^+ induced electron emission from a Au surface	109
4.	Conclusions and Outlook	114
A.	Acknowledgement	116
B.	Acronyms	117
C.	Curriculum vitae	118

1. Auger Photoelectron Coincidence Spectroscopy on Silicon

In APECS [38, 37] an Auger and a photoelectron which were created in the same ionization process are measured in coincidence. Such coincidence experiments therefore provide deeper insight into initial and final state effects, satellite structures, shake-up and shake-down processes and other effects.

One of the most interesting properties of APECS is the enhanced surface sensitivity compared to conventional non-coincident spectra. This is easy to understand, since for a coincidence event both the Auger and photoelectron need to escape the solid without being inelastically scattered. The possibility that this happens for an ionization event decreases rapidly with the depth.

In the following sections a theory is described which is mainly concerned about the surface sensibility and also addresses multiple elastic scattering effects. A general quantification model for surface sensibility in electron spectroscopy is presented and extended to APECS [111].

At the synchrotron in Trieste (ELETTRA) [35] coincidence measurements were conducted in order to investigate the enhanced surface sensitivity of APECS. The Si-2*p* photopeak was measured in coincidence with the Si-LVV Augerpeak as well as its inelastic features and the results were compared to a theoretical model. It was proven that if photoelectrons are measured in coincidence with Augerelectrons that have lost a certain fraction of their original energy, one can select the depth range of individual photoelectrons.

1.1. Theory of APECS

1.1.1. The photoionization process

X-ray photoelectron spectroscopy (XPS) is based on the phenomenon of photoemission which was detected by Hertz [45] in 1887. Hertz basically illuminated samples with electromagnetic radiation and measured the voltage needed to suppress the electric current which would flow otherwise. Hertz discovered that there is a direct proportionality between the frequency of the radiation and the voltage, which corresponds to the kinetic energy of the electrons emitted from the surface. In contradiction to the classical picture of this experiment the intensity of the incoming radiation had no influence on the voltage applied. In 1905 Einstein [29] was able to explain the systematic of this process by taking the quantum nature of light into consideration.

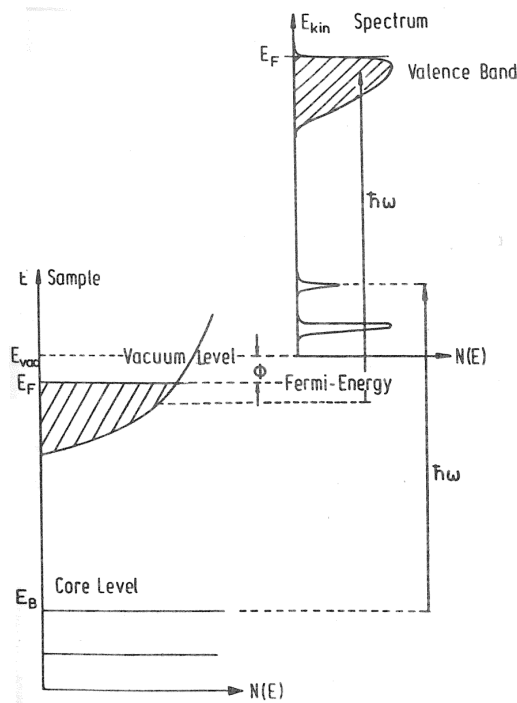


Figure 1.1: Schematic drawing which shows the relation between the energy levels in the solid (in this case a metal) and energy distribution of the electrons emitted due to photons of the energy $h\nu$. The kinetic energy E_{kin} of the electrons is zero at the vacuum level of the sample. Alternatively one can use the so-called binding energy of the electrons E_b , which in solids is generally referred to the Fermi level and in free atoms to the vacuum level. For the emitted electrons the photoelectric equation $E_{kin} = h\nu - E_b(i) - \phi$ is valid [47].

If radiation of high enough energy is absorbed by a solid, electrons can be emitted into the vacuum. This is called the photoemission process. The photoelectric equation

describing energy conservation is

$$E_{kin} = h\nu - E_b(i) - \phi \quad (1.1)$$

where E_{kin} is the kinetic energy of the photo-emitted electron, $h\nu$ is the exciting photon energy and $E_b(i)$ is the binding energy of an electron emitted from the i^{th} level as referenced to the vacuum level. In solids the photoelectron have to overcome the surface barrier and the kinetic energy is decreased by the amount of the work function ϕ of the solid.

Figure 1.1 schematically shows the energy levels in the solid and the energy distribution of the photoelectrons according to eq. 1.1. The Fermi edge E_F is at the top of the valence band and is separated from the vacuum level E_{vac} by the work function ϕ . Thus, while the Fermi energy E_F represents the “physical reference” in solids, the kinetic energy E_{kin} is measured with respect to the vacuum level E_{vac} . The energy distribution of the photoelectrons replicates the electron energy distribution in the solid as can be seen from figure 1.1 at the top. The knowledge about the core photoelectrons intensities can be used for quantitative analysis of the surface composition of a specimen.

Photoemission spectroscopy is (PES) performed in the same way as it was almost a hundred years ago. The basic instrumentation for the PES are: a light source (gas discharge lamp, X-ray tube, or synchrotron radiation source) produces photons which impinge the specimen; electrons excited by the photoelectric effect are analysed with respect to their kinetic energy E_{kin} and momentum \mathbf{p} in an electrostatic analyzer [47].

1.1.2. The Auger process

The Auger process was discovered independently in the 1920's by Lise Meitner [71] and Pierre Auger [4]. Although Meitner reported this discovery two years before Auger, the process was named after Auger. In this process a core level electron vacancy recombines with an electron from an outer shell, and the energy difference is transferred to a third electron which might get ejected from the atom subsequently. The Auger process is illustrated in detail in figure 1.2.

The competing process to the Auger electron emission is X-ray fluorescence, where the excited state decays due a radiative process after photoionization. Photoionization leaves an atom in an excited state with a finite lifetime τ which is determined by the sum of all possible decay processes, including radiative processes. For atoms with a low atomic number ($Z \leq 30$) and for low transition energies ($\leq 10\text{keV}$), the probability for a radiative decay is negligible [72]. The relative probabilities of the competing processes are plotted as a function of the atomic number Z in figure 1.3.

When the hole is filled by an electron of a subshell within the same shell, the process is called Coster-Kronig transition [18], since in an Auger process the electron that fills

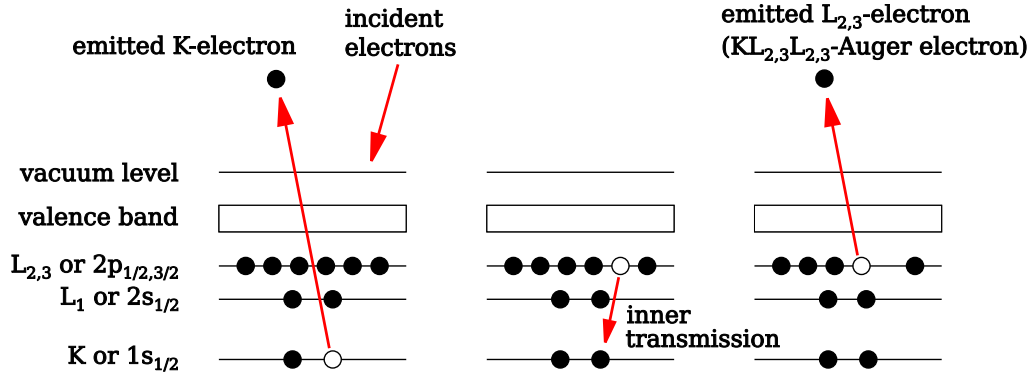


Figure 1.2: Emission of a $KL_{2,3}L_{2,3}$ -Auger electron. The discrete energy levels are represented by the horizontal lines. A core electron is emitted from the atom due the interaction with the energetic incoming electron or X-ray radiation. A possible process for the decay of the excited atom is the Auger transmission: an electron from a higher energy level fills the hole in the core level and the energy difference between the level is transferred to another electron of the same level. This electron is transferred to a higher energy level or, if the energy transfer is sufficient, is emitted from the atom [36].

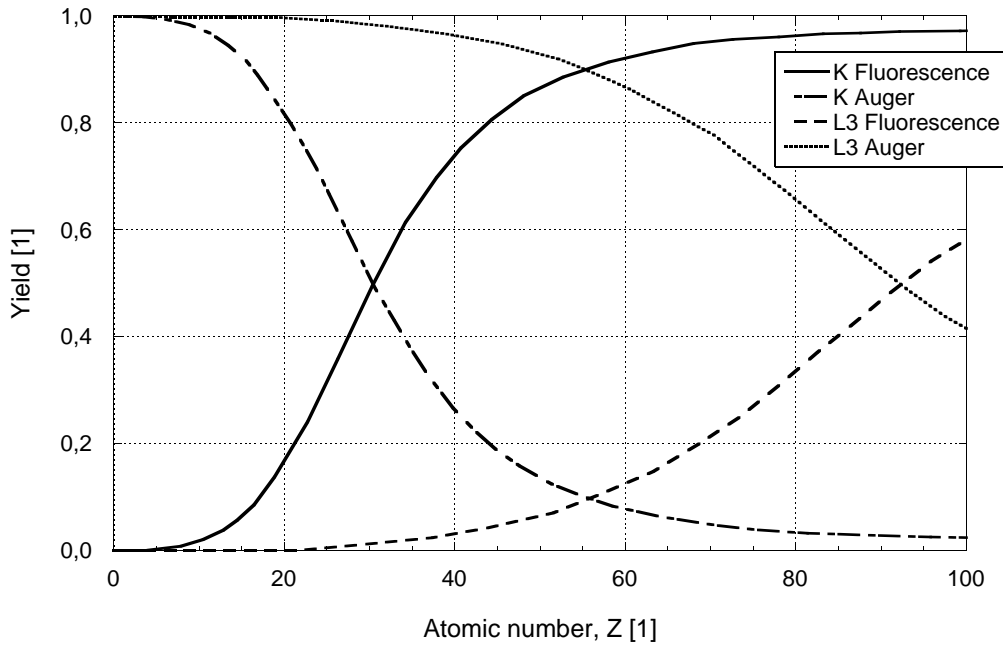


Figure 1.3: Relative probability of K-shell and L_3 -subshell fluorescence compared to the competing Auger process as a function of atomic number Z . For low Z the Auger transition is dominant [72].

the hole does not belong to the same shell. Transitions for which all three participating electrons belong to the same shell, are called super-Coster-Kronig transitions [70]. Due to the large overlap between the levels of the principal shell, both Coster-Kronig transitions are faster than the competing Auger process from the same initial-state. This leads to broader Auger peaks [81].

1.1.3. Principles of APECS

XPS and Auger electron spectroscopy (AES) are complimentary techniques which provide direct information about occupied electrons states in solids. Especially for solids the spectra may become very difficult to interpret, since the line widths are comparable to their separations. Various extensive mathematical data processing methods, including background synthesis and subtraction, deconvolution, and theoretical curve-fitting, were proposed to investigate electron spectra.

Another approach to this problem is to attain additional information from other spectroscopic techniques to improve the understanding of Auger spectra. The application of *post-acquisition* methods is generally complicated and the reliability limited. Alternatively spectral complications can be eliminated (or selected) *during* acquisition. This is essentially the principle for two-parameter experiments such as measurements of electron distributions for various geometric spectrometer configurations, and coincidence experiments.

APECS is a time-coincidence spectroscopy, which is based on the principle that if two electrons are detected within the experimental time resolution it is assumed, that these electrons were emitted during the same excitation-decay event. The time difference between the emission of the photoelectron and the emission of the Auger electron is of the order of 10^{-15} s for simple Auger processes where core-levels are involved [38, 37]. The experimental time resolution achieved is considerably larger (about 10^{-9} s) than the lifetime of the Auger decay. Therefore one needs to be careful to separate the true coincidences from the false ones [81].

1.1.4. Surface sensitivity of APECS

For completeness, the model on the surface sensitivity of APECS [111] is briefly summarized below. A electron which is emitted inside the solid is scattered elastically and inelastically many times until it reaches the surface. Several types of inelastic collisions can be distinguished:

- The excitations of bulk plasmons where the electron is influenced by the polarization field set up by itself in the solid [64, 24, 120]. This excitations are labelled with a 'b' in the following.

- Near the surface, additional modes (surface plasmons) of the inelastic process occur, which decay within a few Å below the surface towards the interior of the solid and above the surface. These surface excitations are labelled with an 's' [82, 95, 119, 17, 102, 23, 3].
- During the excitation process of the core electron due to a photon, the emitted photoelectron may experience a change in the kinetic energy caused by the response of the loosely bound solid state electrons to the sudden appearance of the core hole [47]. This process is referenced to as “intrinsic excitation”.

In the further considerations the intrinsic excitations are not considered since they are believed to be inherent to the emission process.

Every single electron which is emitted from the solid has suffered a number of energy losses due to excitation of bulk and surface plasmons. The number of collisions can be labelled n_b and n_s accordingly and all emitted electrons which suffered the same number of collisions of the same type can be combined to groups described by n_b and n_s . These groups are called partial intensities and are labelled $C_{n_s, n_b}(\Omega)$, where $\Omega = (\theta, \phi)$ defines the emission direction. The spectrum of the emitted electrons, or yield $Y(E, \Omega)$, can be defined as the sum of the partial spectra of all groups:

$$Y(E, \Omega) = \sum_{n_b=0}^{\infty} \sum_{n_s=0}^{\infty} C_{n_s, n_b}(\Omega) F_{n_s, n_b}(E) \quad (1.2)$$

Here, E is the energy of the emitted electrons and $F_{n_s, n_b}(E)$ is the energy distribution after a certain number of collisions for a given normalized source distribution $f_0(E)$. There is only a weak energy dependence of the normalized distributions $w_s(T, E)$ for surface energy losses and $w_b(T, E)$ for bulk energy losses [118]. Therefore, it is valid to assume $w_{s,b}(T, E) \simeq w_{s,b}(T)$. This allows to express the energy distributions $F_{n_s, n_b}(E)$ as multiple convolutions in the form of recurrence relations:

$$\begin{aligned} F_{n_s, n_b}(E) &= \int_0^{\infty} f_0(E+T) L_{n_s, n_b}(T) dT \\ &= \int_0^{\infty} F_{n_s-1, n_b}(E+T) w_s(T) dT \\ &= \int_0^{\infty} F_{n_s, n_b-1}(E+T) w_b(T) dT \end{aligned} \quad (1.3)$$

Here, $L_{n_s, n_b}(T)$ represent the partial loss distribution, i.e. the energy loss distribution after a certain number of surface and bulk losses. Since the partial energy and loss distributions are normalized by integration over the energy, one can see from eq. 1.2 that the partial intensities $C_{n_s, n_b}(\Omega)$ represent the number of electron within each group.

The collision number distribution $W_n(s)$ describes the probability for an electron to belong to the group of n -fold scattered electrons after travelling a path of the length s . According to Ref. [117] near the region of the peak this distribution can be written as

$$W_n(s) = P_n\left(\frac{s}{\lambda}\right) = \left(\frac{s}{\lambda}\right)^n \frac{e^{-s/\lambda}}{n!} \quad (1.4)$$

where λ is the inelastic mean free path (IMFP) [88, 24]. The function on the right hand side is equivalent to the Poisson distribution. The pathlength s which electrons travel before they are emitted is normally longer than the direct path from the point of emission at the depth z to the surface because of elastic collisions in the solid. $Q(s, \Omega; z)$ describes the distribution of the path lengths of electrons emitted at the depth z and leaving the surface along the direction Ω . Multiplying the path length distribution $Q(s, \Omega; z)$ with the collision number distributions $W_{n_s}(s)$ and $W_{n_b}(s)$ for surface and bulk losses respectively and the depth distribution $c_0(z)$ of the signal electrons and integrating over all pathlengths one obtains:

$$\begin{aligned} C_{n_s, n_b}(\Omega) &= \int_0^\infty \int_0^\infty Q(s, \Omega; z) W_{n_s}(s) W_{n_b}(s) c_0(z) ds dz \\ &= \int_0^\infty \phi_{n_s, n_b}(z, \Omega) c_0(z) dz \end{aligned} \quad (1.5)$$

Here we introduced the depth distribution function (DDF) or partial escape distribution $\phi_{n_s, n_b}(z, \Omega)$. The DDF describes the probability for electrons escaping from the solid along the direction Ω after certain number of collisions from emission depth z . In the following considerations it is assumed that the specimen is a homogeneous semi-infinite solid and that the excitation probability also doesn't change with the depth z . Therefore $c_0(z) = \text{const.}$

Equation 1.2 can now be generalized to case of APECS for the double differential yield

$$\begin{aligned} Y(E_A, E_X, \Omega_A, \Omega_X) &= \sum_{n_{sA}=0}^\infty \sum_{n_{bA}=0}^\infty \sum_{n_{sX}=0}^\infty \sum_{n_{bX}=0}^\infty C_{n_{sA}, n_{bA}, n_{sX}, n_{bX}}(\Omega_A, \Omega_X) \\ &\quad \times F_{n_{sA}, n_{bA}}(E_A) F_{n_{sX}, n_{bX}}(E_X) \end{aligned} \quad (1.6)$$

where the index "A" and "X" label Auger electron and the photoelectron quantities respectively. Since now only signal electrons which were emitted from the same location are of interest, the partial intensities should be established via:

$$C_{n_{sA}, n_{bA}, n_{sX}, n_{bX}}(\Omega_A, \Omega_X) = \int_0^\infty \phi_{n_{sA}, n_{bA}}(z, \Omega_A) \phi_{n_{sX}, n_{bX}}(z, \Omega_X) dz \quad (1.7)$$

In APECS the impact of multiple scattering on the line shape of correlated electrons is then described by equations 1.6 and 1.7. It was assumed in eq. 1.6 that the Auger electron distribution is independent of the energy of the photoelectrons with which the Auger electrons are observed in coincidence with. This is known not to be strictly correct [74, 98], but this fact is not essential for further considerations. Furthermore, we introduce the rectilinear model where elastic scattering is neglected. Additionally, surface excitations are not considered in order to investigate the salient features of eqs. 1.6 and 1.7. In this straight line approximation, any two points in space are connected by a unique trajectory and the pathlength distribution becomes:

$$Q(s, \theta; z) = \delta(s - z/\cos\theta) \quad (1.8)$$

We also assumed here that we use a homogeneous specimen with planar symmetry. Hence, all relevant quantities have a dependency on the polar emission angle θ . After inserting eq. 1.8 into eq. 1.5 as DDF and integrating eq. 1.7 (using eq. 1.4) we obtain

$$C_{n_A, n_X} = \frac{(n_A + n_X)!}{n_A! n_X!} \left(\frac{\mu_A}{\mu_A + \mu_X} \right)^{n_X} \left(\frac{\mu_X}{\mu_A + \mu_X} \right)^{n_A} \frac{\mu_A \mu_X}{\mu_A + \mu_X} \quad (1.9)$$

where we introduced $\mu_{A,X} = \lambda_{A,X} \cos\theta_{A,X}$. In order to obtain the Auger electron peak intensity in coincidence with the photoelectron peak we need to evaluate $C_{n_A=0, n_X=0}$ from eq. 1.9. We get the well known result [97]

$$C_{n_A=0, n_X=0} = \left(\frac{1}{\lambda_X \cos\theta_X} + \frac{1}{\lambda_A \cos\theta_A} \right)^{-1} \quad (1.10)$$

which describes the surface sensitivity in APECS. We obtain in addition the singles partial intensities from eq. 1.9 by summing over one of the two collision numbers,

$$C_{n_A}^{singles} = \sum_{n_X=0}^{\infty} C_{n_A, n_X} = \lambda_A \cos\theta_A \quad (1.11)$$

and

$$C_{n_X}^{singles} = \sum_{n_A=0}^{\infty} C_{n_A, n_X} = \lambda_X \cos\theta_X \quad (1.12)$$

consistent with eq. 1.5 in the regarded approximation. The enhanced surface sensitivity of APECS as compared to the singles spectrum is demonstrated by comparing eqs. 1.10 and 1.11.

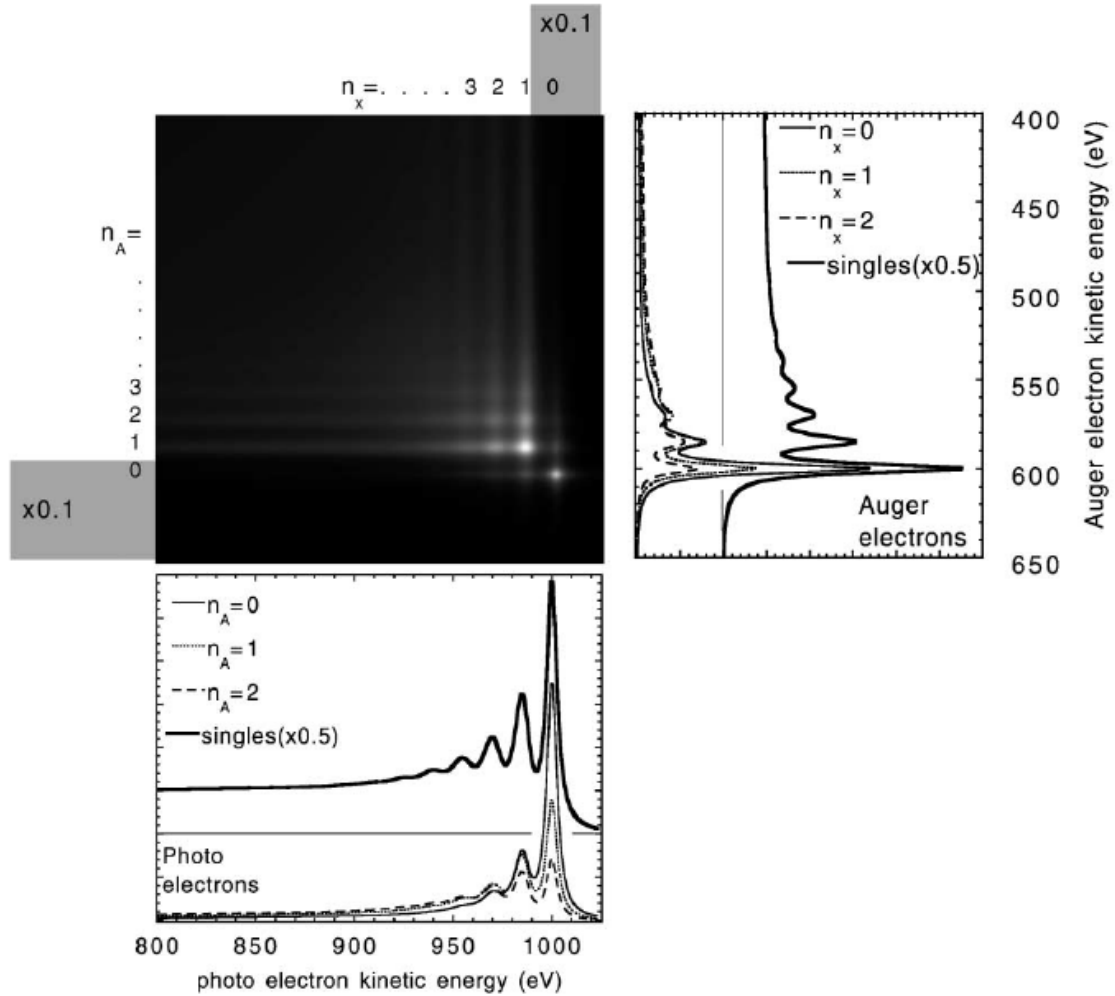


Figure 1.4: Double-differential APECS spectrum for two model peaks, which were simulated with Monte Carlo simulation using the straight line approximation. Surface excitations were neglected in these calculations. Near the region of the peaks marked with a grey band the image was scaled by a factor of 0.1. On the right side a singles Auger spectrum and the coincidence spectra of the Auger peak with the photopeak (full line), with the first plasmon loss (dotted line) and with the second plasmon loss (dashed line) can be seen. At the bottom a singles photoelectron spectrum is depicted, as well as the coincidence spectra of the photopeak with the Auger peak (full line), with the first plasmon loss (dotted line) and with the second plasmon loss (dashed line) [111].

Figure 1.4 shows an illustrative example of eq. 1.6. Here, APECS model calculations in the straight line approximation for an Al sample were conducted for a hypothetical Auger peak at 600 eV and a photoelectron peak at 1000 eV. Both peaks were described as a Lorentzian with a FWHM of 1.0 eV. Both detectors had an observation angle of 60° off normal. The bulk energy loss distribution $w_b(T)$ was determined on the basis of optical data for Al [26].

Due to the enhanced surface sensitivity of APECS it can be seen that for the Auger spectra in coincidence with the photoelectron peaks, the inelastic loss features are strongly suppressed compared to the singles spectrum. Note, that the loss features of the Auger spectrum in coincidence with the first plasmon loss ($n_X = 1$) are similar to the case where $n_X = 0$, but the elastic peak is decreased. This decreased surface sensitivity is due to the, on the average, larger depths of emission of the Auger electrons, since the photoelectrons which scattered once inelastically stem from deeper inside the solid.

This allows one to select Auger electrons from various depths by measuring the Auger electrons in coincidence with the loss features in the photoelectron spectrum. The depth resolution may be rather disappointing though for higher order losses, since the fractional depth resolution is given by $\Delta z/z \approx (\lambda \cos \theta/z)^{1/2}$ [116]. Still, the possibility to select the emission depth of Auger electrons with coincidence measurements enables one to conduct new kind of experiments as described in section 1.2.3.

1.1.5. Considerations about the coincidence rate

For APEC spectrometer the efforts to achieve high energy resolution on one hand and obtain data with good statistics in a short time on the other hand counteract each other. In non-coincidence experiments an increase in the energy resolution by the factor two decreases normally the intensity by approximately the same factor. For non-coincidence experiments it is possible to increase the incident flux to compensate the drop in the countrate, although this may also have limits (e.g. if the sample gets damaged). In coincidence experiments the increase of the incident flux often leads only to a insignificant decrease or even an increase of the time needed to achieve acceptable statistics. Therefore one has to put much effort into the apparatus design to compensate for the impossibility to increase the incident flux. In this section general considerations about the coincidence rate and the influence of the incident flux are investigated. This is also important for a comparison to the novel spectrometer called MoVES explained later 3.3 in detail. The considerations presented in this section closely follow the work in ref. [50].

A typical APECS experiment consists of two electron single-channel detectors, where one counts electrons in the energy range of the photoelectron peak, while the other covers the energy range of the Auger peak. We define the core hole creation per unit time and unit volume with R . This parameter is proportional to the incident flux. For every event two electrons are emitted if we assume that the Auger transition dominates compared to the creation of a photon. In addition, γ_i defines the signal to signal-plus-background ratio

for each channel, which characterizes the background of single electrons events which are proportional to the incident flux. For each detector $i = 1, 2$ we can then define a singles countrate

$$\nu_{Si} = \frac{\alpha_i R V_i}{\gamma_i}$$

where α_i are the efficiencies of the detectors and V_i is the detection volume. The efficiencies α_i include the detector efficiency as well as the probability that a core-hole is created in the detection volume V_i and the created electrons are emitted and detected.

We assume now that the coincidences are detected by a simple coincidence circuit (e.g. an AND gate), which has a time resolution of τ . Since the lifetime of an Auger decay is in the order of 10^{-15} s and the timing resolution of TDCs (time-to-digital converter) are usually in the order of 10^{-9} s, the latter together with other parameters of the signal channels defines the time separation of two events which are to be considered in coincidence. This circuit is called the coincidence channel and its countrate is given by ν_C . The true coincidence countrate is given by

$$\nu_T = \alpha_1 \alpha_2 R V_c \quad (1.13)$$

where V_c is the volume shared by both detectors. But there is also a finite possibility that two not related events are detected in each single channel within the time τ . Hence, there is also a contribution to the coincidence countrate ν_C from the accidental countrate

$$\nu_A = \nu_{S1} \nu_{S2} \tau = \frac{\alpha_1 \alpha_2 V_1 V_2 R^2 \tau}{\gamma_1 \gamma_2} \quad (1.14)$$

The coincidence rate ν_C is the sum of ν_T and ν_A . One can notice from equation 1.13 and 1.14 that ν_T is proportional to R while ν_A is proportional to R^2 .

In the following we'll have a closer look at the detector volumes V_i . The surface areas A_i which the detectors cover have sharp boundaries, but the possibility that electrons from the depth z are emitted is $\exp(-z/\lambda_i)$. Here, λ_i is the inelastic mean free path (IMFP) which is dependent on the energy of the electrons. The electron yield emitted from the volume V_i is then

$$R A_i \int_0^\infty \exp(-z/\lambda_i) dz = R A_i \lambda_i$$

Since this is the same yield which would be emitted from a volume $A_i \lambda_i$ we define

$$V_i \equiv A_i \lambda_i$$

To determine the coincidence rate ν_C the Volume V_c needs to be defined. If both detectors cover the surface area A_c the true countrate is

$$\nu_T = \alpha_1 \alpha_2 R A_c \int_0^\infty e^{-z/\lambda_1} e^{-z/\lambda_2} dz = \alpha_1 \alpha_2 R A_c \frac{\lambda_1 \lambda_2}{\lambda_1 + \lambda_2}$$

If we compare this result with equation 1.13 we can define

$$V_c \equiv A_c \frac{\lambda_1 \lambda_2}{\lambda_1 + \lambda_2}$$

For some cases $\lambda_1 \approx \lambda_2$ and the last equations simplify to $V_c = A_c \lambda / 2$. So even if the detectors are perfectly aligned the coincidence volume is only half of the singles detector volume, since the surface sensitivity of APECS is higher than for the singles spectrum.

In order to derive the true coincidence rate ν_T , the accidental countrate ν_A needs to be experimentally determined. This can be achieved by establishing a second coincidence circuit called the accidental channel, where the second channel is recorded after a time delay much larger than the time resolution τ . Hence, the true countrate for this circuit is zero.

For non-coincidence experiments the signal is $S = t\nu$, while the noise is defined as $N = \sqrt{t\nu}$. We can solve these equations for t as a function of S/N and ν

$$t = (S/N)^2 / \nu \quad (1.15)$$

This well known result expresses that the time for an experiment is inversely proportional to the countrate ν and proportional to the signal-noise ratio S/N . It is useful to define ν_{eff} as the time needed to conduct an experiment to achieve a signal-noise ratio of unity. We replace now the bare countrate ν with the effective countrate ν_{eff} to generalize equation 1.15. For coincidence experiments $S = t\nu_T$ and $N = \sqrt{t(\nu_T + \nu_A)}$ and we obtain for the effective countrate

$$\nu_{eff} = \frac{\nu_T^2}{\nu_T + \nu_A} \quad (1.16)$$

This function is plotted in Figure 1.5. Equation 1.16 can be written in terms of experimental parameters

$$\nu_{eff} = \frac{\gamma_1 \gamma_2 \alpha_1 \alpha_2 R'}{\gamma_1 \gamma_2 + GR'\tau}$$

where we defined $G \equiv V_1 V_2 / V_c^2$ and $R' \equiv RV_c$ for simplification. For a low incident flux the accidental countrate is negligible due to its R^2 dependency and $\nu_{eff} = \nu_T$. For a high incidence the effective countrate saturates at

$$\nu_{eff}^0 = \frac{\gamma_1 \gamma_2 \alpha_1 \alpha_2}{G\tau}$$

which is the highest rate that can be achieved. Hence, because of the saturation of ν_{eff} it is of no useable effect if the intensity is raised above a certain limit. If $\nu_A = \nu_T$ which corresponds to intermediate incident flux the singles rate is given by

$$\nu_{Si} = \frac{\alpha_i V_c \gamma_i}{V_i \tau}$$

For this conditions ν_{eff} becomes half of ν_{eff}^0 and the true and accidental countrate is of the same order. Hence, the numerical error made by subtracting the accidental countrate from the coincidence count rate is minimal.

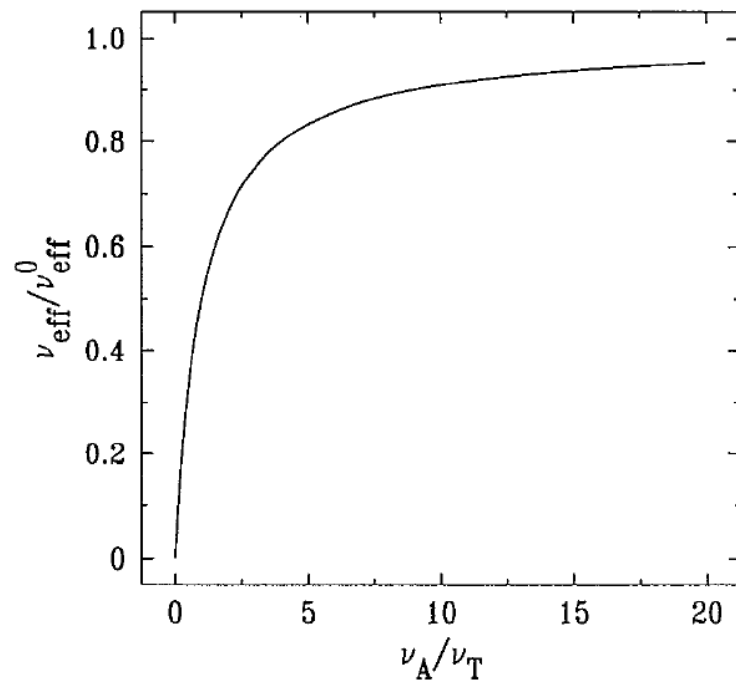


Figure 1.5: The effective count rate ν_{eff} is plotted against the ratio ν_A/ν_T , which is proportional to the incident flux. For a high incident flux ν_{eff} converges against a certain limit ν_{eff}^0 . Hence, there is no improvement in the count rate if the incident flux is increased above a certain limit (figure taken from [50]).

1.2. Emission-Depth-Selective APECS

Coincidence measurements at the synchrotron in Trieste (ELETTRA) [35] were conducted in order to investigate and verify the enhanced surface sensitivity of APECS, which theory was introduced in section 1.1.4. Here, the Si-2*p* photopeak was measured in coincidence with the Si-LVV Augerpeak as well as its inelastic features to show that it is possible to select the emission depth of photoelectrons [109].

1.2.1. Experimental aspects

In this section the instrumentation required for APECS is briefly presented. We outline the concepts how pairs of electrons can be detected in time coincidence rather than to give a detailed description of the characteristics of the instrumentation.

The APECS technique was developed by Haak, Sawatzky and Thomas [38, 37, 39] and is still in use. Similar to AES or XPS the sample is illuminated in vacuo with usually soft X-rays. Two electron spectrometers observe the same location at the sample. One of them is usually fixed to the kinetic energy of photoelectrons while the other scans the energy range of the Auger electrons. Another possible operational mode of the spectrometers is to fix one spectrometer to the energy of the Auger electrons and scan the photoelectron spectrum with the other. The non-coincidence or singles spectrum is collected at the same time with the coincidence spectrum for both modes, which allows to eliminate differences between the two spectra due to analyser calibration.

A sample application of APECS is presented in figure 1.6 illustrates the use of the modes. Here, APECS is applied to probe the local electronic properties of an inhomogeneous solid. A solid is composed of two types of atoms, “A” and “B”, as shown in figure 1.6(a). These atoms may be either from a different species or from the same atomic species that are nonequivalent due to local chemical or physical properties. Such inhomogeneities may lead to a shift in the core energy levels or to changes in the shape of the valence band.

If the sample is illuminated with X-rays photoelectrons are emitted from the the valence band and the core levels and the excited atom may then decay via an Auger transmission. All electrons are measured in the singles electron spectrum shown in figure 1.6(b). It is difficult to determine a specific emission feature with a particular site in the valence band energy range, since here the photoemission spectrum is integrated over the nonequivalent sites in the solid. The same problems arise for the Auger electron energy range due to the overlap in energy because of the small core level shift.

The coincidence Auger technique can be used to separate the local electronic structures of atoms A and B as illustrated in figure 1.6(c). In the case that one electron spectrometer is fixed at the kinetic energy corresponding to the emission of the core level electrons of atom A, the coincidence Auger electrons participated in the decay of the core hole

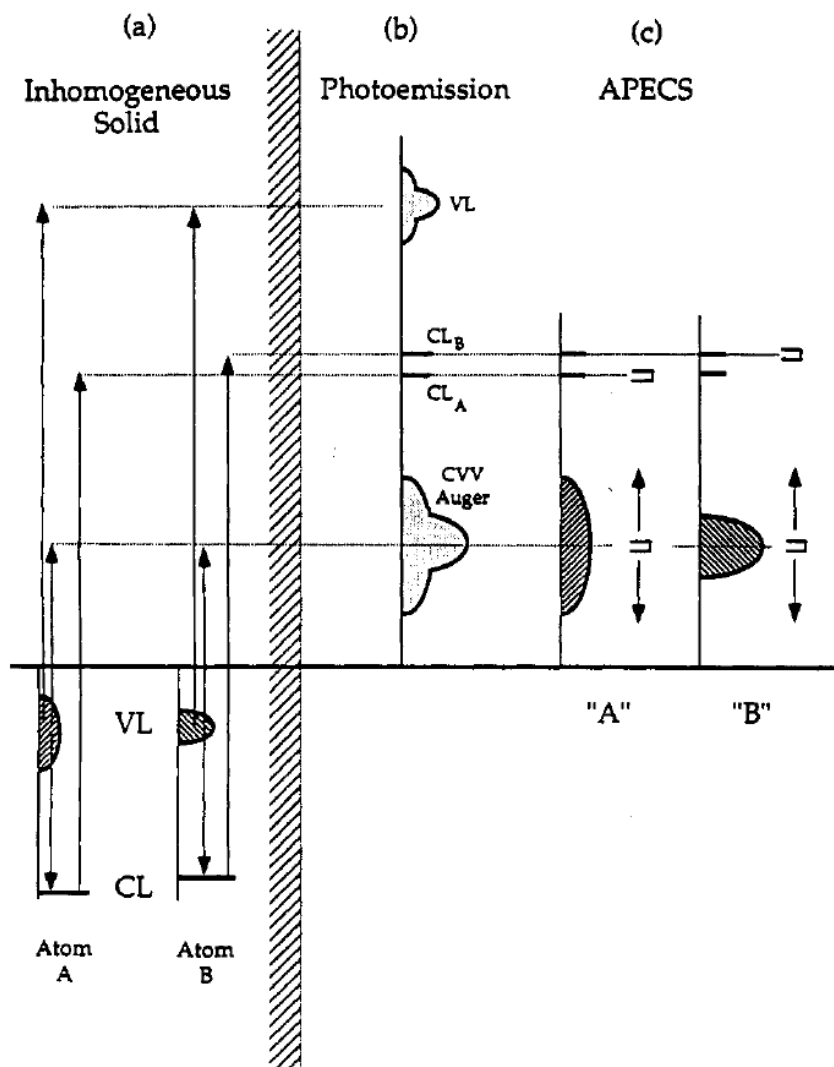


Figure 1.6: In panel (a) the photoexcitation process and the following Auger process of an inhomogeneous solid comprised of two types of atoms, A and B, are considered. Panel (b) shows the conventional photoemission spectrum consisting of valence level (VL), core level (CL), and Auger (CVV) electrons. Panel (c): If the CVV Auger region is measured in coincidence with particular core level photoelectrons ("A" and "B") we only obtain the Auger spectrum from the decay of that core hole [9].

at site A. Respectively, if the electron spectrometer is fixed at the kinetic energy of photoelectrons emitted from the atom B, local electronic structures near the site B are probed. Therefore, APECS can be applied for investigation of the electronic structure at a particular site in the solid [9].

In an APECS experiment two electrons are considered originating from the same ionization event on the basis of their arrival in time at each spectrometer, depending on their energy. It is as a matter of principle not possible to distinguish between uncorrelated electron events and true coincidence electron events. The former are termed accidental coincidences, or short accidentals. The time resolution of the experiment has a major impact on the ability to discriminate between true and accidental coincidences.

Since the number of coincidence events are proportional to the incident X-ray flux, while the accidentals are proportional to the square of the flux, there is actually a hard limit to which the flux can be increased. This causes low count-rates for APECS which is also a major drawback of this technique. In section 1.1.5 all the details about the achievable countrate is considered in more detail.

APECS has been adapted already for solid-state targets to synchrotron radiation by Jensen et al. [50], Gotter [35] and recently by Mase et al. [68]. The different experimental aspects for continuous synchrotron radiation and pulsed sources have been reviewed by Jensen et al. [50].

1.2.2. ALOISA Beamline at ELETTRA

ALOISA is an acronym for “Advanced Line for Overlayer, Interface and Surface Analysis” and is a multipurpose beamline at the synchrotron ELETTRA in Trieste [35]. A wide energy range of the light beam from 120eV to 8000eV can be provided at this beamline due to a peculiar mono-chromator. The spot size in the experimental chamber is about $30 \times 200 \mu\text{m}$ and the flux at the sample is 10^{11} photons/s for the low energy range and 5×10^{10} photons/s in the high energy range.

Seven hemispherical electron energy analyzer are mounted in an UHV chamber, the bimodal analyzers have an opening angle of 1° and two angular degrees of freedom. The axial analyzers have only one degree of freedom and an acceptance angle of 2° . Furthermore, a RHEED (Reflection high energy electron diffraction) device and a sputter gun are available in the preparation chamber. The sample is mounted on a high resolution manipulator which allows to manipulate the sample with six degrees of freedom. A fast entry system enables the rapid change of samples.

The seven hemispherical mirror analyzers (HMA) allow to do APECS, since it is possible to scan different electron energies at different angles. For an APECS measurement the bimodal analyzers are user to measure the photo peak, while the axial analyzers measure the Auger peak [94].

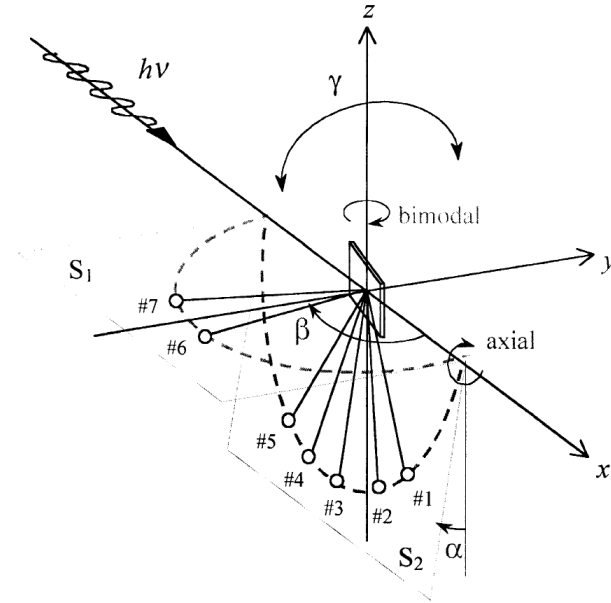


Figure 1.7: Seven electron energy analyzer are installed in the experimental chamber. The rotation axis of the bimodal analyzers (6, 7) can be rotated in the z, y -plane, while the rotation axis of the axial analyzers (1–5) is identical to the chamber axis [94].

1.2.3. Experiments and results

Investigations of the collision statistics for $n_A = 0, 1$ and $n_X = 0, 1$, where the Auger electron and the photoelectron suffered no or one plasmon loss respectively, were conducted. Related peak-peak, peak-plasmon, and plasmon-plasmon coincidences were measured.

A Si(100) sample was cut from a wafer of lightly doped Si ($10^{15} P$ atoms cm^3) and mounted in the ALOISA beam line chamber at ELETTRA (base pressure $\sim 3 \times 10^{10}$ mbar) [35]. The sample was prepared by repeated cycles of annealing at 1100°C and 3 keV Ar^+ sputtering. X-ray photoemission spectroscopy (XPS) angle scans showed that after this treatment the Carbon and Oxygen contamination levels were below 10% of a monolayer. Since the XPS-scans also showed no diffraction effects, it could be assumed that the resulting surface was completely amorphized to sufficiently large depths. This cleaning procedure was repeated at every injection of electrons in the synchrotron ring (approximately every ~ 24 h) during the coincidence measurements. Several singles spectra were measured as a reference at $h\nu = 300$ eV. This spectra were subjected to a partial intensity analysis [106, 118, 108], in order to eliminate multiple scattered electrons and to determine the peak parameters and gain information on the intrinsic and surface excitation probabilities needed in the simulation of the APECS spectra.

As an example, in figure 1.8 the dash-dotted line shows the measured Si-LVV peak while the data points show the result of the line shape analysis of this peak. Three Gaussians were needed to fit the background subtracted spectrum. These three com-

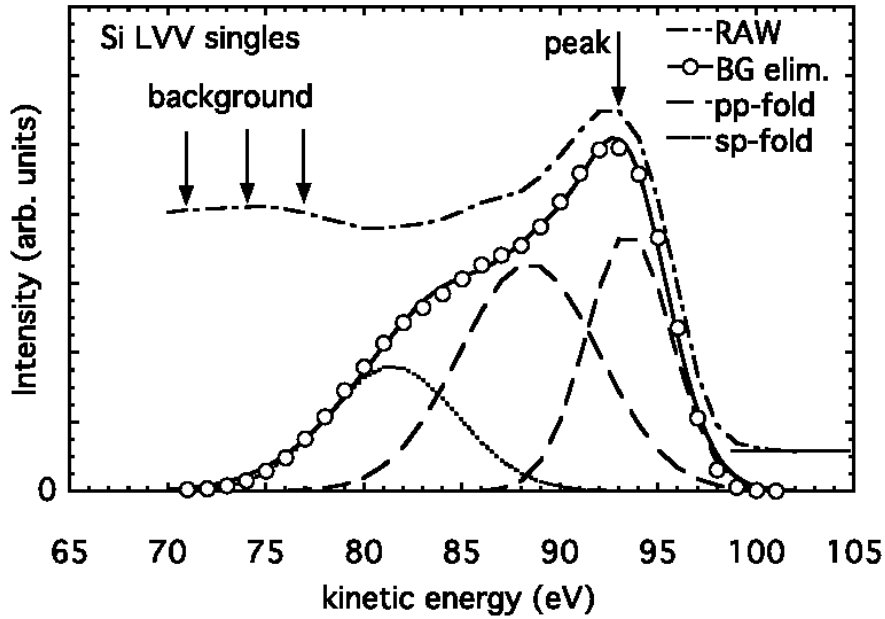


Figure 1.8: The dash-dotted line shows the experimental Si-LVV singles spectrum. The spectrum where the background is removed via the the Partial Intensity Analysis [92] is shown by the open circles [109].

ponents compare well with the assignment of Parnaselci and Cini [76] who applied the extended Cini-Sawatzky theory to calculate the Si-LVV and Si-KVV line shapes. Thus the dashed curves are identified as the self-convolution of the p-state electronic density of states (p-DOS), while the dotted curve corresponds to the convolution of the s- and p-DOS. The intensity ratio of the sp- and pp-contributions of our results is 0.30 ± 0.05 , close to the value of 0.38 ± 0.02 , as quoted in ref. [78]. The Si $2p$ spectrum, where the background was already subtracted, was fitted by a linear combination of two Doniach-Sunjic line shapes with a fixed doublet ratio of $I_{2p_{3/2}}/I_{2p_{1/2}} = 2$. The difference between the $2p_{1/2}$ and $2p_{3/2}$ amounted to 0.6 eV, in good agreement with earlier assessments [100].

After the measurements of the singles spectra, Si $2p$ photoelectrons recorded in the two bimodal analyzers (energy resolution $\Delta E = 2.2$ eV) of the ALOISA apparatus were measured in coincidence with Auger electrons measured by one of the five axial analyzers ($\Delta E = 3$ eV) [35]. In order to reach a true to false coincidence ratio of approximately one in the peak-peak coincidences, as explained in section 1.1.5, the mono-chromator slit width was reduced to decrease the photon beam intensity. For the coincidence measurements the surface normal of the sample was in the plane of incidence of the incoming (linearly polarized) radiation and the polarization vector. The angle between the sample surface normal and the incidence direction of the synchrotron radiation was set to be 72° , well below the critical angle ($\sim 84^\circ$ at $h\nu = 300$ eV) for total reflection. The bimodal analyzers were oriented at emission angles of 2° and 20° relative to the surface normal. The plane of the axial analyzers was tilted 35° with respect to the plane

of incidence, while the bimodal analyzers were in this plane.

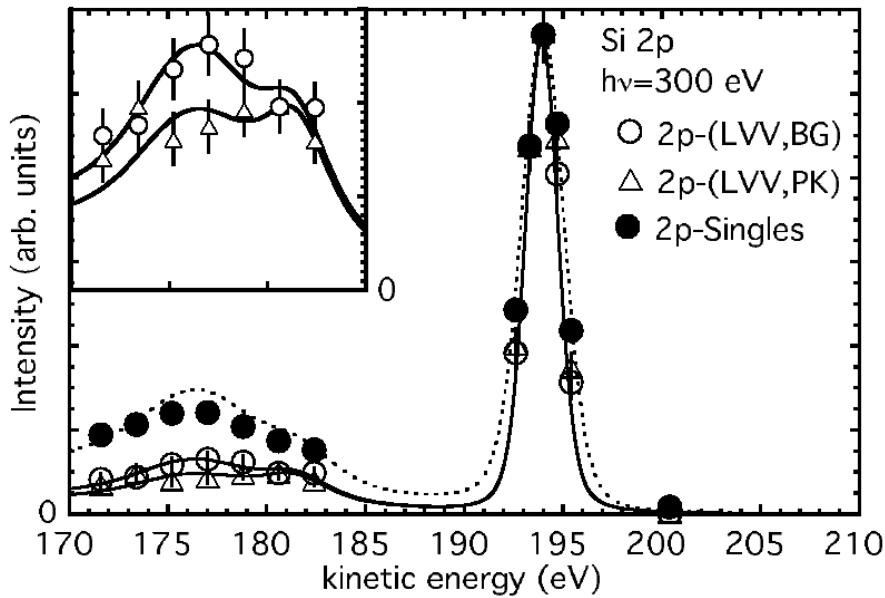


Figure 1.9: Singles and coincidence spectra of the Si-2p peak are shown in this plot. The singles spectrum is represented by closed circles. Open triangles show the coincidence spectrum of the Si-2p photopeak with the Si-LVV Auger peak (marked with “peak” in fig. 1.8), while the open circles show the coincidence spectrum of the photopeak with the background of the Auger line (marked with “background” in fig. 1.8). The SESSA software [92] was used to conduct model calculations represented by solid and dotted lines. The data were normalized at the peak maximum. An expanded view of the BG and PK spectra is shown in the inset [109].

For optimization reasons two of the axial analyzers were tuned to the no-loss Auger peak, while the other three measured the intensity at the first plasmon loss, as is shown by the arrows in fig. 1.8. After data acquisition, the spectra recorded in coincidence with the LVV peak and plasmon loss were combined to yield the 2p spectra shown in fig. 1.9. with the required statistics in the plasmon region. The energy range chosen for the 2p spectrum is shown in fig. 1.9 and covers the no-loss peak and the first volume plasmon as well as a single point well above the peak, recorded as a reference. Data accumulation took place over a period of 6 d with an effective counting time of approximately 90 h.

The singles spectra of the Si 2p region are represented by the filled circles in fig. 1.9 and are compared with the intensities measured in coincidence with the no-loss peak (open triangles, referred to as “PK” hereafter) and the inelastic background (open circles, “BG”) in the Si-LVV Auger electron line. All data shown in this figure are normalized to the same value in the peak maximum. It can be clearly seen that compared to the singles spectrum the intensity of the plasmon in the PK spectrum is significantly reduced by about a factor of 2.5. This can be explained by the well-known enhancement of the surface sensitivity of APECS (see eqs. 1.10 and 1.11) as compared to ordinary

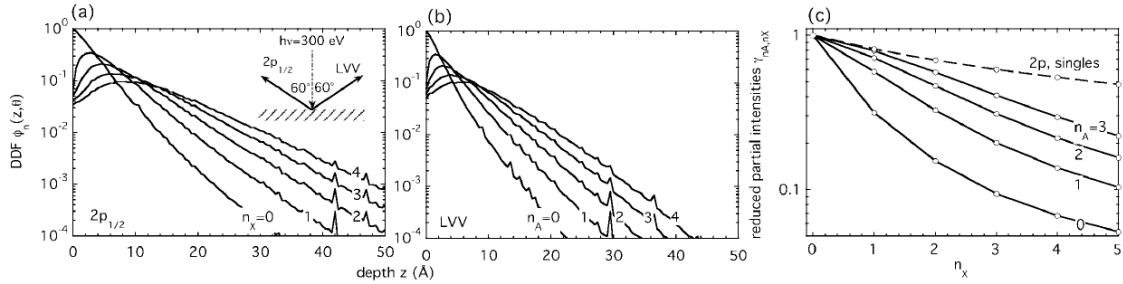


Figure 1.10: (a) Partial escape distribution, or depth distribution function (DDF), $\phi_{n_X}(z, \theta_0)$ for the Si $2p_{1/2}$ transition. These data were simulated by means of a Monte Carlo model [92] for normal x-ray incidence, and with the Auger and photoelectron detected at an off-normal emission angle of 60° , as indicated in the inset. (b) Same as (a), for Si-LVV Auger electrons. (c) Reduced double differential partial intensities for bulk inelastic scattering $\gamma_{n_X, n_A} = C_{n_X, n_A} / C_{n_X=0, n_A=0}$ calculated from the curves in (a) and (b) using Eq. 1.7. The dashed curve represents the Si $2p$ singles partial intensities for bulk scattering [109].

XPS [38]. In the BG spectrum, the first plasmon intensity is higher, indicating that the path length the electrons travel inside the solid is longer, or in other words, that they originate from greater depths. These observations are qualitatively consistent with the theoretical considerations for the surface sensitivity discussed in section 1.1.4. This can be seen in fig. 1.10(c) where the corresponding partial intensities for the first volume plasmon in the singles spectrum (the point $n_X = 1$ in the curve labeled “2p, singles”) is larger than for the BG spectrum ($n_X = 1, n_A = 1$) while the latter is in turn larger than for the PK spectrum ($n_X = 1, n_A = 0$). The experimental results therefore also provide direct proof for the existence of extrinsic plasmons that are independent from the atomic decay and (many-electron) relaxation processes involved in the photoelectron emission at the source.

Elastic as well as intrinsic and surface inelastic collisions need to be taken into consideration for a quantitative comparison. Simulations of the singles spectrum and the coincidence measurements were conducted [92] and are shown by the solid and dotted lines in fig. 1.9. The simulations agree quantitatively with the experimental data. The main uncertainty in the theoretical calculation is the intensity of the surface plasmon peak and the contribution of intrinsic excitations. However, even when surface and intrinsic excitations are completely disregarded in the simulation, the ratio of intensities of the first plasmon peak of the simulated BG and PK spectrum changes only by up to 15% and still agrees with the measurements within the experimental uncertainty. Therefore we conclude that the change of the plasmon intensity is a signature of the different depths sampled in the PK and BG spectrum and, most importantly, that the intensity of the elastic peak of these spectra is due to electrons with a different average emission depth: while the electrons in the PK spectrum originate from an average depth of about $2.0 \pm 2.1 \text{ \AA}$, the average emission depth of the BG spectrum amounts to about

$4.7 \pm 4.9 \text{ \AA}$. The singles spectrum, on the other hand, consists of electrons emitted from an average depth of $6.1 \pm 6.5 \text{ \AA}$.

The uncertainties quoted above for the emission depths represent the root-mean-square widths $\sigma_{\langle z \rangle}$ of the fluctuations in the emission depth. In the rectilinear motion model, $\sigma_{\langle z \rangle}$ is equal to the average emission depth $\langle z \rangle_0$. For APECS in the rectilinear model the average emission depth can be estimated to

$$\langle z \rangle_{n_X, n_A} = (n_A + n_X + 1) \frac{\mu_A \mu_X}{\mu_A + \mu_X}$$

ignoring surface and intrinsic excitations, while for ordinary XPS $\langle z \rangle = \mu_X$. A realistic estimate of the emission depth cannot be derived from a simple analytic formula, since it should account for all different scattering processes and also depends on the shape of the Auger and photoelectron peak, the shape of the inelastic cross section, and the energy interval in which the Auger and photoelectrons are accepted [111]. Furthermore, this formula neglects that a part of the electrons in the BG spectrum are measured in coincidence with the intrinsic plasmon of the LVV Auger line, which leads to an additional broadening of the emission-depth fluctuations since intrinsic excitations can take place at any depth. These phenomena have been accounted for in the values for $\sigma_{\langle z \rangle}$ presented above. It can therefore be stated that the present results prove the ability of APECS to discriminate the average emission depth of individual electrons within the limits of the statistical fluctuations of the emission depth that are inherent to the stochastic process for multiple scattering.

Another interesting feature seen in fig. 1.9 is the change in the linewidth of the coincidence spectra as compared to the singles spectrum. The simulated spectra match the experimental linewidth by allowing for a narrowing of the linewidth of the coincidence spectra by 0.8 eV, taking into account the experimental broadening of 1.1 eV. The fact that our measurement comprises the unresolved $2p_{1/2}$ and $2p_{3/2}$ components makes the interpretation of this observation difficult. However, it is noted that the line narrowing seems to be symmetric, indicating that both core-hole components are indeed present also in the coincidence spectra.

It was already anticipated [38] that APECS can be used to remove the core-hole lifetime broadening and modify other contributions to line broadening. Indeed, line narrowing in photoemission spectra by APECS has been observed by several groups [98, 51] and is a clear indication for the onestep character of the Auger emission process [74]. The present observation adds to the body of evidence for this statement but on the basis of the experimental energy resolution and statistics it is difficult to decisively pinpoint the reason for this observation.

2. Electron induced Electron Emission from Surfaces

Electrons emitted from a solid due to irradiation of electrons or ions are referred to as “Secondary electrons”. Secondary electrons (SE) can either be excited directly by the incident radiation or due to the following collision cascade.

Furthermore, many other fields in physics like secondary electron microscopy, nuclear fusion, or space technology depend on the knowledge of SE emission and their properties. Hence, it is of vital interest to gain more insight in the field of SE. Due to the involving theory of the excitation and transport of SE and difficult experimental aspects for the energy range of SE, the physics of SE is still a challenging field.

$(e, 2e)$ spectroscopy experiments are a suitable technique to improve the understanding of the SE emission process. $(e, 2e)$ spectroscopy enables one to measure electron energy-momentum densities in solid targets by measuring the reflected electrons and the excited electrons in coincidence.

To investigate the decay of electron excited plasmons in an Al (100) single crystal SE were measured in coincidence with the inelastic features of the elastic peak. The Al (100) single crystal was chosen due its pronounced features in the inelastic tail of the elastic peak. An apparatus developed at the Department of Physics of the Università di Roma Tré was used to conduct these $(e, 2e)$ -experiments.

From the shape and position of the peaks in the resulting coincidence spectra of the SE and from comparison of Monte Carlo simulations to experimental results it is concluded, that the SE emitted from the solid stem from plasmons which decay into single electron-hole pairs. Only a small part of the spectra can be attributed to electrons excited by the collision cascade of secondary electrons.

2.1. Emission of secondary electrons

A detailed review on secondary electrons is given in reference [107], which is summarized in this section. The common definition of the term “Secondary electron” in solid-state physics is that electrons which are emitted from a solid due to irradiation with an energetic beam of electrons or ions are considered as “Secondary electrons” if their kinetic energy is below 50 eV. This definition is problematic since model calculations show that in case of primary electrons the secondary electron (SE) energy distribution has a broad tail up to energies just below the primary energy. In an experiment it is also not possible to distinguish inelastically scattered primary electrons from SE.

In addition, the quantitative interpretation of the SE spectra is very complicated compared to emission phenomena in the medium energy range. Many parameters which describe the electron transport in solids in the energy range below 50 eV are only known with a large uncertainty, since the experiments in this energy range and the theory describing the transport and emission of SE are much more involved than in the medium energy range. For example, the comparison in references [53, 54, 65] demonstrates that experimentally determined SE yields, which are the number of SE emitted per incident primary, exhibit significant scatter of up to 100% [107].

The emission of SE is usually described theoretically on the basis of the three step model [86, 25, 89, 60, 33, 34]. In this model SE are generated due to various processes during which energy from the primary electron is transferred to loosely-bound solid state electrons so that they can overcome the surface barrier (e.g. core level ionizations, electron–electron scattering, or surface and plasmon decay). The band structure of the solid is obviously of major importance for these processes. Furthermore primary electrons can excite more than one SE, and SE can on their own excite other electrons by transferring energy to them.

The transport of slow electrons with an energy below 50 eV in solids is more complicated than for electrons of higher energy. The interaction characteristics of the electrons with the solid have a strong dependence on the electron energy. This is the case for the elastic and inelastic mean free paths as well as for the energy loss distribution for inelastic collisions. In addition exchange and correlation effects can’t be neglected at such low energies as it is usually done for electrons of energies above 200 eV.

For elastic electron–solid interaction in the energy range below 50 eV the choice of the potential to be used in the partial–wave algorithm is of importance. Primary electrons are mainly scattered elastically at weakly bound electrons of the atom, which corresponds classically to a large impact parameter or quantum mechanically to a large angular momentum. Hence, it is not possible to use free-atom potentials, since here solid–state effects are disregarded by definition. In consequence the elastic mean free path (EMFP, i.e. the path electrons travel until they suffer an elastic collision) in solids for low energies differs significantly from the gas phase. The transport mean free path (TMFP, i.e. the path electrons travel until they experience a significant change of the direction) however

depends mainly on the core electrons and is therefore not much influenced by the choice of the potential.

The inelastic mean free path (IMFP, i.e. the average path length electrons travel between successive inelastic collisions) is in general quite large compared to TMFP in this energy region. Therefore the electron transport is determined by the momentum relaxation or, in other words, electrons suffer many large angle deflections until they are scattered inelastically. Hence, the exact shape of the elastic cross section (ECS) is not vital and the ECS can be expressed by an isotropic transport cross section in the transport approximation [118, 16, 93].

Additionally, in this energy region it can't be assumed that electrons don't suffer a deflection during an inelastic collision as this is assumed for the medium energy range. Due to the strong momentum relaxation, this effect can be compensated by replacing the usual (elastic) TMFP λ_{tr} by the total transport mean free path $\lambda_{tr,t}$

$$\frac{1}{\lambda_{tr,t}} = \frac{1}{\lambda_{tr}} + \frac{1}{\lambda_{tr,i}} \quad (2.1)$$

where $\lambda_{tr,i}$ is the TMFP for inelastic scattering.

In summary, due to strong momentum relaxation the SE spectrum is a superposition of many different scattering orders for a complicated excitation function. The emitted energy distribution of the SE is smeared out, making it very difficult to study details of excitation and inelastic scattering characteristics experimentally. Comparison between theory and experiment is therefore a very complicated task.

Another essential aspect of the SE emission process within the three step model is the surface barrier. At the surface the periodicity of the crystal potential is abruptly terminated leading to a surface barrier of the height of typically 10–20 eV, which is in the order of the SE energy. The height of the surface barrier is commonly taken to be the energetic distance between the vacuum level and the bottom of the conduction band. The energy component parallel to the surface is conserved during the emission process, while the perpendicular component is reduced by the value of the surface barrier. Hence, electrons are refracted during the passing of the surface or are even reflected. Only electrons with an exit angle below a certain value, with respect to the surface normal, can leave the solid (depending on the electron energy) .

Data from different experiments on SE emission have a significant scatter as already mentioned above [65, 54, 53]. This can be attributed to various reasons. The contamination of the surface has a major impact on the height of the surface barrier [101] and therefore on the SE emission. In addition, the crystalline state of the surface has an effect on the emitted spectrum due to the change of the surface barrier with the crystal orientation and due to the availability of states for electron transfer from the primary electrons to the electronic subsystem of the solid depending on the orientation.

A SE energy spectrum (curve labelled 4) for 2 keV incident electron on an Al surface is

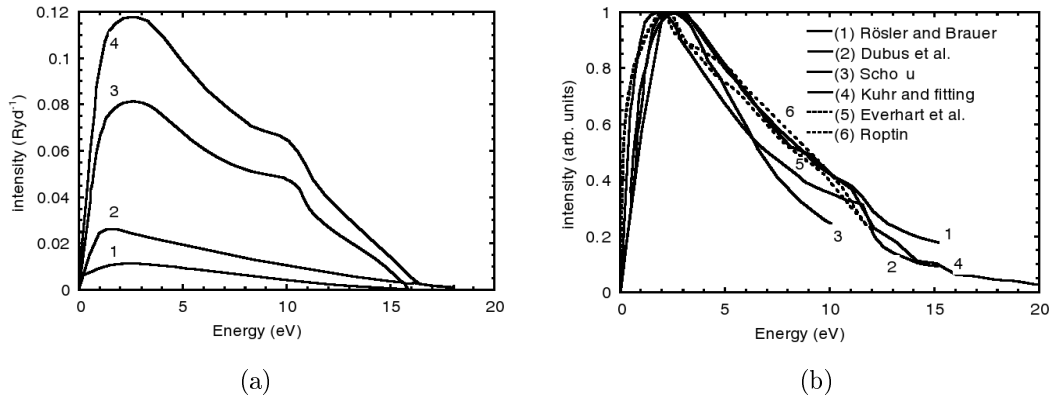


Figure 2.1: (a) Contribution of different excitations mechanisms in Al are revealed for the secondary electron spectrum (in reciprocal Rydbergs) at a primary electron energy of 1 keV [85]: (1) excitation of core levels; (2) electron–electron scattering; (3) decay of plasmons. (4) is the sum of all contributions. (b) A comparison of different theoretical calculations [86, 25, 89, 60] of the secondary electron spectrum of Al for 1 keV primary electrons with experimental results [84, 30]. All curves are normalized to the maximum of the peak [107].

shown in figure 2.1a calculated from theory [85]. The curves below represent different contributions to the SE energy spectrum: core level ionization (curve 1); single particle excitation due to electron–electron scattering (curve 2); and bulk plasmon decay (curve 3). Here the main mechanism is the decay of the bulk plasmons, which can be seen from the shoulder at about 10 eV. This corresponds to the plasmon energy of 15 eV, reduced by the work function for Al of about 5 eV. The excitation of surface plasmons was not taken into account here. For comparison an experimental SE spectrum for Al is presented in figure 2.6b but for incident electrons of an energy of 100 eV.

Figure 2.1b presents a comparison of experimental results [84, 30] with several theoretical calculations [86, 25, 89, 60] of the SE spectrum of Al for a primary energy of 1 keV. All curves were normalized to unity at the maximum. Except for the calculation of Schou [89] all theories considered here show the plasmon decay peak at around 10 eV, which can also be seen in the curve representing the experimental data. In addition, there is no peak at around 5 eV corresponding to electrons which stem from the surface plasmon decay, although Kuhr and Fitting [60] explicitly considered the decay of the collective excitation of electrons at the surface.

Figure 2.2 shows a compilation of the secondary electron yield δ (i.e. the number of electrons per incident primary) as a function of the energy for an Al sample [53, 54]. The experimental data, which are represented by data points, show substantial discrepancies. On the other hand the shape of the distribution is quite similar for most experiments. This similarity can also be found for arbitrary materials [54]. Several proposals to provide an universal description of the secondary electron yield were made in the past. One equation was given by Lin and Joy [53]

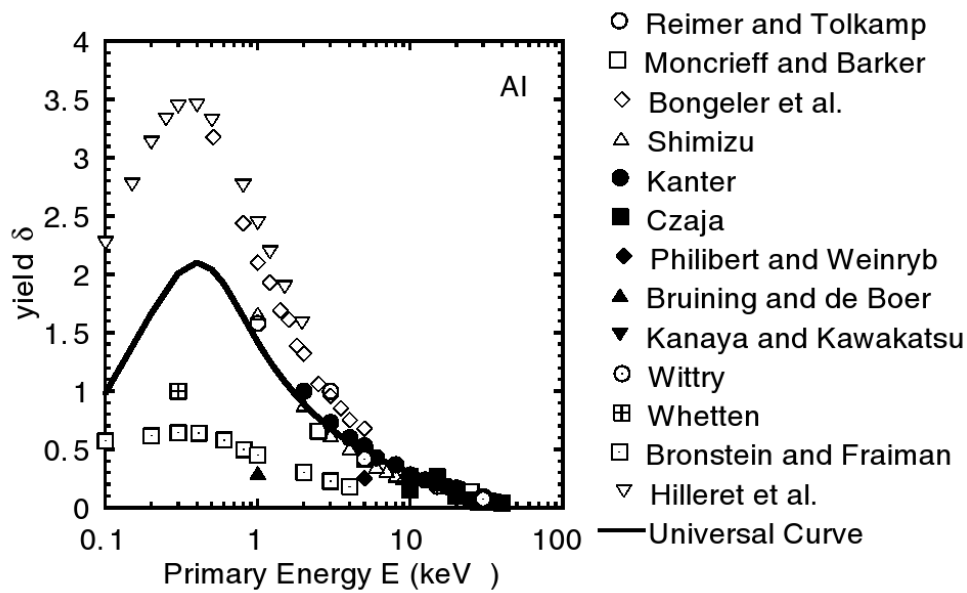


Figure 2.2: Experimental results on the primary energy dependence of the number of secondary electrons emitted, i.e. the secondary electron yield, for Al compared to the “universal” yield curve. Data points represent values from experiments taken from several sources [79, 73, 11, 90, 56, 19, 105, 13, 55, 114, 112, 12, 46], which show substantial discrepancies. The “universal” yield is calculated from eq. 2.2 using $E_m = 0.4$ eV and $\delta_m = 2.05$ and is indicated by the solid curve [107].

$$\delta(E) = 1.28 \times \delta_m \left(\frac{E}{E_m} \right)^{-0.67} \left\{ 1 - \exp \left[-1.614 \left(\frac{E}{E_m} \right)^{1.67} \right] \right\} \quad (2.2)$$

where the material dependency is represented by the maximum yield δ_m and the position of the maximum E_m [107]. Recently, Lin and Joy made a thorough examination of the SE yield as a function of the primary energy for 44 elements and determined the material dependent parameters for eq. 2.2.

2.2. (e,2e)-coincidence spectroscopy

In $(e, 2e)$ spectroscopy an incoming electron excites an electron in the solid and the scattered electron is measured in coincidence with the excited electron. Since commonly both electrons are analyzed for their energies and momenta, $(e, 2e)$ spectroscopy is a kinematically complete experiment. The recorded data is used to determine the binding energy ϵ and the momentum \mathbf{q} of the excited solid-state electron *before* the scattering event. Hence, the spectral momentum density $|\phi(\epsilon, \mathbf{q})|^2$ is obtained. $(e, 2e)$ spectroscopy is therefore also referred to as electron-momentum spectroscopy [69]. An overview of this technique is presented by M. Vos in reference [103] and summarized below.

$(e, 2e)$ spectroscopy was developed over the last 30 years by several research groups. First experiments were conducted by Amaldi *et al.* in 1969 [2] followed by work of Camillon *et al.* [15] and Persiantseva *et al.* [77]. The bad energy resolution obtained in the first experiments was gradually improved over the years as well as the low countrate [96]. $(e, 2e)$ spectroscopy is used to address various questions in solid-state physics especially regarding the band structures of solids.

To achieve sufficient momentum and energy resolution a well-collimated monoenergetic electron beam of the energy E_0 and momentum \mathbf{p}_0 is required. In $(e, 2e)$ spectroscopy one is commonly interested in electron-electron collisions involving large momentum transfers, which allows to describe this collision as binary collision. The target electrons is ejected due to the transfer of energy and momentum of the impinging electron. For further considerations \mathbf{p} will refer to electron momenta as determined outside the solid and \mathbf{q} to real momenta of the electrons before the scattering process. Energies and momenta of the electrons are determined in coincidence (E_f and \mathbf{p}_f for the faster of the two electrons, and E_s and \mathbf{p}_s for the slower one). Figure 2.3b presents the relation between the different momenta.

The momentum and the energy of the ejected electron before the collision can be determined by comparing energies and momenta of scattered, ejected and incident electrons. The binding energy ϵ is derived as

$$\epsilon = E_0 - E_s - E_f \quad (2.3)$$

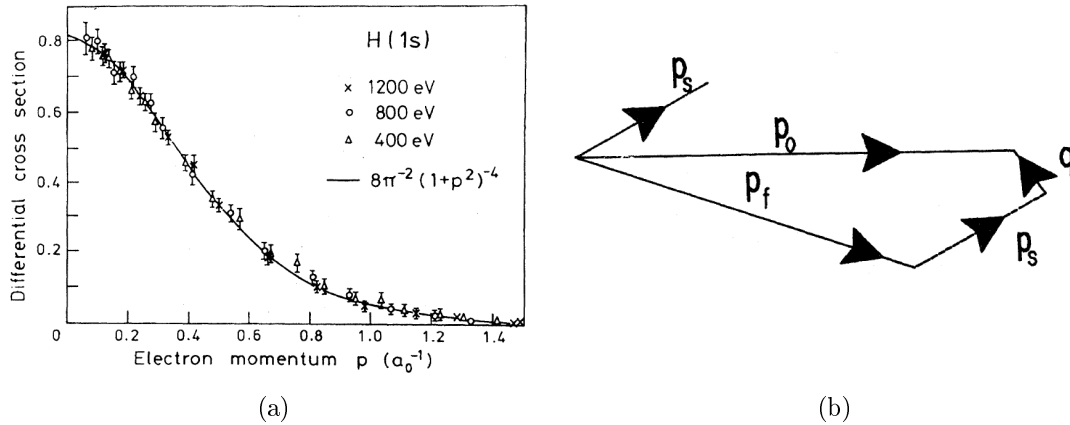


Figure 2.3: (a) shows a comparison of experimental and theoretical results of the differential cross section for atomic Hydrogen. The momentum density $|\phi(\epsilon, \mathbf{q})|^2$ was determined experimentally (data points) for several energies and arbitrarily normalized. It can be seen that the energy of the primary particles has no influence on the momentum density as expected. The exact theoretical solution is represented by the solid line and agrees well with the experiment [66]. In (b) the different momentum components involved in an (e,2e)-experiment are presented [103].

The free electrons can be described by plane waves if they are sufficiently fast and the momentum of the ejected electron before the collisions is then given by (compare figure 2.3b)

$$\mathbf{q} = \mathbf{p}_0 - \mathbf{p}_s - \mathbf{p}_f \quad (2.4)$$

In consequence, the spectral momentum density $|\phi(\epsilon, \mathbf{q})|^2$ can then be derived.

The differential cross section at the energy ϵ for the scattering process from electrons in the orbital a with the binding energy ϵ_a is in the plane-wave Born approximation given by

$$\frac{d^5\sigma}{d\Omega_s d\Omega_f dE_f} = (2\pi)^4 \frac{p_f p_s}{p_0} f_{ee} |\phi_a(\mathbf{q})|^2 \delta(\epsilon - \epsilon_a) \quad (2.5)$$

where f_{ee} is the Mott cross section

$$f_{ee} = \frac{1}{(2\pi^2)^2} \left(\frac{1}{|p_0 - p_f|^4} - \frac{1}{|p_0 - p_s|^2 |p_0 - p_f|^2} + \frac{1}{|p_0 - p_s|^4} \right) \quad (2.6)$$

Figure 2.3a shows a comparison of experiment and theory for the (theoretically) simplest case of the Hydrogen atom ground state [66]. Differential cross sections for various energies of the incoming electron were determined in this experiment. The soundness of (e,2e) spectroscopy is proven by the fact that all experimental differential cross sections coincide disregarding the energy of the primary electron, since the momentum densities are independent of the experimental conditions.

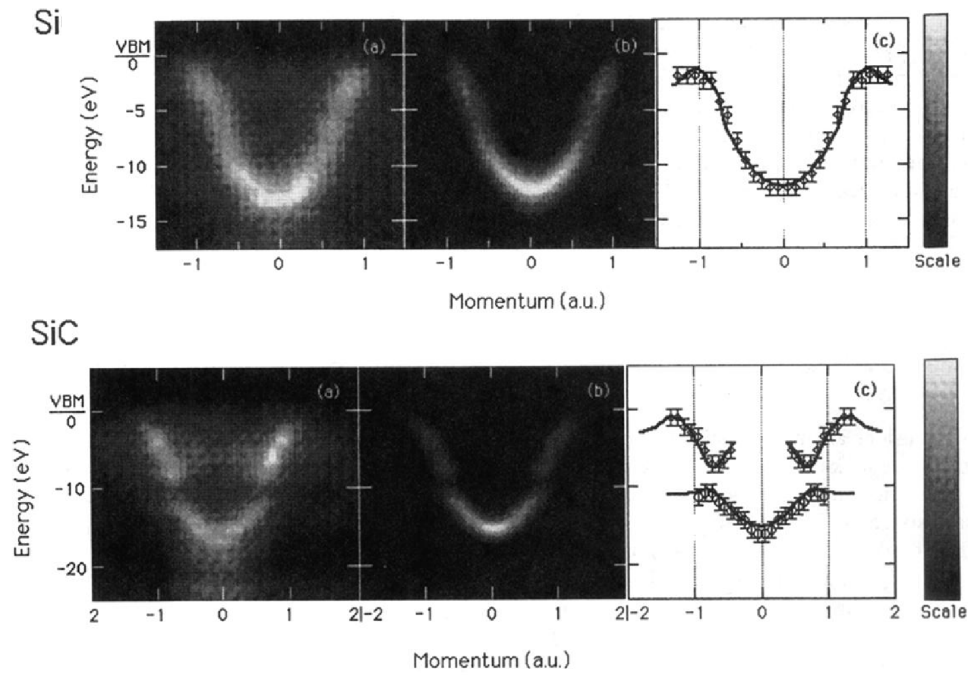


Figure 2.4: Comparison between theoretical and experimental spectral momentum density for amorphous Si (top figure) and amorphous SiC (bottom figure). Top row: (a) is a grey-scale plot of the measured spectral momentum density of amorphous Silicon. The shading is proportional to the intensity. (b) is the calculated spectrum for polycrystalline Silicon. (c) shows the comparison of experimental and theoretical dispersion relations [104]. The bottom row presents a similar comparison of experimental and theoretical data for SiC. A band gap around 10 eV binding energy can be observed [14]. Figures taken from ref. [103].

Figure 2.4 presents an application of the $(e, 2e)$ spectroscopy. In figure 2.4a the measured spectral momentum density of Si (top) [104] and SiC (bottom) [14] are shown in grey-scale plots. Both, Si and SiC, were amorphous due to the preparation of the samples [103]. Momentum-energy combinations of high intensities are represented by lighter shading. Next to this plot calculations using the linear muffin-tin potential approach [91] are depicted. The experimentally determined and calculated dispersion relations are almost identical as can be seen in figure 2.4c. The bottom row shows the results for SiC as an example of a solid displaying two separate filled bands separated by a gap. For Si this gap can't be observed due to symmetry reasons peculiar to solids in three dimensions as explained in ref. [43].

2.3. Experiment

The coincidence experiments on an Al (100) single crystal were conducted on a new apparatus originally developed for electron and ion spectroscopies at the Department of Physics of the Università di Roma Tré. A short description of this apparatus is given in ref. [87] and summarized below.

The design of the apparatus is presented in Figure 2.5. The UHV chamber contains an electron gun, a sample manipulator and two electron analyzers. The electron gun from Varian has programmable power supplies in order to perform automatic scans for electron energies from 50 to 600 eV. The electron gun provides electrons of a incident energy with a reproducibility of ± 500 meV and a precision of ± 1 eV. The sample manipulator is a commercial VG model HPT-WX. The hemispherical electron analyzers are custom built including the electrostatic lenses. The angular resolution of the analyzers is 1.5° full width half maximum (FWHM) and the energy resolution is 400 meV for a pass energy of 20 eV.

In the experiment described in this work, secondary electrons were measured in coincidence with features of the inelastic tail of the elastic peak. The angle of the incident electrons was 30° with respect to the surface normal. The elastic peak and its inelastic features were measured by spectrometer A in specular reflection. The secondary electron energy region is scanned by spectrometer B, whose axis and the surface normal include 60° . The energy of the incident electrons was 100 eV. An Al (100) single crystal was used for the experiments. Every morning the crystal was prepared in the UHV chamber by consecutive sputtering and heating cycles.

Similar to APECS (see section 1.2.1) two electrons are considered belonging to the same scattering event if the time difference of detection corresponds to their energy difference. Again, there is no way to distinguish between true and false coincidences. The parameters of the experiment (e.g. the incidence flux) have to be optimized in a way that the ratio of true to false coincidence events is at a maximum.

Figure 2.6a shows the experimental singles spectrum (i.e. electrons measured in a common non-coincidence experiment) of the elastic peak and its inelastic tail. In the inset at the top left the inelastic features of Al are enlarged. The bulk plasmon peak at ~ 85 eV and surface plasmon peak at ~ 89 eV can clearly be distinguished. The experimental singles secondary electron spectrum is presented in figure 2.6b. Note the shoulder at about ~ 9 eV. The singles spectrum compares well with the experimental spectra in figure 2.1a and figure 2.1b.

Two series of coincidence experiments were conducted for Al (100). In the first series the secondary electron spectrum was measured in coincidence with the surface plasmon peak, i.e. primary electrons which excited a surface plasmon. Here, one spectrometer is fixed on the energy of the surface plasmon peak (~ 89 eV) while the other spectrometer scans through the energy region of the secondaries. Thereafter, the secondary electrons

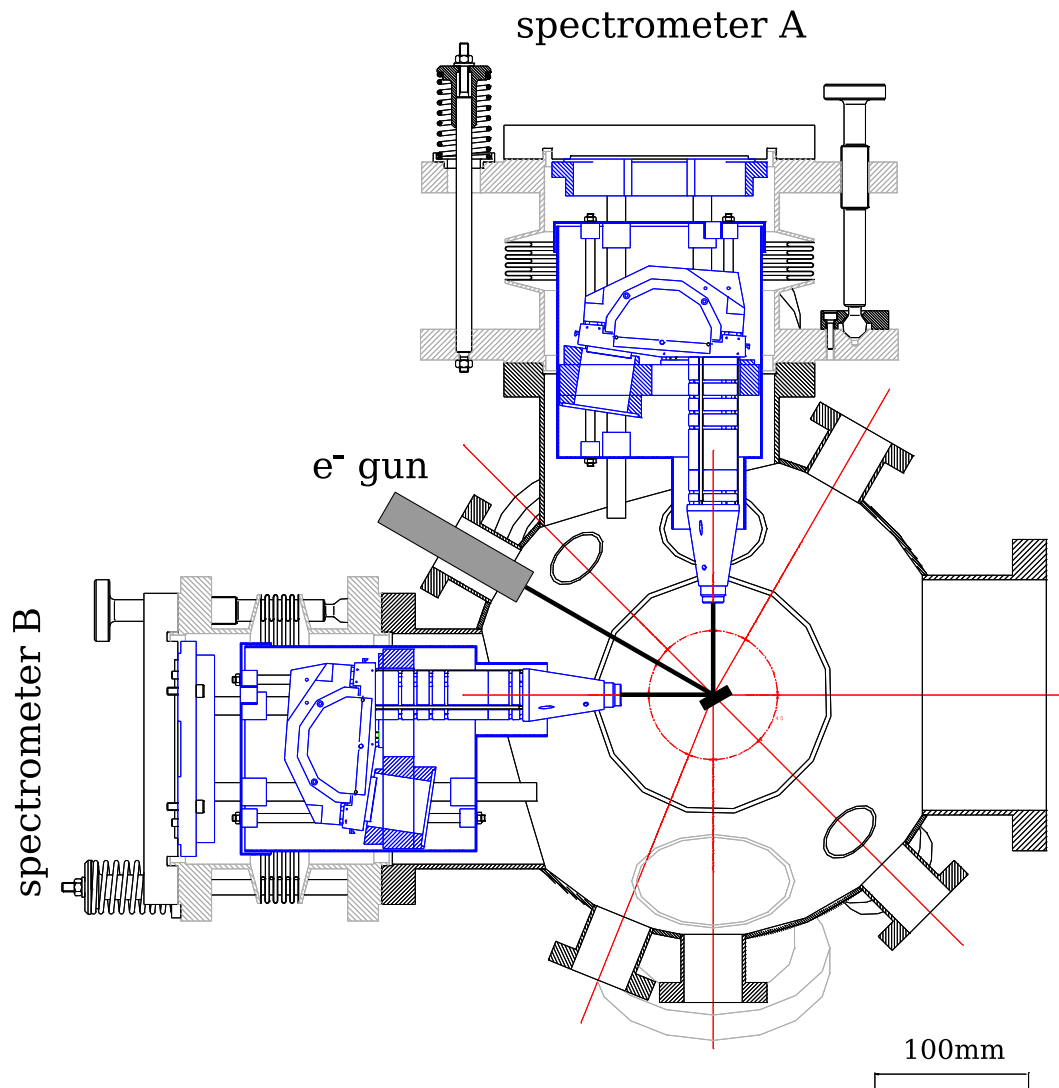
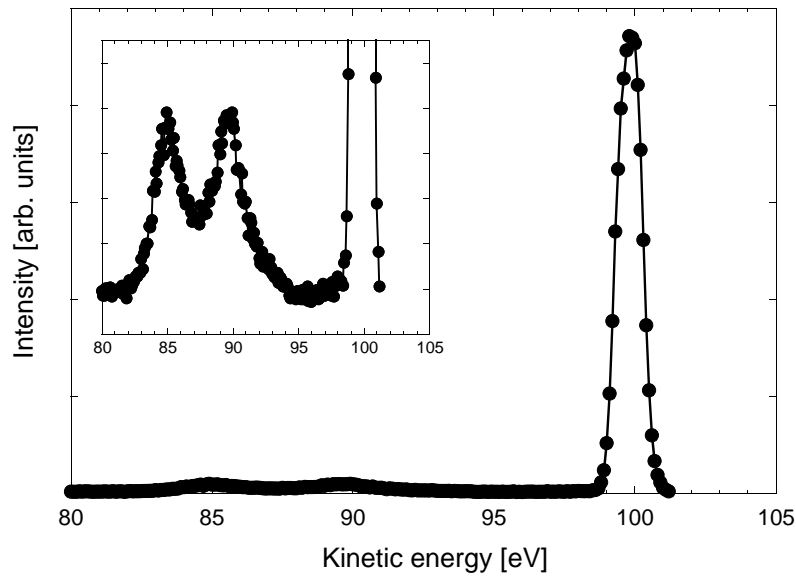
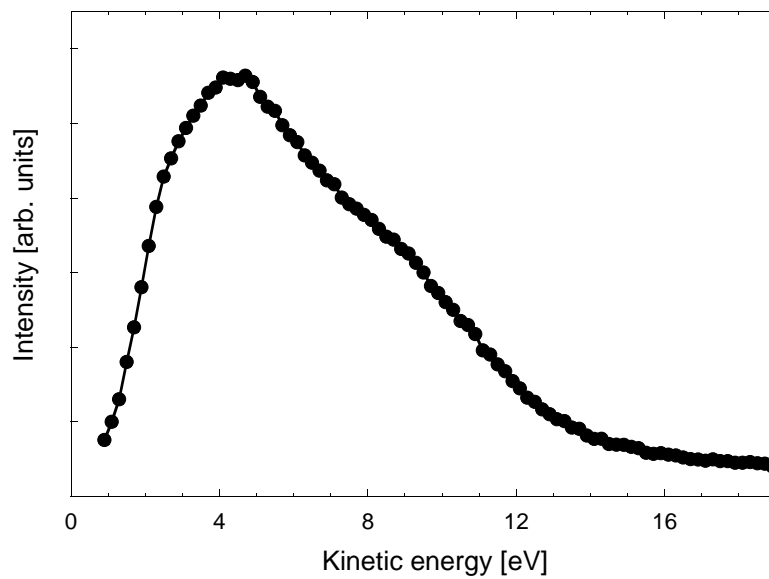


Figure 2.5: This drawing shows the apparatus used for the $(e, 2e)$ -coincidence experiment. The electron gun can provide electrons of an incident energy between 50 and 600 eV. The hemispherical electron analyzers have an angular resolution of 1.5° and an energy resolution of 400 meV (for a pass energy of 20 eV). The angle between surface normal and incident electrons is 30° . In the experiment presented in this work spectrometer A measures the elastic peak and the near energy loss region in specular reflection, while the secondary electrons are measured with spectrometer B. The angle between surface normal and the axis of spectrometer B is 60° . All devices are mounted in an UHV chamber.



(a)



(b)

Figure 2.6: Plot (a) shows the experimental singles spectrum of the the elastic peak and its inelastic tail for Al (100). The inelastic features are enlarged in the inset at the top left. The surface plasmon peak and the bulk plasmon peak can be clearly distinguished. The secondary electron energy distribution is presented in plot (b). At ~ 9 eV a shoulder can be recognized. The shape of the spectrum compares well to the spectra shown in figures 2.1a and 2.1b.

spectrum was measured in coincidence with the bulk plasmon peak, i.e. primary electrons which suffered a bulk plasmon loss. It should be pointed out that in contrast to the common $(e, 2e)$ experiments, the momenta of the electrons were not separately evaluated.

The coincidence rate reached in this experiment was below 0.01 Hz. Hence, the duration of the experiments was several weeks to achieve acceptable statistics. Note, that this experiment is only possible due to the pronounced inelastic loss features of Al. For other materials where this is not the case the secondaries need to be measured in coincidence with the whole energy range of the inelastic tail of the elastic peak. This would be impossible due the low coincidence rate.

2.4. Results

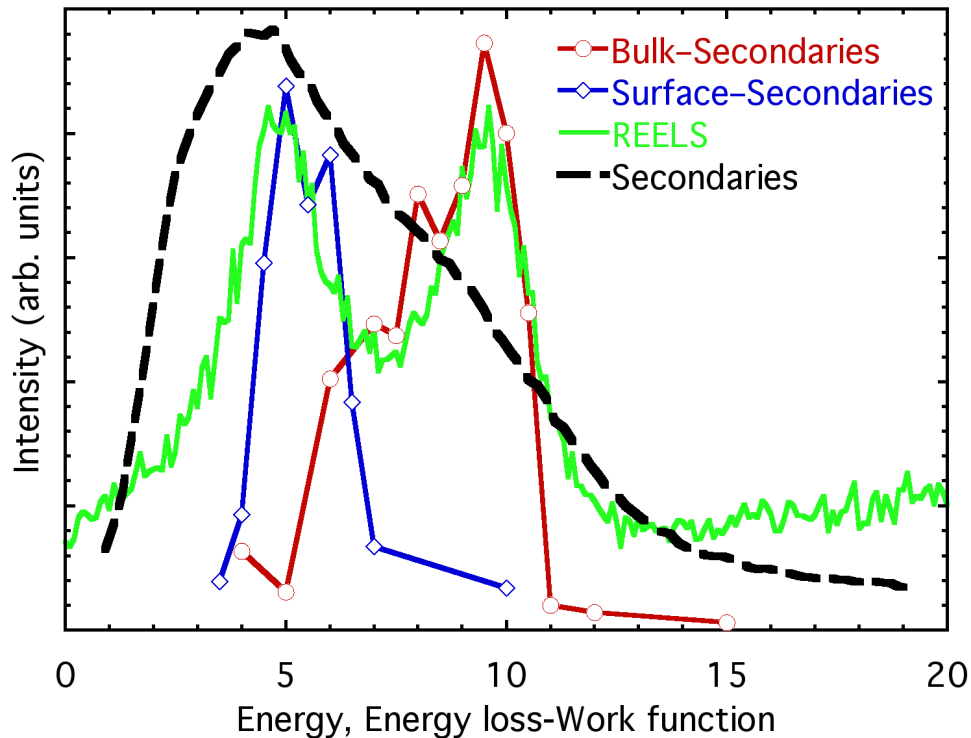


Figure 2.7: Experimental secondary electron spectrum (dashed curve) for 100 eV electrons incident on an Al (100) surface. The solid line represents the corresponding Reflection Electron Energy Loss Spectrum (REELS). The energy offset for the energy loss scale of the latter spectrum is the work function of the spectrometer, which is taken to be 5.5 eV. The open circles and diamonds represent the secondary electrons that are emitted in coincidence with the single volume and bulk plasmon loss features in the REELS.

Figure 2.7 shows the results of the $(e, 2e)$ -experiments for 100 eV incident electrons on

an Al (100) single crystal. The dashed line shows the experimental singles secondaries spectrum. The SE spectra in coincidence with the surface and bulk plasmon peak are represented by the blue (squares) and red (circles) lines respectively. For all three plots the x -axis represents the kinetic energy. The solid line (green) shows the singles REELS spectrum. Here, the x -axis is the binding energy where the work function of the spectrometer is subtracted. This allows to compare the position of the surface and bulk plasmon peaks of the REELS spectrum with the corresponding features in the coincidence spectrum directly.

The coincidence spectra show the energy distribution of the SE which originate from the decay of surface and bulk plasmons respectively. It can be seen that the peaks in the coincidence spectra are at the same position as the corresponding peaks of the REELS spectrum (in binding energy). The position of the peak in the bulk plasmon coincidence spectrum corresponds well to the shoulder in the singles SE spectrum. Both peaks in the surface and bulk plasmon coincidence spectrum are quite narrow. From the position and the shape of the peaks in the coincidence spectra one can conclude that the energy of a plasmon is transferred to one electron during the decay, in other words, the plasmons decay mostly in one electron-hole pair. For further investigation of the experimental results Monte Carlo (MC) calculations were conducted.

2.5. Comparison to Monte Carlo simulation

Monte Carlo (MC) simulations were performed with the usual algorithm, described in detail in ref. [118]. The trajectory of the primary particle is modelled by means of the so-called direct simulation model in which each individual scattering process is explicitly modelled. For the elastic differential cross section the data in ref. [48] were used, while the distribution of energy losses in a single volume and surface scattering process was calculated using linear response theory employing the optical data taken from Palik's book [26]. The total mean free path are used to generate steplengths in between collisions, which are assumed to follow Poisson statistics. Comparing a random number between zero and unity with the ratio of the inelastic mean free path and the sum of the elastic and inelastic mean free path is used to determine the type of scattering. The probability for one or more surface excitations is generated from the total surface excitation parameter taken from ref. [110], assuming that the probability for plural surface scattering is distributed according to the Poisson stochastic process. It is assumed that the energy lost by the primary particle during each inelastic event is transferred to the sea of loosely bound solid state electrons, eventually giving rise to creation of one or more secondary electrons. In the case of a volume loss, the position of secondary electron creation is taken to coincide with the position where the loss occurred, in the case of a surface loss the location of creation is drawn from an exponential distribution with a characteristic length equal to the width of the surface scattering zone v/ω_s , where v is the electron speed and ω_s is the surface plasmon frequency. The average number of

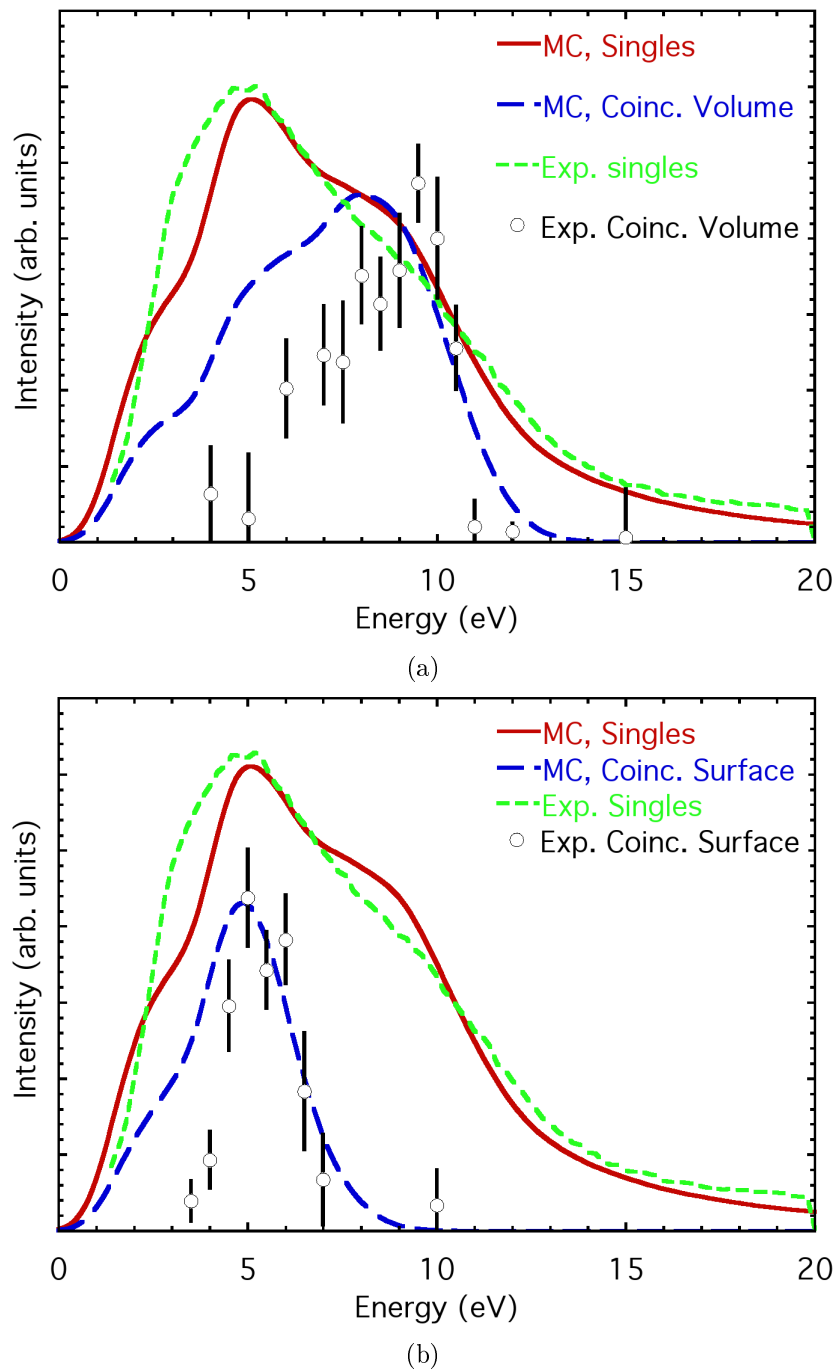


Figure 2.8: Comparison of the experimental data with results of model calculations. Short dashed curve: experimental singles secondary electron spectrum. Solid curve: simulated secondary electron spectrum. Data points with error bars: experimental secondary electron spectra measured in coincidence with the surface (plot a) and volume loss features (plot b) in the REELS spectra. Long dashed curved: corresponding simulated coincidence secondary electron spectra.

secondary electrons created in any loss is used as a free parameter of the model, the actual number released is generated using the Poisson stochastic process. The model calculations agree best with the experimental observations when the average number of secondaries created in a volume or surface inelastic collision is about 1. The energy released during the energy loss process of the primary particle is shared uniformly over all created secondaries. The emission direction distribution of the secondaries is taken to be isotropic. The trajectories of the secondaries are then generated in the usual way, additional loss processes leading to creation of additional electrons that are treated in exactly the same way, in consequence modelling the cascade of secondary electrons. When a secondary electron crosses the surface, its transmission probability is calculated using the formula [60]:

$$T = \frac{4 \left(1 - \frac{W}{E \cos \alpha}\right)^{1/2}}{\left[1 + \left(1 - \frac{W}{E \cos \alpha}\right)^{1/2}\right]^2} \quad (2.7)$$

where W is the work function and E is the actual energy of the particle. If the particle remains inside the solid its refraction angle is calculated using Snell's law. Each secondary electron that is emitted from the surface when the corresponding primary particle is also detected and has suffered a single volume or surface loss, is added to the corresponding histogram of surface and volume loss coincidence spectra.

Figures 2.8a and 2.8b show the result of the MC simulations of secondaries in coincidence with the bulk and surface plasmon respectively. The experimental and simulated singles SE spectrum shown by the short dashed line and the solid line respectively compare well quantitatively. Still, the shoulder at ~ 9 eV is overestimated. The shoulder at 2 eV in the MC calculations can not be seen in the experimental spectrum. The agreement between experimental (data points) and simulated data (long dashed line) of both the surface and bulk plasmon coincidence spectra is qualitatively satisfying. In both cases the low energy side of the peak is overestimated, which means that either the assessment of the collision cascade or of the average number of electron-hole pairs created during the plasmon decay process is too high.

2.6. Summary

$(e, 2e)$ coincidence experiments on an Al (100) single crystal were conducted to investigate the decay of surface and bulk plasmons excited by incident electrons. The SE were therefore measured in coincidence with reflected electrons which suffered an inelastic collision and excited either a surface or bulk plasmon. In addition MC calculations were carried out to gain insight about the cascade process following the plasmon decay. From the shape and the position of the peaks in the coincidence spectra one can draw the conclusion that plasmons decay mostly in one electron-hole pair. From comparison

of the MC calculation with the experimental data it can be assumed that the collision cascade is not of major importance for the emission of SE.

3. Ion induced Emission of Electrons from Surfaces

In the former chapters the emission of electrons from the surface due to photons or electrons impinging on a solid sample were discussed. It is a well known fact, that ion bombardment of surfaces can also lead to emission of electrons. The underlying processes of ion–solid interaction which leads to electron emission are much harder to understand, due to the structure of an ion compared to the fundamental particles like photons or electrons.

In the first section of this chapter the basic theory of ion–induced emission of electrons from surfaces is presented. Here, the two different processes which lead to electron emission due to ion–solid interactions are described: the kinetic emission (KE) and the potential emission (PE) process. KE is caused purely by the kinetic properties of the incoming projectile. PE on the other hand is due to the Coulomb potential of the incoming ion.

In order to study these emission processes a new kind of magnetic–field time–of–flight electron spectrometer was designed and built. This spectrometer is able to determine the energy and momenta of the emitted electrons from a solid surface and is therefore kinematic complete. In addition, this spectrometer allows to determine the kinematic properties for up to 14 electrons for one single incident event. This enables one to conduct coincidence experiments for pulsed electron emission processes from solids. This spectrometer is called “Momentum Vector Electron Spectrometer” and the aspects of this spectrometer is presented in the following sections in some detail.

In addition, an ultra–short pulsed ion source had to be designed and built as well. Here, a Cs⁺ thermionic ion gun was chosen as ion source. The continuous ion beam was pulsed by an electric–field ion chopper in order to produce nano–second pulses. For first test experiments a polycrystalline Au sample was chosen to investigate Cs⁺ induced electron emission from Au. First results of these experiments are presented at the end of this chapter.

3.1. Theory of ion-induced electron emission

In this section a brief introduction of the theory of electron emission induced by ion bombardment of a solid is given. A more detailed overview of this topic is given elsewhere (e.g. [42, 5, 59]). One quantity of great significance in this theory is the total particle induced electron emission yield, which is defined as

$$\gamma = \frac{N_e}{N_i} \quad (3.1)$$

where N_e is the number of electrons which were emitted into the vacuum above the surface, while N_i is the number of incident particles [42]. γ is strongly dependent on the angle of incidence ϑ with respect to the surface normal. Therefore, also the surface roughness has a strong impact on the electron emission yield.

One can further define the single differential yield $d\gamma/dE$, which is also known as the energy spectrum $N(E)$, and the double differential yield $d^2\gamma/dE d\Omega$, i.e. the energy and angular distribution.

The knowledge of the electron yield is of major importance for many applications in physical research, e.g. fusion research or plasma technology, but it reveals no information about the mechanisms on which the electron emission is based on. Theoretical models need to explain the emission yield not only qualitatively but also quantitatively.

Two processes are assumed to be responsible for the emission of electrons when a particle strikes a surface: kinetic and potential emission. For the kinetic emission process (KE) it is presumed that the penetrating projectile loses energy in a series of interactions with the solid described by a statistical process. In the very low energy region this is the dominant process for singly charged ions. Potential emission (PE) of electrons can occur if the projectile carries potential energy, which at least as a first approximation is not dependent on the kinetic energy of the projectile. This process will not take place for neutral atoms, except if electrons are occupying excited states.

3.1.1. Kinetic emission

Kinetic emission (KE) of electrons is a process which is caused purely by the kinetic properties of the impinging projectiles. KE of electrons due to the impact of primary electrons is far better understood as for incoming atoms and ions, since the latter ones are far heavier and structured particles. The description of the KE process below is generally applicable to electrons, ions and atoms.

All theoretical models separate the process of KE of electrons into

- generation of excited electrons in the bulk and surface region,

- transport of the electrons to the surface and
- escape over the surface barrier.

It is generally assumed that these sub-processes are independent from each other.

Kinetic generation of excited electrons

There are two different processes during which excited electrons are produced. First, direct collisions between projectiles and target electrons and/or atoms lead to excitation of valence band electrons into free states above the Fermi level. Hence, target atoms or projectiles are ionized. Secondly, several secondary processes like cascade multiplications of already excited electrons while traveling through the solid, excitation due to recoil atoms and backscattered projectiles, photon emission, and plasmon decay also lead to the creation of excited electrons.

The various excitation mechanisms are rather complicated from the theoretical point of view. Therefore, for the electron production due to KE semi-empirical theoretical approaches are usually applied [42]. One approach is to assume a proportionality between the electron yield and the mean energy loss of the primary particles in the solid [8]. Although all excitation mechanisms are included in this approach statistically, the proportionality factor remains only a crude estimate.

For primary electrons or ions with high energy it is assumed that electrons of the conduction band at the Fermi edge as well as inner-shell electrons are excited. The situation gets more complicated if the energy of the primary particle is decreased until the threshold of KE is reached. From the several theoretical approaches to explain this threshold [42, 75] one can deduce that the motion of the free electrons (according to the Fermi statistics) need to be taken into consideration.

The kinetic emission of an electron is only possible if it gains enough energy to overcome the surface potential barrier. Assuming that the conduction band electron has the maximum possible energy E_F (Fermi energy) the maximum energy transfer possible amounts to [8]

$$T = 2m_e v_p (v_p + v_F) \quad (3.2)$$

Here, m_e is the reduced mass of the electron, v_p the velocity of the primary projectile and v_F is the velocity of the electrons at the Fermi edge. To derive eq. 3.2 a hard-sphere head-on collision between the electron travelling with v_F in opposite direction of the projectile moving with v_p is assumed. This case leads to the maximum transfer of energy to the electron. The order of magnitude of the threshold velocity of the projectile below which no KE is possible according to eq. 3.2 is about 10^5 m/s [63].

In addition, the excited electron has to overcome the surface potential barrier W_b . If

eq. 3.2 is changed accordingly we obtain for the threshold velocity

$$v_{th} = -\frac{v_F}{2} \left[\left(1 + \frac{2W_b}{mv_F^2} \right)^{1/2} - 1 \right] \quad (3.3)$$

For all projectiles slower than this threshold velocity v_{th} no KE occurs. This simple theory works well for light atoms like Hydrogen and predicts the threshold velocity satisfactorily. For heavy atoms KE was already observed below the threshold velocity [63]. These observations can be explained by the introduction of quasi-molecular effects since the assumption of a simple head-on collision doesn't hold for heavy particles. Other effects, like the Pauli-excitation [1] decreases the threshold further. A more detailed model describing the threshold of KE for heavy particles can be found in reference [63].

Transport of electrons to the surface

The transport of electrons in the solid is independent of how they were excited and therefore the situation is similar to electron-induced (see section 2.1) or photon-induced electron emission. A very detailed review about the transport of medium energy electrons in solids can be found in a tutorial review article of Werner [118].

On their way to the surface electrons suffer several elastic and inelastic collisions. In consequence the initial direction and energy of the electrons are changed. Taking this into consideration, the transport of the electron in the solid is described by a Boltzmann like transport equation [118]. On their way to the surface electrons may transfer part of their energy to other loosely-bound solid state electrons, which in turn leads to a formation of a collision cascade. Also, as was explained in section 2.1, the theory of the transport of electrons in the low energy region is much more involved. In addition, due to the difficult experiments in this energy region many quantities are not determined with sufficient accuracy. Simplified approaches to describe the transport of electrons in solids are usually applied here. The straight line approximation neglects elastic scattering and the probability P to leave the surface for an electron of the energy E without energy loss excited at the depth z which moves in the direction ϑ with respect to the surface normal is given by [118]:

$$P(z, E, \vartheta) = \exp \left(-\frac{z}{\lambda_i(E) \cos \vartheta} \right) \quad (3.4)$$

where $\lambda_i(E)$ is the inelastic mean free path (IMFP, e.g. the average path an electrons travels until it suffers an inelastic collision). Especially for the low energy region where the transport mean free path (TMFP, i.e. the average path an electrons travels until it experience a severe change in direction) is much smaller than the IMFP, elastic scattering must be taken into consideration. Therefore as a first improvement of eq. 3.4 λ_i is replaced by a mean free path λ , where the effects of the inelastic and elastic scattering are included approximately. A more sophisticated theory of electrons transport in solids is presented by Schou in reference [89].

The experimentally determined average escape depth of ion induced electrons is between 5 and 20 Å. Hence, excited electrons stem mainly from the surface region of the solid.

The surface barrier

A simple model for the surface barrier is the assumption of a semi-infinite solid defined by a planar surface with a mean work function ϕ_W . The energy level of the surface barrier calculates then to $W_b = E_F + \phi_W$, where E_F corresponds to the Fermi edge. Here, the reference for E_F is the bottom of the conduction band. Simple considerations about the scattering of the particle at this barrier sets the energy and direction of the particle in- and outside in relation [89].

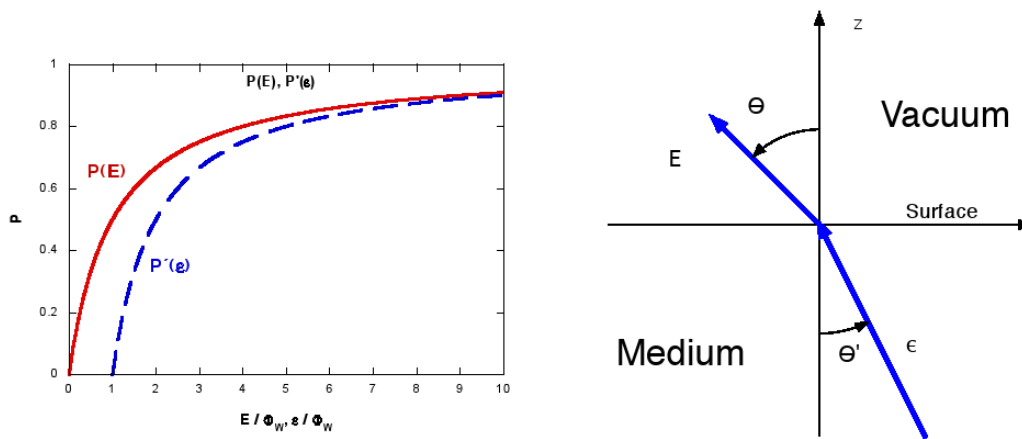


Figure 3.1: In the left plot the probability for particles to cross the surface barrier are shown. The escape probability is shown as a function of the energy of the particle inside the solid ϵ and as a function of the kinetic energy outside the solid E . Both energies are set in relation to the work function ϕ_W . At the right a schematic drawing shows the basic kinetic relations of the particle movement inside and outside the solid (figures taken from [59]).

The surface barrier is also responsible for total reflection of particles which come from inside the solid. The probability $P(E)$ for the particle to overcome the surface barrier, assuming an isotropic angular distribution of the electrons inside the solid, is [42]

$$P(E) = \left(1 - \frac{W_b}{\epsilon}\right) = \left(1 + \frac{W_b}{E}\right)^{-1}$$

where ϵ is the electron's energy inside the solid with respect to the bulk's binding energy and $E = \epsilon - W_b$ the kinetic energy of the electron outside the solid (see figure 3.1). For an isotropic angular distribution of the electrons inside the solid, the angular distribution of the emitted electrons follows a cosine law which can be explained with the particle flow conservation at the surface.

The total yield due to kinetic emission

Baragiola *et al.* [8] derived an expression for the total KE yield for incident particles well above the threshold energy (see eq. 3.3)

$$\gamma = \frac{P\lambda_m}{E_i} \frac{dT}{ds}(E) \quad (3.5)$$

where P represents the average escape probability of the excited electrons, λ_m is the mean escape depth and E_i the mean energy necessary to produce an electron-hole pair inside the solid (ionisation energy). We also introduced the mean energy loss T per unit pathlength s , the so-called stopping power $dT/ds(E)$. The main statement of this equation is the direct proportionality of the total yield γ to the stopping power $dT/ds(E)$. Equation 3.5 is valid for particle energies well above several 10 keV for many metal targets [42]. For lower energies this equation is not valid anymore, since one of its requirements, that the energy deposited by the projectile within λ_m is small compared to the initial kinetic energy of the projectile, doesn't hold anymore. Additionally, the electronic stopping power is a not well investigated quantity for low velocities.

A simple law is given within the Parilis-Kishinevsky Theory [75] for the total emission yield

$$\gamma = \rho\sigma_e\lambda_i P$$

Here, normal incidence of the incoming projectiles is assumed. ρ denotes the atomic density of the target, λ_i the inelastic mean free path of the secondary electrons and P is again the average electron escape probability. σ_e is the binary collision cross section. In this theory it is assumed that the main contribution to the KE is a two-step process, where binary collisions lift core electrons slightly above the Fermi level. Subsequently an Auger transition releases a valence electron into the vacuum. The binary collision cross section is given by

$$\begin{aligned} \sigma_e(v) = & \frac{1.16a_0h}{E_i} \left[(Z_1 + Z_2) \left(Z_1^{1/2} + Z_2^{1/2} \right)^{-1} \right]^2 v \\ & \times \arctan \left[0.6 (v_p - v_{th}) 10^{-7} \right] \end{aligned} \quad (3.6)$$

Here, a_0 is the Bohr radius, h the Planck constant, E_i is the ionisation energy, Z_1 and Z_2 are the atomic numbers of the projectile and target atom respectively, v_p is the velocity of the incoming projectile and v_{th} is the threshold velocity. It should be pointed out, that the total yield γ is proportional to the impact velocity v_p near the threshold velocity v_{th} .

Winter *et al.* [113] derived an expression for the total yield for neutral atoms as incoming particles and velocities close to the threshold

$$\gamma \approx (v - v_{th})^2$$

where only kinematic binary collisions between the incoming projectiles and the quasi-free valence electrons are taken into consideration, neglecting any peculiarities of the excitation and emission processes.

3.1.2. Potential emission

Beside the kinetic emission of electrons there is also another completely different process which leads to the release of electrons from the surface during ion–solid interaction. This process is called potential emission (PE) of electrons and is caused by the Coulomb potential of the incoming ion. During an ion–solid interaction electrons are emitted even if the ion never penetrates the solid. This is in contrast to the KE process which takes place inside the solid. Since only the Coulomb potential of the ion is the origin of the electron energies, PE can never occur for neutral atoms if they are not excited. Hagstrum presented a theory of PE in reference [40], which is regarded as the standard description of this effect.

An ion with the charge q has the potential energy

$$V_q = \sum_{j=0}^{q-1} E_i^{(j)}$$

where $E_i^{(j)}$ corresponds to the ionization energy of an atom in the charge-state j .

Overview of possible transitions

In reference [42] various different transition mechanisms were listed which might occur if an ion moves in the front of a surface of a solid. The energy levels of the occupied and vacant states of the ion or excited atom and the distance d_p between the projectile and the surface influence these mechanisms.

Figure 3.2 shows schematic drawings of possible electronic transitions for ions moving in front of the surface. Since the extent of excited states is much larger than the one of the ground states resonant transitions can occur for large distances of the projectile to the surface. These transitions are generally precursors for subsequently possible electron emitting two–electron (Auger) transitions.

Several transitions where only one electron is transferred will be described first. Resonance neutralisation (RN, see figure 3.2a) comprises electron transfer from the surface valence band into free states of the ion in front of the surface. There is only a finite probability for this process if the initially unoccupied final state is energetically favourable compared to electrons in the valence band. The inverse process is the resonant ionisation (RI, see figure 3.2a), which is only possible if the binding energy of an occupied state in the ion is smaller than the surface work function ϕ_W . Another possible transition can take place if the atomic orbitals of the core states and the projectile's states overlap each other, hence, this is only possible in close collisions. This process is called the quasi–resonance neutralisation (QNR).

There are also transitions where two electrons are involved in the process. These processes are called Auger transitions. All of them take place during a very short period of time of

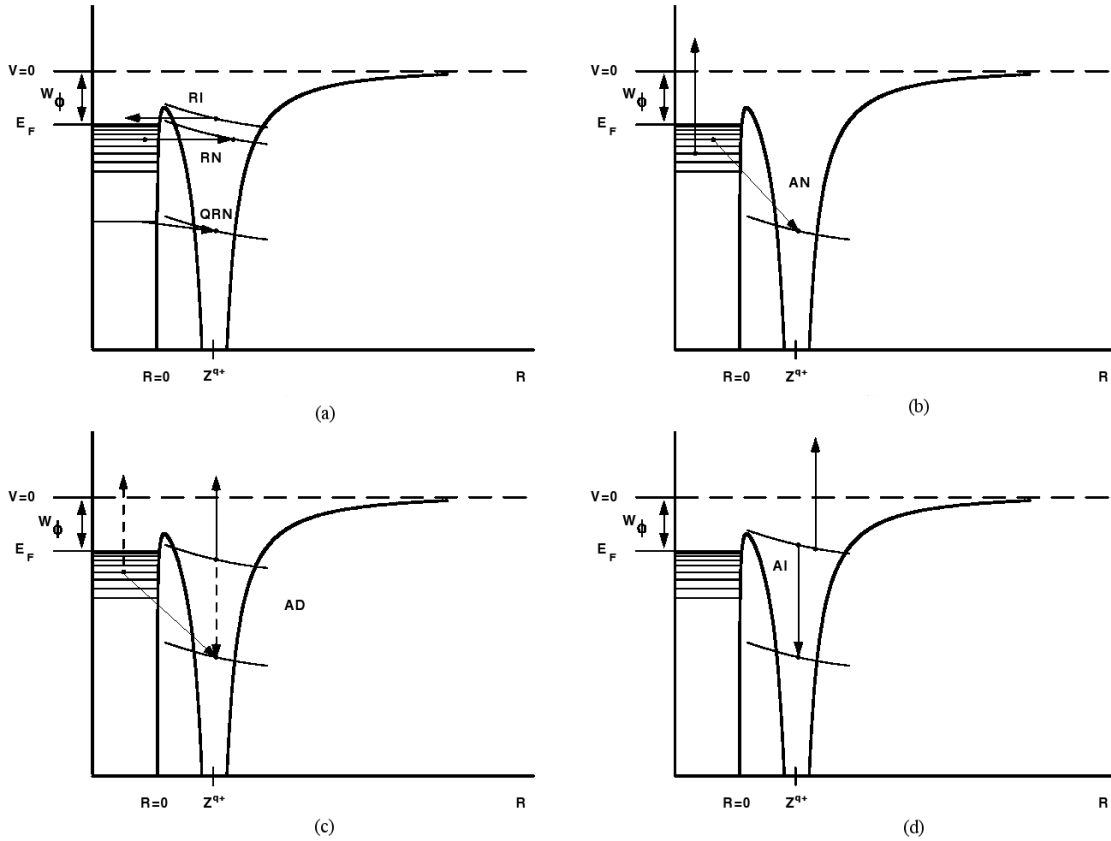


Figure 3.2: Schematic drawings of possible transitions of electrons for ions moving in front of a surface. Figure (a) shows resonant and quasi resonant transitions, while Auger transitions are shown in (b) – Auger neutralisation, (c) – Auger de-excitation and (d) – auto ionisation. Solid arrows indicate the direction of the transition. The valence band is depicted by the horizontal lines up to the Fermi Level E_F . W_ϕ is the work function. Energy level of the ions are shifted with decreasing distance to the surface due to image charge effects (Figure taken from [5]).

about 0.1 to 100 fs. The process where one electron fills directly the vacant ground state of the projectile ion and the corresponding energy is transferred to another electron of the valence band so that it can overcome the work function is called the Auger neutralisation (AN). This process is shown in figure 3.2b. Since only the ionisation energy W_i^* reduced by the work function ϕ_W will become available during the neutralisation, W_i^* must be at least twice the work function ϕ_W for the second electron to be liberated into vacuum. The kinetic energy E of the released electron amounts to

$$E \leq W_i^* - 2\phi_W$$

The effective neutralisation energy W_i^* depends on the distance d_p between the projectile and the surface due the level shift according to the interaction with its image charge.

A similar process is the Auger de-excitation (AD) transition where after the resonant neutralisation as described above the available energy $W_i^* - \phi_w$ is transferred to a more loosely bound electron of the ion. The kinetic energy of the emitted electron amounts to

$$E \leq W_{ex}^* - 2\phi_W$$

where W_{ex}^* is the excitation energy (see figure 3.2c). W_{ex}^* is assumed to be independent of the distance d_p between the projectile ion and the surface of the solid, since all involved electronic states suffer similar level shifts, resulting in approximately constant differences between the states.

The last two-electron transition described here is the auto ionisation (AI) process (see figure 3.2d), where the initially double or multiple excited projectile suffers an auto ionisation process by emitting one or more electrons in combination with de-excitation of excited electrons. This process plays an important role for neutralisation of multiple charge ions (MCI), which follows multiple resonance transitions into high quantum number excited states [21, 61].

It is also possible that an excited projectile can emit a photon to reach a lower energy state. This transition is called the radiative de-excitation (RD). The probability for such a transition is very low, since the time scale of a radiative process is of the order of 10^{-8} s, which is much larger than for Auger transitions. For highly charge ions (HCI) this transition becomes relevant, since the transition rate increases with the charge state of the projectile ion [5].

The total yield including potential emission

Based on the theory of Hagstrum [40] the following formula for the total yield due to PE was derived [58]

$$\gamma_{PE} \approx \frac{0.2}{E_F} (0.8V_q - 2\phi_W) \quad (3.7)$$

Here, E_F is the Fermi energy, V_q the potential energy of the projectile, and ϕ_W the work function. Equation 3.7 yields an upper limit for the total yield due to PE only reached

in the case of very low impact energies. In ref. [62] the energy dependence of the total yield including KE is derived as

$$\gamma = \frac{\alpha_1}{\sqrt{v}} + \gamma_{PE,\infty} + \alpha_2(v - v_{th})\Theta(v - v_{th}) \quad (3.8)$$

where the influence of the velocity of the incident particle on the time of interaction is taken into consideration. The total yield γ decreases with the particle's velocity according to the term α_1/\sqrt{v} until the equilibrium value $\gamma_{PE,\infty}$ is reached. The KE is assumed to be 0 below the threshold and to be proportional to the velocity with the factor α_2 above. The function $\Theta(x)$ is the well-known Heaviside function.

3.1.3. Energy distribution of the emitted electrons

The number of emitted electrons in an energy interval $[E, E + dE]$ are described by the energy distribution $N(E)$. The shape of this distribution is quite similar for all ion-induced electron emission experiments. $N(E)$ rises to a maximum δ_m at an energy E_m of several eV from zero at 0 eV and decreases for higher kinetic energies [42].

The energy distribution $N(E)$ of electron-induced secondary electron emission is described empirically by Lin and Joy [53] where an universal law is proposed:

$$\delta(E) = 1.28 \times \delta_m \left(\frac{E}{E_m} \right)^{-0.67} \left\{ 1 - \exp \left[-1.614 \left(\frac{E}{E_m} \right)^{1.67} \right] \right\} \quad (3.9)$$

(compare eq. 2.2 in section 2.1). E_m and δ_m are material dependent parameters.

For ion-induced electron emission such a simple approach is not appropriate due to the complicated KE and PE processes. Still, the description of the energy spectrum of the emitted electrons with a small number of parameters is practical and is good enough for a rough estimate.

Due to the diverse nature of the PE and KE process, it is justified to look into the influences of these processes on the energy distribution of the emitted electrons separately. For PE the Auger-Neutralisation process is the dominant one especially for singly charged ions. In a first order approximation the energy distribution is not dependent on the particle's energy. Still, there are energy dependent effects which lead to broadening and shifts of the energy distribution. This is described in more detail in reference [40].

For KE the energy distribution $N(E)$ can be described according to eq. 3.9. Here, the energetic maximum E_m is determined by the energy where the stopping power reaches its maximum [89].

3.1.4. Influence of surface contamination

For measurements of the electron emission yield from surfaces it is of great importance that the surface is very clean. Already contamination of well below one monolayer coverage can influence the yield quite drastically as shown in [41]. The adsorbed particles influence the surface work function and this is the reason for the change in the electron yield. Also the shape and position of the energy distribution is strongly correlated to the surface contamination.

It is well known, that adsorbed Oxygen on one hand increases the surface work function and on the other hand decreases the surface density-of-states (S-DOS) at the Fermi level. In addition several resonant states at about 5 eV below the Fermi edge are created. This leads to a decrease in the electron yield due potential emission, while the KE electron yield increases rapidly for higher impact energies. Alkali metals (e.g. Cs as used in experiments described later) in turn strongly decrease the surface work function, which increases the probability for resonant transitions and the AN and AD processes [42].

3.2. General considerations about electron coincidence experiments with ion pulses

In coincidence experiments it is very important to have good knowledge about the statistics of the experiment. It is important to know under which conditions the ratio of true to accidental coincidences reaches a maximum. In contrast to non-coincidence experiments it is generally not true that with increasing incident flux the useful countrate improves. As explained earlier (see section 1.1.5), for APECS the increase of the incident flux leads to a proportional increase of the true coincidences, while the false coincidences are proportional to the square of the flux. Therefore, the incident flux is limited to obtain an acceptable ration of true to false coincidences.

In the next section considerations about the calculation of true and accidental coincidence count rates for the MoVES analyzer used with ions as primary particles are described. Coincidences of electrons which are emitted due to the same ion-solid interaction are considered.

3.2.1. Ion pulse generation

By repeatedly deflecting an ion beam over a slit ion pulses can be generated. The average number of ions λ of one pulse depends on the length of the pulse in time Δt and the flux I of the ion beam:

$$\lambda = \frac{I\Delta t}{e}$$

where $e = 1.602176487 \cdot 10^{-19}C$ is the elementary charge if we assume that we have singly charged ions. The Poisson distribution determines the probability that the pulse contains n ions:

$$P(n; \lambda) = \lambda^n \frac{e^{-\lambda}}{n!}$$

Since it is generally not possible to distinguish electrons which were emitted from two or more ion–solid interactions at the same time, it is desirable to increase the ratio of pulses with one ion to pulses with two or more ions. This is only possible by decreasing the average ion number in a pulse. E.g. for an average ion number of $\lambda = 0.1$ 95% of the ion pulses which actually contain ions contain one ion while 5% contain two or more ions. But for $\lambda = 0.1$ also 90% of the times where the ion beam is deflected over the slit actually no ion at all enters the spectrometer chamber. This drastically reduces the rate of ion–solid interactions. The only way to increase the rate is by increasing the frequency with which the ion beam is chopped.

The ions have to pass a grid with a transparency of $g = 0.92$ on their way to the sample. It is therefore possible that even if two or more ions enter the slit only one ion hits the sample if the other ions are caught in the grid. Summarizing all these considerations the overall rate ν_k^i with which k ions hit the sample per second amounts to

$$\nu_k^i = f \sum_{n=k}^{\infty} P(n; \lambda) g^k (1-g)^{n-k} \binom{n}{k}$$

where f is the frequency.

3.2.2. True and false coincidences

The main interest in such experiments is to measure true coincidences, i.e. measuring two or more emitted electrons which were created during the interaction of one single ion with the solid. As explained above, it is not possible to prevent that a pulse consist of two or more ions. Therefore, there will be also false coincidences, i.e. electrons are measured in coincidence but they actually originate from different ion–solid interactions. Several parameters of the experiment have to be controlled in such a way, that the ratio of true to false coincidences is maximized. In this section we derive the probability that two electrons are detected in a real coincidence if one or more ions hit the sample.

Let $Q(n; \gamma)$ be the probability that n electrons are emitted during an ion–solid interaction, where γ is the average number of electrons emitted during such an interaction or total electron yield. $Q(n; \gamma)$ could be again the Poisson distribution, but the true distribution is not known.

We first consider the case of true coincidence of two electrons. If one ion hits the sample, the probability that two electrons are emitted and detected amounts to

$$\alpha_{12}^t = Q(2; \gamma)T^2$$

where T is the probability that the electrons pass the two grids (transparency g) on their way towards the MCP and are detected by the MCP/DLA detector with a probability d :

$$T = g^2 d$$

If two ions hit the sample exactly two electrons need to be emitted during one ion-solid interaction, while all possible electrons which originate from the other ion-solid interaction need to end up in the grids or are not detected.

$$\alpha_{22}^t = 2Q(2; \gamma)T^2 \sum_{n=0}^{\infty} Q(n; \gamma)(1 - T)^n$$

The factor 2 in the formula above is due the fact that either ion can produce a true coincidence. It is now straightforward to deduce the probability α_{kl}^t for true l electron coincidences if k ions hit the sample

$$\alpha_{kl}^t = kQ(l; \gamma)T^l \sum_{n_{k-1}=0}^{\infty} \cdots \sum_{n_1=0}^{\infty} Q(n_{k-1}; \gamma) \cdots Q(n_1; \gamma)(1 - T)^{n_1 + \cdots + n_{k-1}} \quad (k \ 1)$$

In order to obtain the overall rate of true l electron coincidences the rates for pulses which contain k ions need to be multiplied by the corresponding probability α_{kl}^t

$$\nu_l^t = \sum_{k=1}^{\infty} \nu_k^i \alpha_{kl}^t$$

It is not straightforward to obtain the rate of false coincidences for this case. But the rate of all coincidences (true and false) can be derived in analogy to the above. We first consider the case of one ion-solid interaction.

$$\alpha_{12}^a = \sum_{n=2}^{\infty} Q(n; \gamma)T^2(1 - T)^{n-2} \binom{n}{2}$$

One ion can also produce three or more electrons. If only two of these electrons are detected this also contributes to the two electron coincidences. Since 2 out of n electrons are detected all contributions have to be multiplied by $\binom{n}{2}$ as follows from combinatorics. In the case that two ions hit the sample, the possibility that two electrons are detected is

$$\alpha_{22}^a = \sum_{n_2+n_1 \geq 2}^{\infty} Q(n_2; \gamma)Q(n_1; \gamma)T^2(1 - T)^{n_2+n_1-2} \binom{n_2 + n_1}{2}$$

Here we sum over any possible combination of n_1 and n_2 where $n_2 + n_1 \geq 2$ which corresponds to a reordering of the summands.

We can now write down a general formula for the probability that for k ions l electrons are detected regardless of their origin

$$\alpha_{kl}^a = \sum_{n_1+\dots+n_k \geq l}^{\infty} Q(n_1; \gamma) \dots Q(n_k; \gamma) T^l (1-T)^{n_1+\dots+n_k-l} \binom{n_1+\dots+n_k}{l}$$

The rate of all l electron coincidences is then given by

$$\nu_l^a = \sum_{k=1}^{\infty} \nu_k^i \alpha_{kl}^a$$

The rate of false coincidences can then easily be calculated to

$$\nu_l^f = \nu_l^a - \nu_l^t$$

The ratio R_c of true to false coincidences amounts to

$$R_c = \frac{\nu_l^t}{\nu_l^f} = \frac{\nu_l^t}{\nu_l^a - \nu_l^t}$$

Since the ratio itself does not depend on the frequency f it is possible to directly increase the rate of true coincidences by increasing the frequency without change in the statistics of true to false coincidences.

The coincidence rate for APECS is determined by the incidence flux at which the ratio of true to false coincidences is about 1 (see section 1.1.5). Since the rate of true coincidences is proportional to the incidence flux while the rate of false coincidences is proportional to the square of the flux, there is a hard limit for the coincidence rate. For pulsed ion-induced electron emission coincidence experiments the coincidence rate is determined by the chop frequency and the average number of ions per pulse. The latter is chosen to obtain an acceptable true to false coincidences ratio, while the first quantity is only limited by the experimental setup.

3.3. Aspects and Design of the Momentum Vector Electron Spectrometer

Coincidence spectroscopy is a well known technique but experiments can take a very long time due to the low coincidence rate. This major drawback is responsible for the lack of interest in this technique. A novel magnetic-field time-of-flight electron spectrometer was developed as part of the present thesis work, that features a much higher coincidence rate. The new spectrometer called “Momentum Vector Electron Spectrometer (MoVES)” utilizes a magnetic field to project the half sphere above the surface of the sample onto a detector which is able to resolve the impact position of the electron. From the timing and position information of this detector the kinetics of the emitted electrons at the time of emission are determined. Multi-hit capability of the detector allows to measure up to 14 electrons in coincidence.

The spectrometer is mounted in an ultra high vacuum (UHV) chamber and since both the electric and magnetic field are axial, ions, electrons and photons can be used as incident radiation. A sketch of the spectrometer is shown in figure 3.3. The UHV conditions allow to conduct surface physics experiments.

3.3.1. Principle of Operation

The basic components of the analyzer comprise

- a microchannel plate (MCP) with a delay line anode which allows position dependent measurement of electrons
- electrodes which produce an electric field along the analyzer axis
- Helmholtz coils which generate an axial magnetic field
- a sample where electrons due to incident radiation are emitted and which is part of the last electrode

Figure 3.3 shows a sketch of the relevant parts. A pulsed beam of ions, electrons or photons with a short pulse length (~ 1 ns) enters the analyzer through a hole in the Micro-channel plate (MCP). The beam advances along the axis of the analyzer and hits the sample. Electrons are excited and emitted from the surface of the sample. Due to the magnetic field the electrons are forced on a cyclotron trajectory and if the transversal energy does not exceed a certain limit depending on the strength of the magnetic field the electron will hit the MCP. The time of flight and the impact position are recorded and are used to calculate the electron momentum, i.e its full kinetic properties in terms of its energy and polar and azimuthal emission angle (E, ϑ, φ). An electric field is applied for acceleration, so that the time of flight of all electrons has an upper limit. The electric

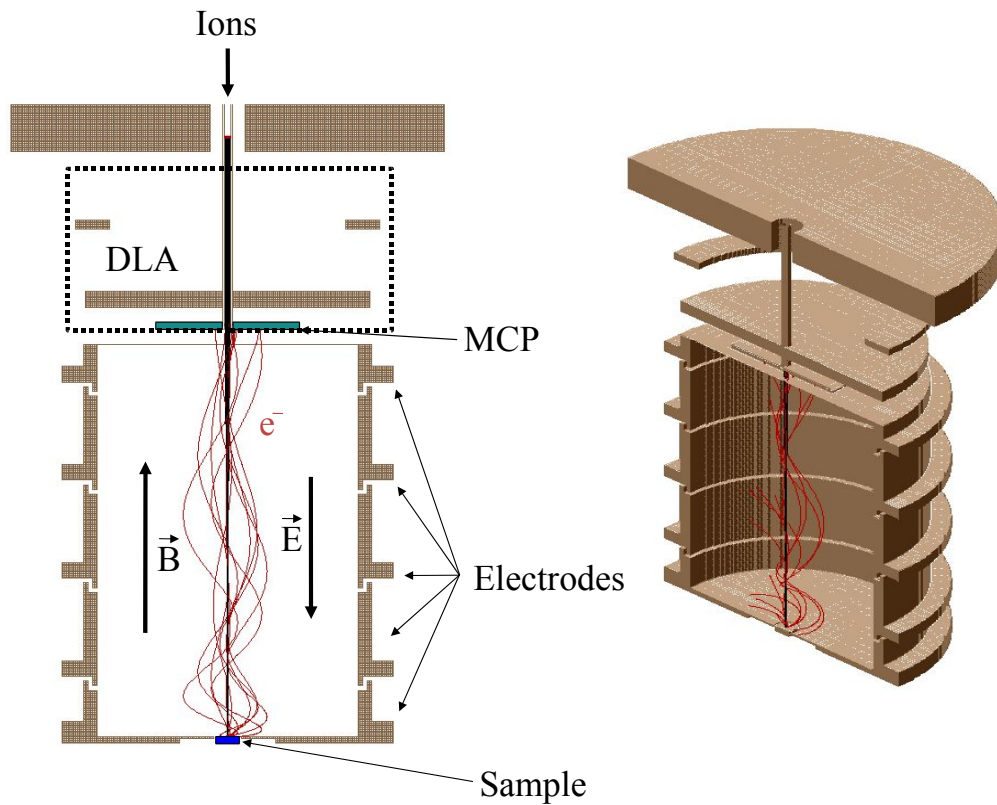


Figure 3.3: A schematic drawing of the novel momentum vector electron spectrometer (MoVES). Very short (~ 1 ns) ion pulses enter the spectrometer from the top and travel through the delay line anode shielded from high voltages by a tube. When the ions hit the sample, electrons are emitted which are forced on a cyclotron trajectory due to the magnetic field (produced by Helmholtz coils) while the electric field (generated by the electrodes) accelerates the electrons towards the MCP. Impact position on the MCP and the time of flight of the electrons are recorded. From these data the momentum of the electrons at the time of emission can be reconstructed.

field ensures that all electrons reach the MCP within a certain period of time and that electrons from consecutive pulses can be distinguished. Furthermore, due to the multi-hit capability of the delay line anode (DLA) it is possible to detect two or more electrons in coincidence.

In order to be able to understand certain aspects of this spectrometer, figure 3.4 shows the velocity dependence $v = \sqrt{2E/m}$ on the energy for electrons and Cs^+ ions. According to this figure the emitted electrons need some 100 ns from the sample to the MCP along the drift range of about 0.25 m. 5 keV Cs^+ ions need about 15 μs from the ion gun to the sample, which are about 1.3 m apart.

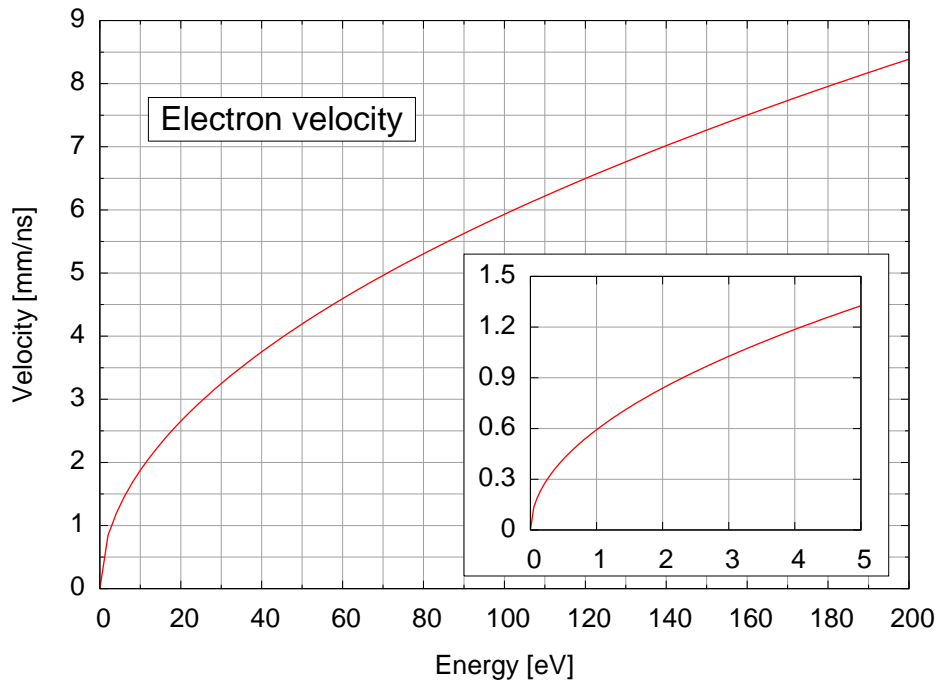
3.3.2. Specifications

In this section the specifications of various parts used of the MoVE-spectrometer and the UHV chamber are introduced. Some of these components are explained later in greater detail.

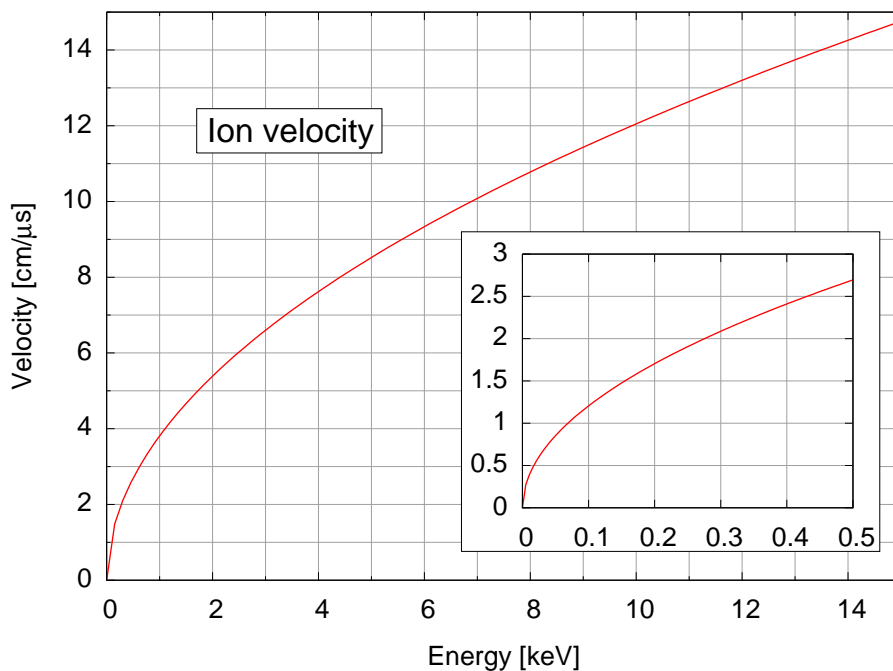
UHV chamber An UHV chamber was designed and built where the spectrometer is mounted and sample manipulation and preparation can take place. A Pfeiffer turbomolecular drag pump (TMU 521P) and a Balzers baffle with integrated Titanium sublimation pump (Type UPK 150/150A) pumps the chamber down to a pressure of about 4×10^{-11} mbar. Since the turbomolecular pump vacuum Pfeiffer has a magnetic bearing it can operate in a magnetic field of 5 mT maximum. An UHV Bayard-Alpert combination gauge of AML (AlG17G) measures the pressure. The whole chamber can be baked to a temperature of 150°. For the chamber only 316LN (magnetic permeability $\mu_r < 1.005$) and 304 ($\mu_r < 1.1$) stainless austenitic steel was used to minimize the influence on the produced magnetic field.

Detector For electron detection a hexanode position- and timesensitive multi-hit MCP delay-line detector system from RoentDek Handels GmbH is used. The MCP and the delay line anode have a 7 mm hole, through which the incident radiation enters the spectrometer. The MCP has an active diameter of 83 mm and a position resolution of 0.15 mm. The DLA has three layers of anode wires from which redundant information about the electron impacts is gained for multihit capability. The signals of the anode and the MCP are amplified and processed by constant fraction timing circuits (CFT).

Time-to-digital converter After the CFT circuits processed the anode and MCP signals the time in relation to the time of ion-solid interaction needs to be determined. This task is fulfilled by a very precise time-to-digital converter (TDC) from GP TA. The TDC has a time resolution of ~ 60 ps and with the help of a time stamp generator a virtually unlimited acquisition time.



(a) Electron velocity for an energy range of up to 200 eV



(b) Cs⁺ ion velocity for an energy range of up to 15 keV

Figure 3.4: In order to understand certain aspects of the spectrometer and to be able to estimate how much time particles need for a certain distance, the velocity of electrons and Cs⁺ ions over an energy range is plotted. Note that different ranges of both velocity and energy are shown in the plots. The insets in the plots show the velocity dependence for the lower energy region respectively.

Electric field The axial electric field in the spectrometer is created by 5 cylindrical electrodes. All electrodes can be adjusted to any arbitrary voltage up to 1 kV. The length of the drift range covered by the electrodes is 0.252 m, therefore a maximal electric field of ~ 4000 V/m can be applied.

Magnetic field The axial magnetic field is established by two parallel coils arranged in Helmholtz configuration. The mean radius of the coils is 1.09 m so that the accuracy of the field in the drift range is below 0.1%. The coils are not cooled, hence, the current is limited to about 30 A which corresponds to a magnetic field of ~ 2 mT. In addition two square coils in Helmholtz configuration together with a magnetic field compensation system [28, 27] are available to compensate the earth magnetic field and noise perpendicular to the axis of the spectrometer.

Sputter gun For sample cleaning purposes a sputter gun from PHI (Model 04-191) is installed. The chamber is backfilled to 5×10^{-5} mbar of Argon to provide the sputter ions during the sputter process.

Auger spectrometer In order to determine the surface cleanliness a compact Auger electron spectrometer with a cylindrical mirror analyzer from Perkin Elmer (Model 10-155) is mounted near the sample. The μ -metal shield of the spectrometer was removed since it would have distorted the magnetic field in the chamber. Hence, the operation of the spectrometer demands also the use of the magnetic field compensation system.

Sample manipulator The sample is positioned with a Varian high precision manipulator (Model 981-2523). The rotary motion mechanism has a position resolution of 0.1° , while two (X and Y) of the three orthogonal manipulator motions have a position resolution of 0.01 mm and Z 0.02 mm.

Faraday cup In order to measure the current of the full incident charged particle beam a Faraday Cup is mounted on the sample manipulator. In front of the cup a collimator with a 1mm hole is installed to determine the size and location of the beam at the sample position.

3.3.3. Creation of the axial magnetic field

The magnetic field in the axis of the spectrometer is responsible for the cyclotron trajectories of the electrons. Therefore, nearly all electrons emitted from the sample up to a certain energy end up on the MCP.

The magnetic field must be homogeneous to a very high degree in the range of the drift region, since the accuracy of the reconstructed momentum depends on the field. It was chosen to build coils which are mounted in Helmholtz configuration. In this section we present a simplified derivation of the magnetic field produced by coils in Helmholtz

configuration in order to estimate the size of the coils and the current needed to create a magnetic field up to 2 mT.

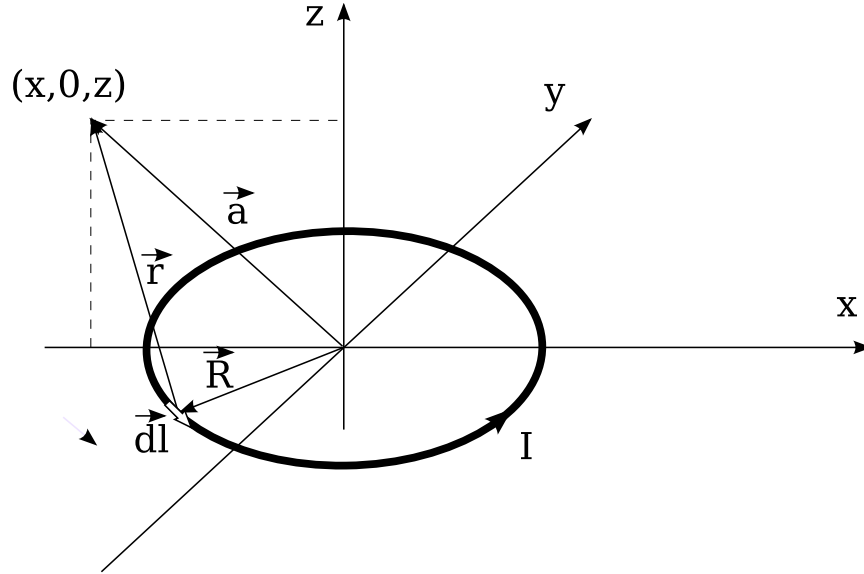


Figure 3.5: An infinitesimal part $d\mathbf{l}(\mathbf{R})$ of the loop with the current I and the radius R contributes $d\mathbf{B}$ at the position $\mathbf{a} = (x, 0, z)$ to the magnetic field according to the law of Biot-Savart (eq. 3.10). \mathbf{r} is the distance vector between $d\mathbf{l}$ and \mathbf{a} .

If there is a current I in a loop a magnetic field is generated at the position \mathbf{a} according to the law of Biot-Savart

$$d\mathbf{B}(\mathbf{a}) = \frac{\mu_0 I}{4\pi} \frac{d\mathbf{l} \times \mathbf{r}}{r^3} \quad (3.10)$$

where μ_0 is the permeability of vacuum, $d\mathbf{l}$ an infinitesimal small part of the loop and \mathbf{r} the position vector from $d\mathbf{l}$ to \mathbf{a} . Since this is a cylinder symmetric problem we set $y = 0$ and calculate the magnetic field at the position $\mathbf{a} = (x, 0, z)$.

For $d\mathbf{l}$ and \mathbf{r} we find (compare fig. 3.5)

$$d\mathbf{l} = \begin{pmatrix} dx \\ dy \\ 0 \end{pmatrix} = R d\varphi \begin{pmatrix} -\sin \varphi \\ \cos \varphi \\ 0 \end{pmatrix} \quad (3.11)$$

$$\mathbf{r} = \mathbf{a} - \mathbf{R} = \begin{pmatrix} x - R \cos \varphi \\ -R \sin \varphi \\ z \end{pmatrix} \quad (3.12)$$

where

$$\mathbf{R} = R \begin{pmatrix} \cos \varphi \\ \sin \varphi \\ 0 \end{pmatrix} \quad \mathbf{a} = \begin{pmatrix} x \\ 0 \\ z \end{pmatrix}$$

Here, R is the radius of the loop and \mathbf{R} determines the position of $d\mathbf{l}$.

If equations 3.11 and 3.12 are inserted in 3.10 we obtain

$$d\mathbf{B}(\mathbf{a}) = \frac{\mu_0 I}{4\pi} \frac{R}{(x^2 + z^2 + R^2 - 2xR \cos \varphi)^{3/2}} \begin{pmatrix} z \cos \varphi \\ z \sin \varphi \\ R - x \cos \varphi \end{pmatrix} d\varphi$$

If we integrate over φ from 0 to 2π we get

$$B_r(\mathbf{a}) = B_x(\mathbf{a}) = \frac{\mu_0 I}{4\pi} R \int_0^{2\pi} \frac{z \cos \varphi}{(x^2 + z^2 + R^2 - 2xR \cos \varphi)^{3/2}}$$

$$B_z(\mathbf{a}) = \frac{\mu_0 I}{4\pi} R \int_0^{2\pi} \frac{R - \cos \varphi}{(x^2 + z^2 + R^2 - 2xR \cos \varphi)^{3/2}}$$

Further calculations will reveal that the integrals are of elliptic type. Since solving elliptic integrals will not simplify further calculations a program was written to solve these integrals numerically using the GNU Scientific Library (GSL) [31].

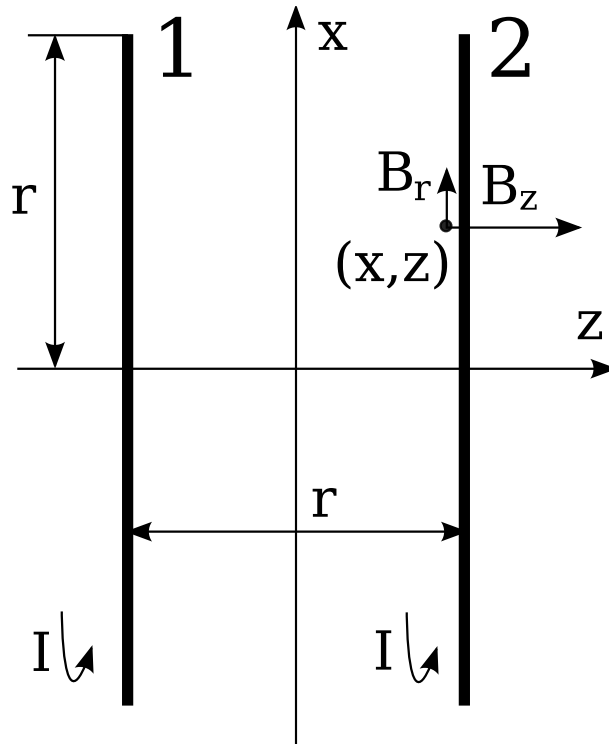


Figure 3.6: Two coils in Helmholtz configuration. The distance between the coils is equal to the radius r of a coil. If the same current I flows in both coils in the same direction a homogeneous magnetic field will be produced in between.

The magnetic field B_H of two coils in Helmholtz configuration (see figure 3.6) can be calculated if the field of both coils are superpositioned

$$B_{H,r}(x, z) = B_{1,r}(x, z + r) + B_{2,r}(x, z - r)$$

$$B_{H,z}(x, z) = B_{1,z}(x, z + r) + B_{2,z}(x, z - r)$$

It is possible to derive the magnetic field on the z -axis for coils in Helmholtz configuration (see e.g. [22]) analytically

$$B_{H,z}(0, z) = \frac{\mu_0 I}{(5/4)^{3/2} R} \left[1 - \frac{144 z^4}{125 R^4} \right]$$

and therefore the magnetic field exactly between the coils is

$$B_{H,z}(0, 0) = \frac{\mu_0 I}{(5/4)^{3/2} R}$$

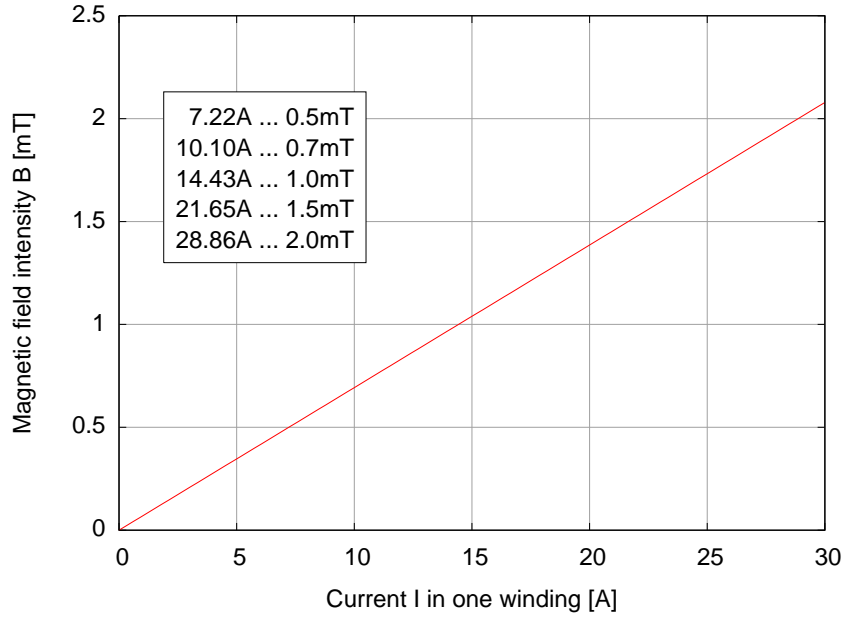
For the MoVE spectrometer it is required that the magnetic field intensity should be as much as 2 mT and that the inhomogeneity of the field in the drift region is below 0.1%. Based on the considerations above it was decided to design coils with a radius of 1.09 m and 84 windings of copper cable (rectangular shape 5 mm \times 2 mm) each. Figure 3.7a shows the dependence of the magnetic field of the current I for coils (84 windings) in Helmholtz configuration. In figure 3.7b the intensity of the magnetic field of coils in Helmholtz configuration depending on the position in space is shown. It is seen that the homogeneity in the drift region (central 25 cm of the figure) is better than 0.1%.

3.3.4. Compensation of the earth magnetic field and noise

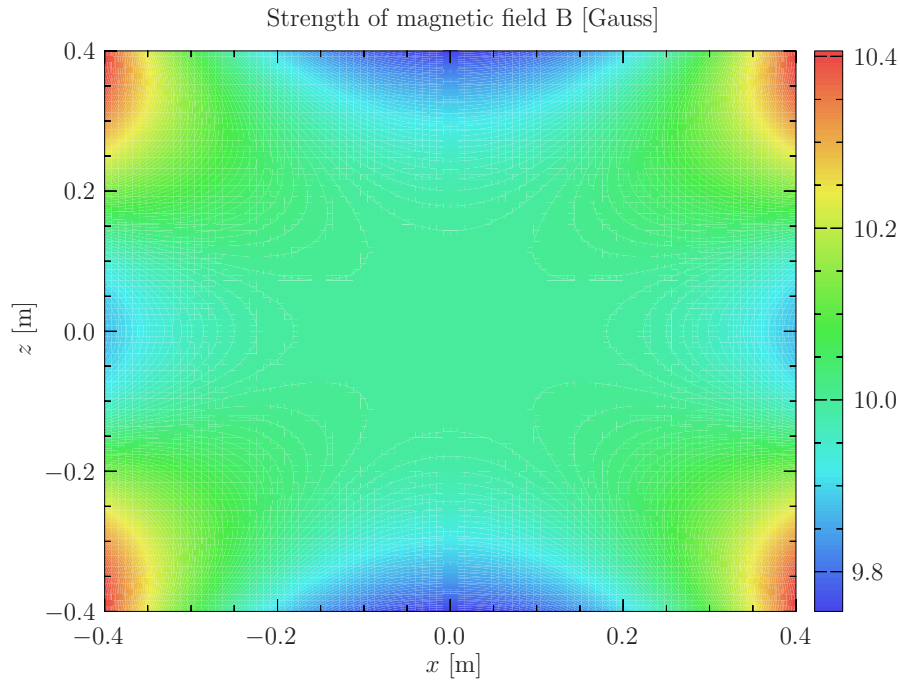
The earth magnetic field and magnetic noise needs to be compensated to obtain the energy and angular resolution with this analyzer. In Vienna (48.2167 North latitude and 16.3667 East longitude) the magnetic field of the earth has an total intensity of 48387 nT. The field has a declination of 2.972° and an inclination of 64.483°. The component in direction of the analyzer axis can be easily compensated by adjusting the current of the Helmholtz coils. Nevertheless, the components perpendicular to the axis have a major impact on the measurement.

For example, if the magnetic field produced by the Helmholtz is of the order of 1 mT, the earth magnetic field causes an electron drift of about 10 mm perpendicular to the analyzer axis for a drift range of about 0.260 m. Electromagnetic noise is typically in the order of a tenth of the earth magnetic field. Such fields will lead to drifts of the electrons of about 1 mm. Since the lateral resolution of the MCP is 0.15 mm it is also necessary to reduce the noise to the order of about 500 nT.

For this experiment it was possible to reuse a system for compensation of the earth magnetic field and noise, which was built for an experiment by Eder *et al.* [28, 27] some years ago. Only two of the three square Helmholtz coils (side length $a = 1$ m) were used. The field component in direction of the magnetic field generated by the circular Helmholtz coils don't need to be compensated, since the noise ($\sim 5 \mu\text{T}$) is about 0.2–0.5% of the axial magnetic field which is in the order of the homogeneity of this field.



(a) Magnetic field dependence of I



(b) Magnetic field dependence of position

Figure 3.7: Two coils ($R = 1.09$ m) are mounted in Helmholtz configuration with 84 windings each. Figure (a) shows the dependence of the magnetic field intensity B between the coils of the current I . Figure (b) depicts the magnetic field intensity B in dependence of the position. The current through one coil was 14.43 A and therefore a field of 1 mT was produced in the drift region. The homogeneity of the magnetic field in the drift region (0.25 m \times 0.18 m) for this configuration is below 0.1%.

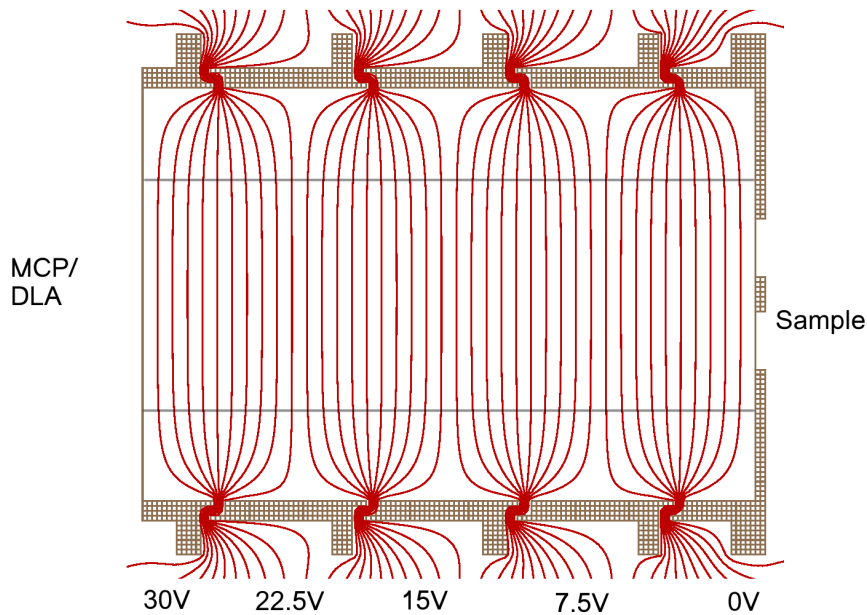


Figure 3.8: The electric field of the electrodes was calculated with SIMION 7.0 [20]. For the calculation an overall potential difference of 30 V was chosen. The potential difference between two adjacent electrodes is of the same order of magnitude to obtain a homogeneous electric field. The bounds of the drift region perpendicular to the spectrometer axis was determined by the size of the MCP (indicated by the solid horizontal lines).

To further improve the resolution of the spectrometer this noise component should also be compensated.

3.3.5. Creation of the axial electric field

In order to prevent that electrons with a very small axial velocity will mix with electrons from the next pulse, an electric field is applied in the drift zone. The electric field in the drift region is produced by five coaxial electrodes as shown in figure 3.8. All these electrodes can be set to an arbitrary potential. For the experiments between adjacent electrodes the same voltage difference is applied. The size of the electrodes were chosen in such a way that the electric field is homogeneous with the whole drift region. The size of the MCP determines the boundaries of the drift region perpendicular to the spectrometer axis as indicated by the horizontal solid lines in figure 3.8. The sample itself is part of the first electrode to achieve an even equipotential surface. The last electrode has a hole of the size of the MCP which is covered with a Molybdenum grid

(with a high transmission of 0.92).

After the last electrode there is another small drift range toward the MCP grid. The reason for this additional area is to prevent secondary electrons which are created when the emitted electrons hit the grid from reaching the MCP. To achieve this, the grid in front of the MCP is on a more negative potential than the grid at the electrode.

Note that the electric field also influences charged incident particles so that a change of the field also alters the energy of the particle and the time of the particle–solid interaction.

3.3.6. Electron trajectories in the spectrometer

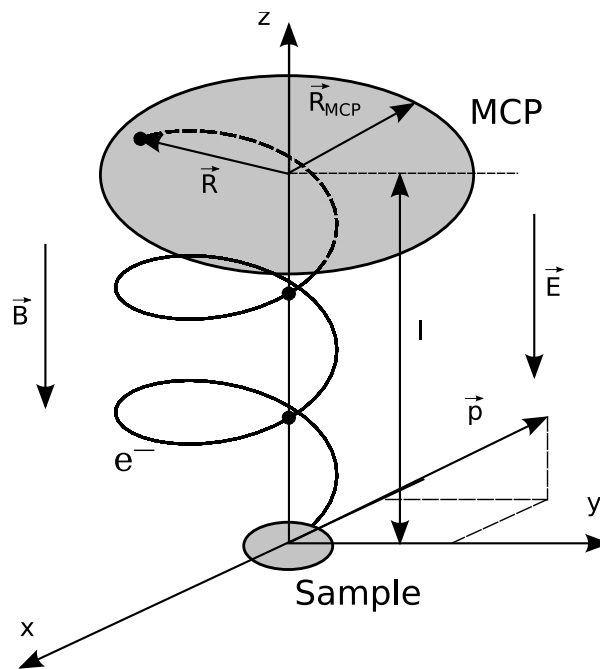


Figure 3.9: An electron with the initial momentum \mathbf{p} emitted from the sample is forced on a cyclotron trajectory if a magnetic field \mathbf{B} is applied in the drift region of the length l . The electric field \mathbf{E} accelerates the electron towards the MCP with the radius R_{MCP} . The impact position of the electron at the MCP is given by \mathbf{R} . If the time of flight t is a multiple of the cyclotron time t_c the electron passes the axis of the spectrometer shown with black dots at the directory.

The emitted electrons travel on a cyclotron trajectory towards the MCP. Figure 3.9 shows a sample trajectory of an electron. Since both the magnetic and the electric field are in the axis of the analyzer, the movement of the electron can be separated into two components: a longitudinal and a transversal part. The electric field influences only the longitudinal part of the movement. The magnetic field on the other hand has only an impact on the transversal motion.

An electron with charge $-e$ (e is the elementary charge) and the mass m_e experiences a force \mathbf{F} in a homogeneous electric field \mathbf{E}

$$\mathbf{F} = m_e \mathbf{a} = -e\mathbf{E}$$

Here, \mathbf{a} is the acceleration in direction of the force. Since the electric field has only a component in the spectrometer axis ($E = E_z$) we consider only the axial components. Integrating twice over the time t we obtain

$$v_z(t) = v_z(0) + \frac{eE}{m_e}t \quad (3.13)$$

and

$$z(t) = v_z(0)t + \frac{eE}{m_e} \frac{t^2}{2} \quad (3.14)$$

Here, v_z is the longitudinal velocity and z is the position at the z -axis, the sample is at the position $z = 0$. Equation 3.14 completely defines the axial motion of the electron in the spectrometer. It is straightforward to extend these equations for several consecutive electric fields.

In a homogeneous magnetic field of intensity B a charged particle will be forced on a periodic cyclic motion. The time needed for one period is the so-called cyclotron time

$$t_c = \frac{2\pi m_e}{eB} \quad (3.15)$$

and the radius of the trajectory is the so-called cyclotron radius

$$r_c = \frac{m_e v_{\perp}}{eB} \quad (3.16)$$

Without loss of generality we assume for the following considerations that $t < t_c$. Figure 3.10 shows the projection of the electron motion on the xy -plane. Since we have a cylinder symmetrical problem we also assume for the moment that $\varphi = 0$. Then the center \mathbf{m} and the radius $\mathbf{r}(t)$ of the circular trajectory are given by

$$\mathbf{m} = \begin{pmatrix} 0 \\ r_c \end{pmatrix} \quad \mathbf{r}(t) = r_c \begin{pmatrix} \sin \gamma(t) \\ -\cos \gamma(t) \end{pmatrix}$$

where $\gamma(t) = 2\pi t/t_c$. Hence, the current position $\mathbf{R}(t)$ of the electron is

$$\mathbf{R}(t) = \mathbf{m} + \mathbf{r}(t) = r_c \begin{pmatrix} \sin \gamma(t) \\ 1 - \cos \gamma(t) \end{pmatrix}$$

In order to discuss the case where $\varphi \neq 0$ we convert $\mathbf{R}(t)$ into polar coordinates. Note, that for the angles γ and δ the relationship $\gamma(t) = 2\delta(t)$ is valid (see figure 3.10).

$$\mathbf{R}(t) = \begin{pmatrix} 2r_c \sin \gamma(t)/2 \\ \delta(t) \end{pmatrix}$$

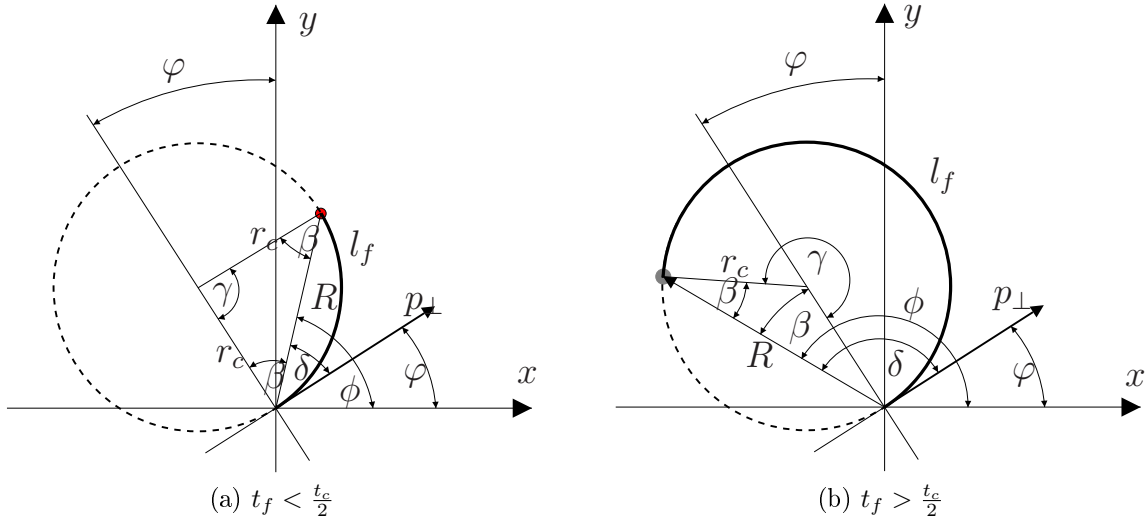


Figure 3.10: Both Figures show projections of the electron trajectory on a plane parallel to the MCP. The electron hits the MCP at the location \mathbf{R} . r_c denotes the cyclotron radius of the electron, \mathbf{p}_\perp the transversal momentum and l_f the trajectory length in the projected plane. The angles indicated are described in the text. Figure (a) shows the case where the flight time t_f is less than half the cyclotron time t_c , while figure (b) depicts the case where $t_f > \frac{t_c}{2}$.

Now we take into account φ and eventually get

$$\mathbf{R}(t) = \begin{pmatrix} 2r_c \sin \gamma(t)/2 \\ \delta(t) + \varphi \end{pmatrix} = 2r_c \sin \left(\frac{\pi t}{t_c} \right) \begin{pmatrix} \cos(\pi t/t_c + \varphi) \\ \sin(\pi t/t_c + \varphi) \end{pmatrix} = \begin{pmatrix} x(t) \\ y(t) \end{pmatrix} \quad (3.17)$$

It is important to understand that movement in the plane perpendicular to the spectrometer axis is only defined by the magnetic field and the initial momentum in this plane. Equation 3.17 and 3.14 together govern the motion of the electron in the spectrometer.

3.3.7. Determination of the electron momentum

If a homogeneous magnetic field \mathbf{B} is applied along the analyzer axis the emitted electrons travel on a cyclotron trajectory toward the Micro-channel plate (MCP). The position where the electrons hit the MCP and the flight time are recorded. From these three parameters (x, y, t_f) the energy E and direction (ϑ, φ) of the electron at the time of emission, i.e. the full kinetic information about the emission process can be calculated. We assume, that no electric field is applied in the drift region.

Figure 3.10 shows the electron trajectory projected on a plane parallel to the MCP. The position \mathbf{R} where the electron hits the MCP is marked with a circle. Since the cyclotron time t_c for electrons only depends on the magnetic field \mathbf{B} and therefore the trajectory

in the projected plane is periodic with t_c , it is only necessary to consider the case where the flight time t_f is smaller than the cyclotron time t_c .

First the cyclotron radius r_c and the azimuthal angle at the time of emission is determined. It is necessary to consider three cases: a) $t_f < t_c/2$, b) $t_c/2 < t_f < t_c$ and c) $t_f = t_c/2$. In all three cases the following relations are valid:

$$\gamma = 2\pi \frac{t_f}{t_c} \quad (3.18)$$

$$\beta = \arccos \frac{R}{2r_c}$$

In figure 3.10 all angles used above (γ, β) and in further derivation of relations (δ, ϕ, φ) are indicated.

Case (a). $\gamma < \pi$: From figure 3.10 we get the relationships

$$\frac{\gamma}{2} + \beta = \frac{\pi}{2} \quad (3.19)$$

$$\beta = \frac{\pi}{2} - \delta \quad (3.20)$$

Inserting eq. 3.20 in eq. 3.19 we obtain

$$\delta = \frac{\gamma}{2} \quad (3.21)$$

If equations 3.18 are inserted in 3.19 one gets

$$r_c = \frac{R}{2 \sin \frac{\pi t_f}{t_c}} \quad (3.22)$$

Considering figure 3.10 and using equation 3.18 and 3.21 we obtain

$$\varphi = \phi - \delta = \phi - \frac{\pi t_f}{t_c} \quad (3.23)$$

Case (b). $\pi < \gamma < 2\pi$: From figure 3.10 we get the relationships

$$\frac{2\pi - \gamma}{2} + \beta = \frac{\pi}{2} \quad (3.24)$$

$$\beta = \delta - \frac{\pi}{2} \quad (3.25)$$

which again leads to equation 3.21. One obtains equations 3.22 and 3.23 by combining equations 3.18 and 3.24

Case (c). $\gamma = \pi$: It is easy to confirm that in this case equations 3.22 and 3.23 are also true.

The transversal momentum p_{\perp} can be calculated from the cyclotron radius r_c and equation 3.22:

$$p_{\perp} = \frac{eBR}{2 \sin \frac{\pi t_f}{t_c}} \quad (3.26)$$

where e is the elementary charge.

If we assume that m_e is the electron mass and l is the length of the drift range the longitudinal momentum p_{\parallel} calculates to

$$p_{\parallel} = \frac{m_e l}{t_f} \quad (3.27)$$

Combining eq. 3.26 and 3.27 the energy of the electron is

$$E = \frac{1}{2m_e} \left[\left(\frac{m_e l}{t_f} \right)^2 + \left(\frac{eBR}{2 \sin \frac{\pi t_f}{t_c}} \right)^2 \right] \quad (3.28)$$

The polar angle ϑ at the time of emission calculates to

$$\vartheta = \arctan \frac{p_{\perp}}{p_{\parallel}} = \arctan \left(\frac{r \pi \frac{t_f}{t_c}}{l \sin \frac{\pi t_f}{t_c}} \right) \quad (3.29)$$

and the azimuthal angle φ was already determined in equation 3.23.

$$\varphi = \phi - \frac{\pi t_f}{t_c} \quad (3.30)$$

It was shown that from the impact position (x, y) and the flight time t_f , it is possible to determine the energy E and the direction (ϑ, φ) of the electron at the time of emission, if a homogeneous magnetic field is applied to the drift region but no electric field. In case of an additional axial electric field only the calculation of the longitudinal momentum (eq. 3.27) is directly influenced. All other derivations are still correct taking into account that the flight time of the electrons changes with the electric field. From eq. 3.13 we obtain (see figure 3.11a for the notation)

$$p_{\parallel}(0) = p_{\parallel}(t_f) - eEt_f \quad (3.31)$$

where $p_{\parallel}(0)$ is the longitudinal momentum of the electron at the time of emission and $p_{\parallel}(t_f)$ the momentum at the time of impact. In addition, we can determine the average longitudinal momentum

$$\overline{p_{\parallel}} = \frac{lm_e}{t_f} = \frac{p_{\parallel}(t_f) + p_{\parallel}(0)}{2} \quad (3.32)$$

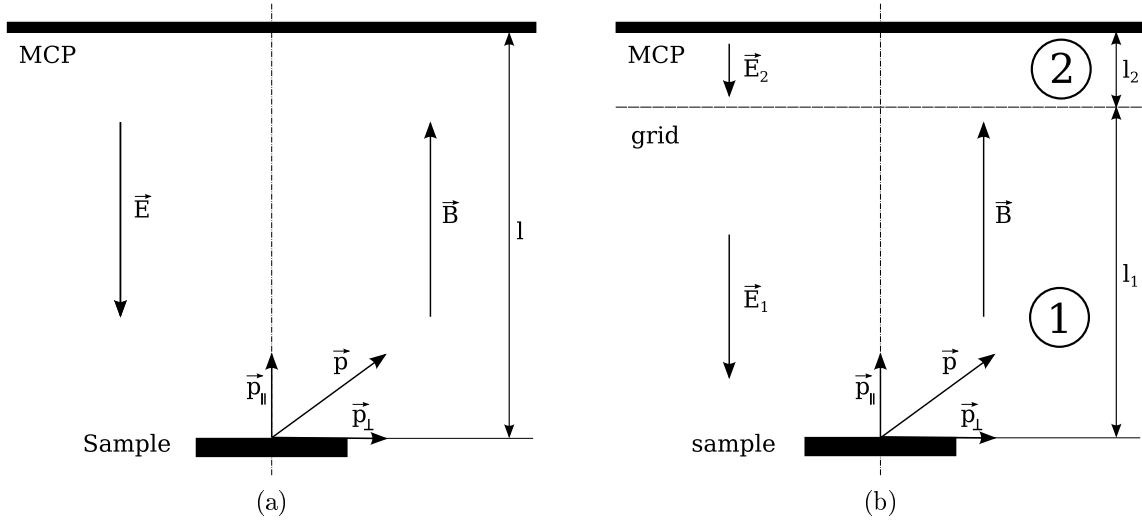


Figure 3.11: Notation if one (a) or two (b) electric fields are used for the spectrometer.

Since the acceleration due to the electric field is constant it is possible to relate the average momentum $\overline{p_{\parallel}}$ to $p_{\parallel}(0)$ and $p_{\parallel}(t_f)$. Inserting eq. 3.32 in 3.31 one obtains

$$p_{\parallel}(0) = \frac{lm_e}{t_f} - \frac{eEt_f}{2} \quad (3.33)$$

In case of one electric field present in the drift range the energy of the electron at the time of emission is therefore

$$E = \frac{1}{2m_e} \left[\left(\frac{m_e l}{t_f} - \frac{eEt_f}{2} \right)^2 + \left(\frac{eBR}{2 \sin \frac{\pi t_f}{t_c}} \right)^2 \right] \quad (3.34)$$

In order to prevent secondary electrons originating from the grid at the last electrode to reach the MCP a second short drift range is arranged after the spectrometer drift range. Here, two consecutive constant electric fields need to be taken into consideration to determine the momentum at the time of emission (see figure 3.11b). In further considerations,

$$t_f = t_1 + t_2$$

where t_1 and t_2 are the time of flight in the drift range 1 (of the length l_1) and 2 (of the length l_2) respectively,

$$l = l_1 + l_2 \quad (3.35)$$

and the average momenta in the respective drift range amount to

$$\overline{p_{\parallel,1}} = \frac{p_{\parallel}(t_1) + p_{\parallel}(0)}{2} \quad (3.36)$$

and

$$\overline{p_{\parallel,2}} = \frac{p_{\parallel}(t_2) + p_{\parallel}(t_1)}{2} \quad (3.37)$$

Inserting eq. 3.31 in eqs. 3.36 and 3.37 we can write

$$\overline{p_{\parallel,1}} = p_{\parallel}(0) + \frac{eE_1 t_1}{2} = \frac{l_1 m_e}{t_1} \quad (3.38)$$

and

$$\overline{p_{\parallel,2}} = p_{\parallel}(t_1) + \frac{eE_2 t_2}{2} = p_{\parallel}(0) + eE_1 t_1 + \frac{eE_2 t_2}{2} = \frac{l_2 m_e}{t_2} \quad (3.39)$$

If eqs. 3.38 and 3.39 are combined with eq. 3.35 we obtain

$$m_e l = t_1 \left(p_{\parallel}(0) + \frac{k_1}{2} t_1 \right) + t_2 \left(p_{\parallel}(0) + k_1 t_1 + \frac{k_2}{2} t_2 \right) \quad (3.40)$$

where

$$k_1 = eE_1, \quad k_2 = eE_2$$

Further simplifications of eq. 3.40 lead to

$$0 = l_1 t_f + t_1 \left(t_f^2 \frac{k_2}{2} - l m_e \right) + t_1^2 \left(\frac{k_1}{2} t_f - t_f k_2 \right) + t_1^3 \left(\frac{k_2}{2} - \frac{k_1}{2} \right) \quad (3.41)$$

With the help of the Cardano's formula we obtain a solution for t_1 . If there are 3 solutions of eq. 3.41 for t_1 all of them have to be checked for physical plausibility ($0 < t_1 < t_f, p_{\parallel}(0) > 0, p_{\parallel}(t_f) > 0$). Eq. 3.38 delivers then the longitudinal momentum at the time of emission.

3.3.8. Energy- and Angle Resolution

The energy resolution can be simply established when the relationship between the observables x, y and t_f and the parameters E, ϑ, φ describing the emission are known. This relationship was derived in section 3.3.7 above.

At its emission origin, the electron is therefore characterized by eqs. 3.28, 3.29 and 3.30. Applying the usual rules for uncorrelated propagation of the uncertainties in the flight time Δt and detection location ΔR to Equation 3.28, the energy resolution is found as:

$$\frac{\Delta E}{E} = 2 \left\{ \sin^2 \vartheta \left[\left(\frac{\Delta R}{R} \right)^2 + \left(\frac{\pi \Delta t / t_c}{\tan(\pi t_f / t_c)} \right)^2 \right] + \cos^2 \vartheta \left(\frac{\Delta t}{t_f} \right)^2 \right\}^{1/2} \quad (3.42)$$

The energy resolution as per Equation 3.42 is seen to consist of a transversal (1^{st} and 2^{nd} term) and a longitudinal component (3^{rd} term), as expected. The longitudinal component is governed by the flight time (or drift length) and the time resolution, while the transversal component is determined by the lateral resolution and an oscillatory term. The oscillatory term shows that if the flight time is a multiple of the cyclotron time, all emitted electrons will end up at the detector center and consequently all information

about the original momentum will be lost. This implies that all events with arrival times in a certain range $nt_c - \Delta t_c < t_f < nt_c + \Delta t_c$ must be discarded from the spectrum. The effective transmission of the analyzer is then smaller than unity and equal to $1 - 2\Delta t_c/t_c$.

If Δt_c is chosen appropriately, the longitudinal resolution is the leading term in the resolution which then can simply be estimated. For example, for a drift length of 1 m, the resolution at 1, 10, 100 and 1000 eV amounts to ~ 0.7 meV, 20 meV, 0.7 eV and 20 eV, respectively. If Δt_c is chosen in such a way that the oscillatory term can be neglected altogether, the remaining transversal and longitudinal terms depend only on the system dimensions and the lateral and time resolution. Since R is determined by the maximum detector size available, this allows to establish an optimum drift length. However, model calculations show that for energies of the order of 100 eV, the oscillatory term dominates the resolution up to values of $\alpha = \Delta t_c/t_c = 0.45$. Since the analyzer transmission becomes intolerably low for larger values of α , the energy resolution cannot be enhanced by making the drift length longer than a certain amount. This implies that the only effective way to improve the energy resolution is to increase *both* the detector radius and the drift length. For the present purpose, a drift length of ~ 25 cm turns out to be sufficient.

3.3.9. Transmission Function

The transmission function $T(E, \vartheta, \varphi)$ describes the probability that electrons with certain kinetic properties are detected by the analyzer. Since the MoVE spectrometer has a cylindrical symmetry, the transmission function does not depend on the azimuthal angle φ , therefore $T(E, \vartheta, \varphi) = T(E, \vartheta)$. In theory the MoVES analyzer could detect all electrons below a certain energy E depending on the magnetic field B . But by design there are some effects which in consequence decrease the possibility of detecting all electrons.

- The grids at the end of the electrode and in front of the MCP have a limited transparency. In addition, the direction of electrons when they pass the grids influences the transmission probability due to the finite thickness of the grids.
- The hole in the MCP and a “dead” area around this hole prevent the detection of electrons hitting the MCP in this area. In addition, the size of the MCP limits the transmission for higher energies and emission angles.
- The detector efficiency of a MCP for electrons is about 60%.
- The energy and angle resolution is dependent on the flight time modulo the cyclotron time. To improve the quality of the measurements only electrons satisfying a certain relationship between time of flight and cyclotron time are accepted which reduces the transmission function.

- The electron cloud emitted by the MCP must produce signals on the layers of the DLA, which in turn are then electronically processed and evaluated with a software on a computer. All these processes decrease the probability to detect the electron successfully.

It is now possible to write down the transmission function

$$T(E, \cos \vartheta) = g(\vartheta_1, \vartheta_2)md\tilde{T}(E, \vartheta, \mathbf{E}, \mathbf{B}, \alpha, A_{MCP}) \quad (3.43)$$

where $g(\vartheta_1, \vartheta_2)$ is the transmission of the grids used for the electrodes and in front of the MCP, m is the electron detection efficiency of the MCP and d is the probability that an electron which was amplified by the MCP will be eventually processed by all the electronics and software driving the DLA, CFT and time-to-digital-converter (TDC). $\tilde{T}(E, \vartheta, \mathbf{E}, \mathbf{B}, \alpha, A_{MCP})$ is the probability that the trajectory of an electron with a certain energy E and emission angle ϑ off normal will end on the active surface of the MCP (A_{MCP}), if an electric field \mathbf{E} and magnetic field \mathbf{B} are applied in the axis of the spectrometer. α is the threshold which defines which electrons are rejected because their kinetics can not be determined with sufficient accuracy.

In the following paragraphs we discuss the various contributions to the Transmission function.

Grid transparency

The grids used for the electrodes and the MCP have a transparency below 100%. For the MoVE spectrometer special ion-etched Molybdenum grids from HeatWave Labs (<http://www.cathode.com/>) were bought, which have a specified grid spacing of $l = 0.3556$ mm, grid thickness of $d = 0.01524$ mm and an estimated transparency of $g = 0.92$. The latter value is only valid if the electrons pass the the grid normal to the grid plane. In case the velocity vector of the electrons describe an angle ϑ with the grid normal, the

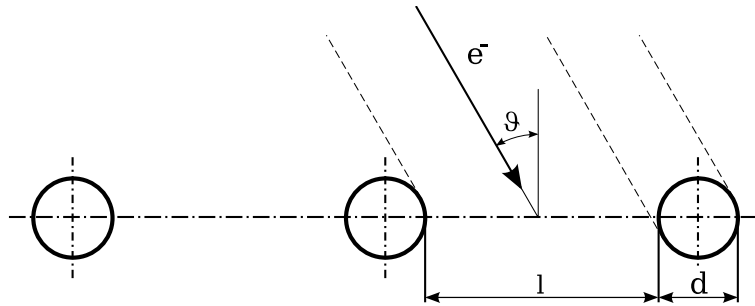


Figure 3.12: An electron passes the grid with an angle ϑ with respect to the grid normal. l is the grid spacing and d the thickness of the grid. The transmission of the grid decreases with ϑ .

transmission calculates to

$$g'(\vartheta) = \frac{((l+d)\cos\vartheta - d)l}{(l+d)^2}$$

(see figure 3.12 for details).

Since an electron has to pass two grids in the drift region, one at the last electrode and one in front of the MCP, the overall transmission due the grids is

$$g(\vartheta_1, \vartheta_2) = g'(\vartheta_1)g'(\vartheta_2)$$

where ϑ_1 and ϑ_2 are the angles under which the electron passes the grid at the last electrode and before the MCP respectively. The angles ϑ_1 and ϑ_2 depend themselves on the energy and direction of the electron at the time of emission and on the electric and magnetic field. Hence, it is possible to influence the grid transparency by the electric field which accelerates the electrons in the drift range. The higher the electric field the better is the grid transmission. Note, that the considerations above are only valid in first approximation, since there is also a dependency on the azimuthal angle φ . The grid has no cylindrical symmetry.

Influence of the shape of the MCP

The transmission of the electrons depends on the detection region of the MCP. This region is on one hand limited by the size of the MCP and on the other hand by the hole and the dead region around this hole in the middle of the MCP.

In order to examine the influence of the MCP on the transmission function we only need to examine the projection of the trajectories on the MCP, since the movement of the electron along and perpendicular the spectrometer axis are independent from each other. We assume for further considerations that the electric and magnetic field are fixed at a certain value.

Figure 3.13 shows the MCP (black circles) and three possible projected trajectories. In areas of the MCP where electrons can be detected the trajectories are green, red otherwise. Such a circle represents all trajectories of electrons with the same transversal momentum p_{\perp} or cyclotron radius but all possible longitudinal momenta p_{\parallel} . The time of flight of the electrons is only determined by p_{\parallel} . Therefore, if we increase p_{\parallel} while p_{\perp} stays the same, the impact position gradually moves clockwise along such a projected trajectory. This follows directly from eq. 3.17, which describes the movement of electrons in the x, y -plane perpendicular to the spectrometer axis. In consequence, electrons with a certain energy and emission direction will always be detected (green part of the trajectory) while other electrons with other kinetic properties will not (red part of the trajectory).

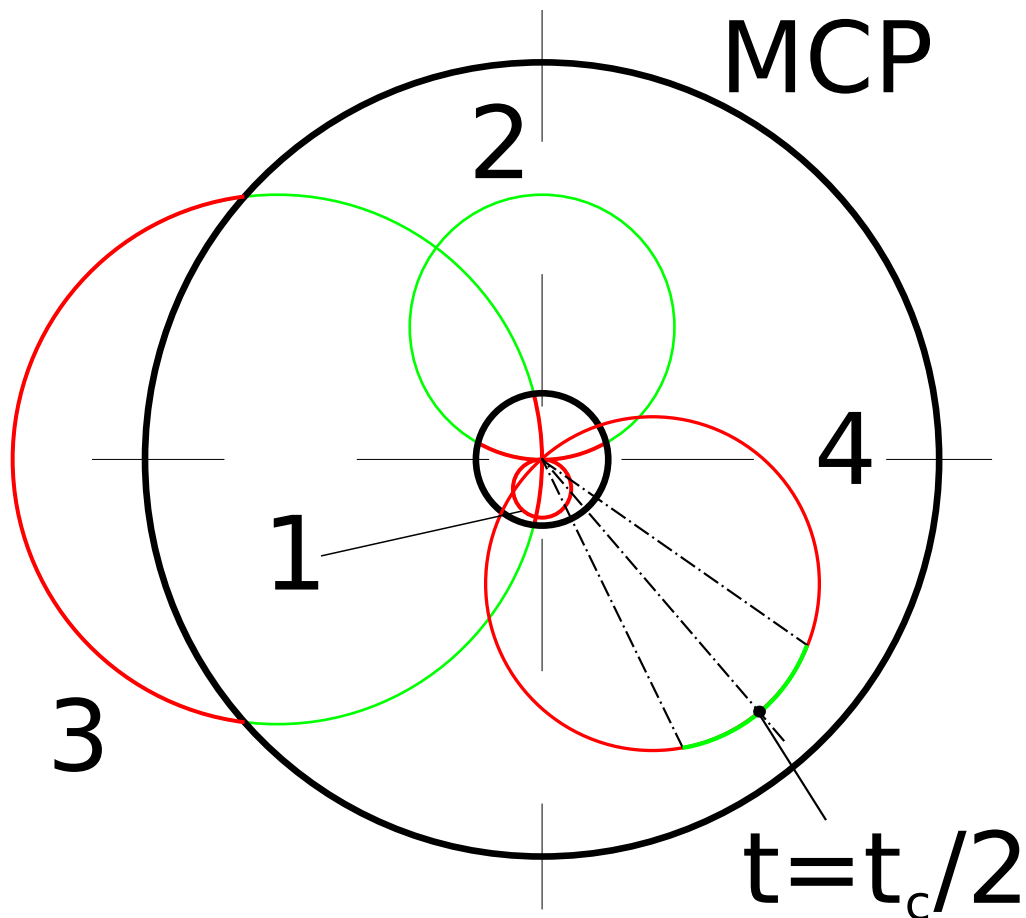


Figure 3.13: The shape of the MCP (black solid lines) has an influence on the transmission function. Projections of three possible kinds of electron trajectories are shown here. Such a trajectory represents electrons with the same cyclotron radius and all possible momenta p_{\parallel} along the spectrometer axis. Trajectory 1 is always outside of the MCP area, therefore there is no transmission. Electrons on trajectory 2 will most of the times hit the MCP, while some will end up in the hole of the MCP. This is determined by their energy and direction of emission. Electrons, which have sufficient momentum perpendicular to the spectrometer axis might miss the MCP (trajectory 3). For trajectory 4 only electrons are accepted which have about the maximum distance from the spectrometer axis. For these electrons a good energy resolution is obtained.

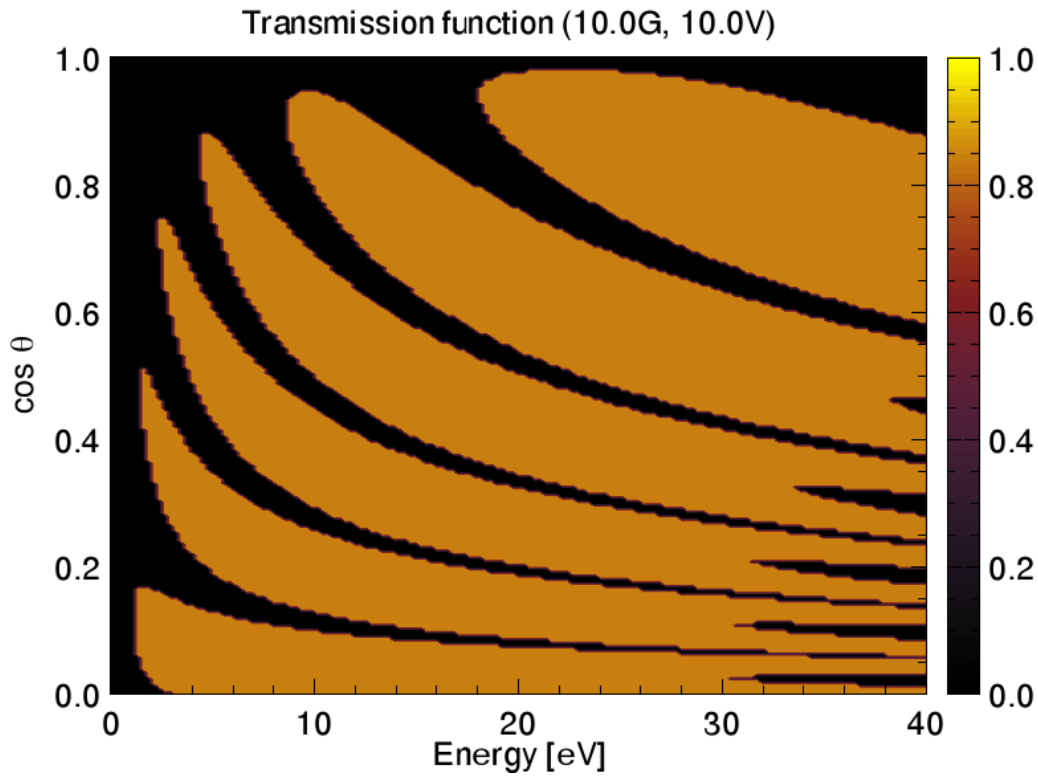


Figure 3.14: Transmission function $T(E, \vartheta)$ versus the cosine of the emission angle θ and the electron energy E . This particular transmission was calculated for an magnetic field of 1 mT and an electric field of 39.68 V/m. The size of the MCP ($R_{MCP} = 37$ mm, $R_{hole} = 7$ mm) and the length of the analyzer ($l = 0.262$ m) were taken into consideration. Since all electrons were accepted for this transmission function regardless their time of flight (compare 3.3.9) the structure of this transmission function is only based on the size of the MCP and its hole.

Figure 3.14 shows the transmission function depending on the energy and the emission angle for a certain analyzer configuration, taking the design of the MCP into consideration. “Bands” of maximum transmission can be seen which can be explained by the considerations above. The zero transmission area for low energies and for low emission angles is explained by the hole in the MCP (trajectory 1). There is no possibility that these electrons can be detected. For high electron energies the “bands” are split by zero transmission areas, which are due to the size of the MCP (trajectory 3). Here, electrons have enough energy to actually miss the MCP.

MCP detector efficiency

Not all incident source of radiation (photon, electron or ion) on a Micro-channel plate (MCP) lead to an amplified output electron pulse. The probability of this event is called detection efficiency of a MCP or Quantum Detection Efficiency (QDE). When incident radiation hits the surface of a channel, there is a probability that electrons will be ejected and further amplified. This probability is quite high (up to 60%) for charged particles like moderately energetic electrons or ions (0.3 – 3 keV), but also strongly dependent on the incident energy. For X-rays and ultra-violet radiation the QDE is in comparison quite low (between 5 – 10%). Here, the QDE is commonly increasing with the photon wavelength from 0.01 nm until a sharp drop at 120 nm. Various photon-cathode coatings applied to the input face of the MCP can increase the sensitivity to ultra-violet radiation.

The QDE of an MCP at normal operating conditions is limited by the open-area-ratio, i.e. the ratio of the area covered by channels to the overall MCP area. This ratio amounts for MCPs approximately to 60% and can practically never exceed 80%.

The angle of the channels with respect to the surface normal has great influence on the QDE. This angle is called the bias angle. Similar, the incident angle of the radiation to the channel will have comparable influence. A sharp drop of the QDE can be experienced if the bias angle is below 5° , due to increased reflectivity of the channel wall for grazing angles of radiation. For electrons the optimal bias angle is determined to 5° . For X-ray radiation the optimal bias angles are between 10° and 15° depending on the photon wavelength. For bias angles higher than 15° the higher penetration depth of the incoming radiation lowers the probability for the emission of secondary electrons and thus the QDE as well.

The value of the QDE is not correlated with the pore size. Generally smaller pore sizes lead to higher open-area-ratios which results in an increase of the practical limit of the QDE imposed by geometric constraints [115].

Improving the energy and angular resolution

The energy and angular resolution are dependent on the flight time of the electron t modulo the cyclotron time t_c as explained in section 3.3.8. We define $t_m := t \bmod t_c$. In order to achieve an acceptable resolution only these electrons are accepted for which the resolution is sufficient, i.e. where t modulo t_c is about half the value of t_c .

We introduce a quality parameter $\alpha \in [0, 0.5] \in \mathfrak{R}$ which is dependent on the energy resolution required. All electrons where t_m is between $t_1 = t_c \cdot \alpha$ and $t_2 = t_c \cdot (1 - \alpha)$ are accepted. For trajectory 4 in fig. 3.13 this constraint is applied. Electrons are only accepted if they hit the MCP in the green part of this trajectory. All other electrons are rejected due insufficient energy resolution obtained for them.

To obtain an acceptable resolution α must be between 0.35–0.45 if the spectrometer has a time resolution of 0.1 ns and a lateral resolution of 0.15 mm. The demand for acceptable energy resolution has a significant impact on the transmission of the spectrometer. The transmission “bands” as seen in fig. 3.14 become more narrow for high α and the overall transmission of the spectrometer decreases significantly.

Efficiency of the electronics and software

After the amplification of one electron by the MCP of about 10^7 the electron cloud is further accelerated towards the delay-line-anode (DLA). The cloud produces signals in the layers of the DLA. The signals are amplified and converted to NIM-signals by the constant-fraction-timing discriminator (CFT), which in turn are converted to timing information by the TDC. This timing information is processed by a software program (see section 3.4.1) which tries to sort the events and recreate the position where the electron impact on the MCP occurred. For all these steps there is a probability that signals are lost: signals of two different electron impacts close in time may overlap, signals may be attenuated by dissipation effects on the anode or arrive during the dead time of the electronics. Also the software might not be able to calculate lateral information from all the measured data.

The overall efficiency d of this system to detect an electron can be estimated as follows: the resort algorithm counts the number of times an electron is detected on only two of the three layers ($N_{e,2}$) and on all three layers ($N_{e,3}$) (compare table 3.1). We assume that \tilde{d} is the probability that an electron is detected on one layer and that \tilde{d} is the same for all layers. If for an actual measurement N electrons were amplified by the MCP we get

$$N_{e,2} = N\tilde{d}^2(1 - \tilde{d})\binom{3}{2} \quad (3.44)$$

and

$$N_{e,3} = N\tilde{d}^3 \quad (3.45)$$

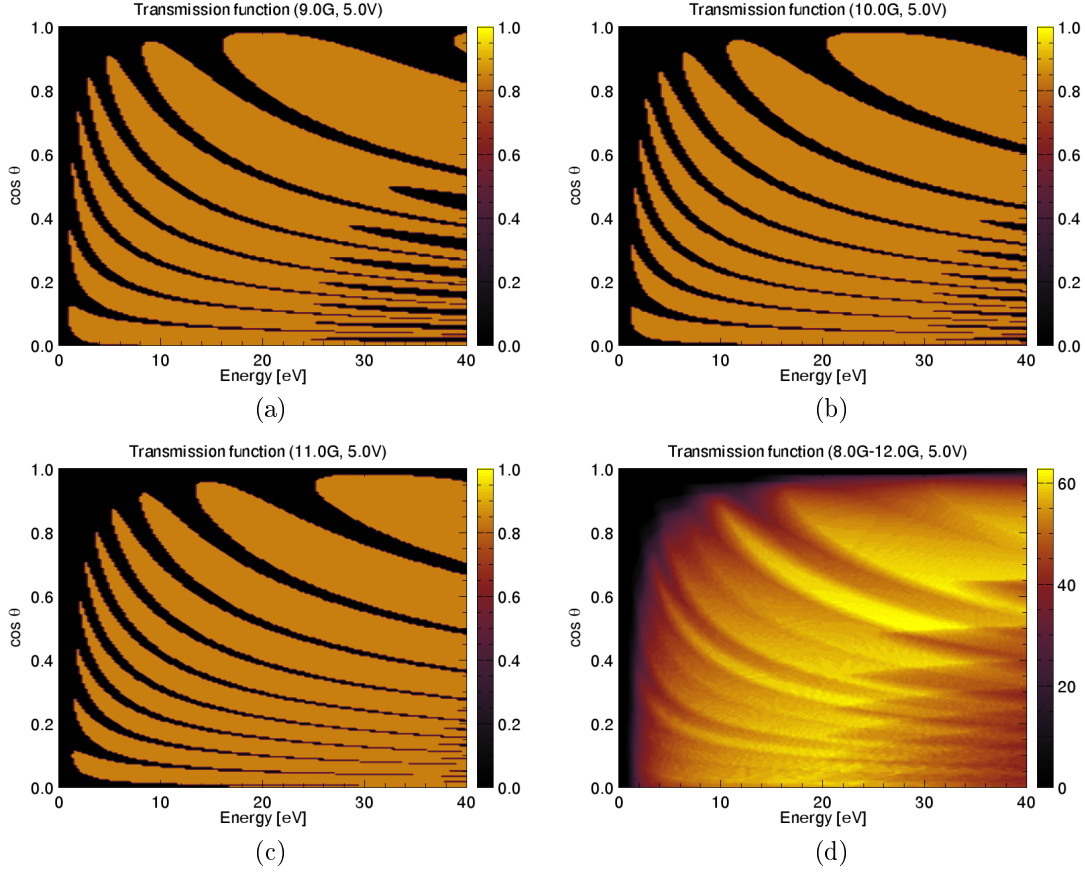


Figure 3.15: (a)-(c): Transmission function of the spectrometer for various magnetic fields from 9 to 11 G, while the electric field stays the same. (d): Cumulative transmission function if the magnetic field is changed periodically. θ is the polar emission angle.

If we insert equation 3.45 in 3.44 we obtain

$$\tilde{d} = \frac{3N_{e,3}}{N_{e,2} + 3N_{e,3}} \quad (3.46)$$

The efficiency d then calculates to

$$d = \binom{3}{2} \tilde{d}^2 (1 - \tilde{d}) + \tilde{d}^3 \quad (3.47)$$

Improving the transmission of MoVES

Considering all effects described in the paragraphs above the transmission of the MoVE spectrometer turns out to be a complicated function. Most of the effects can not be influenced since they are determined by the design of the spectrometer and by the phys-

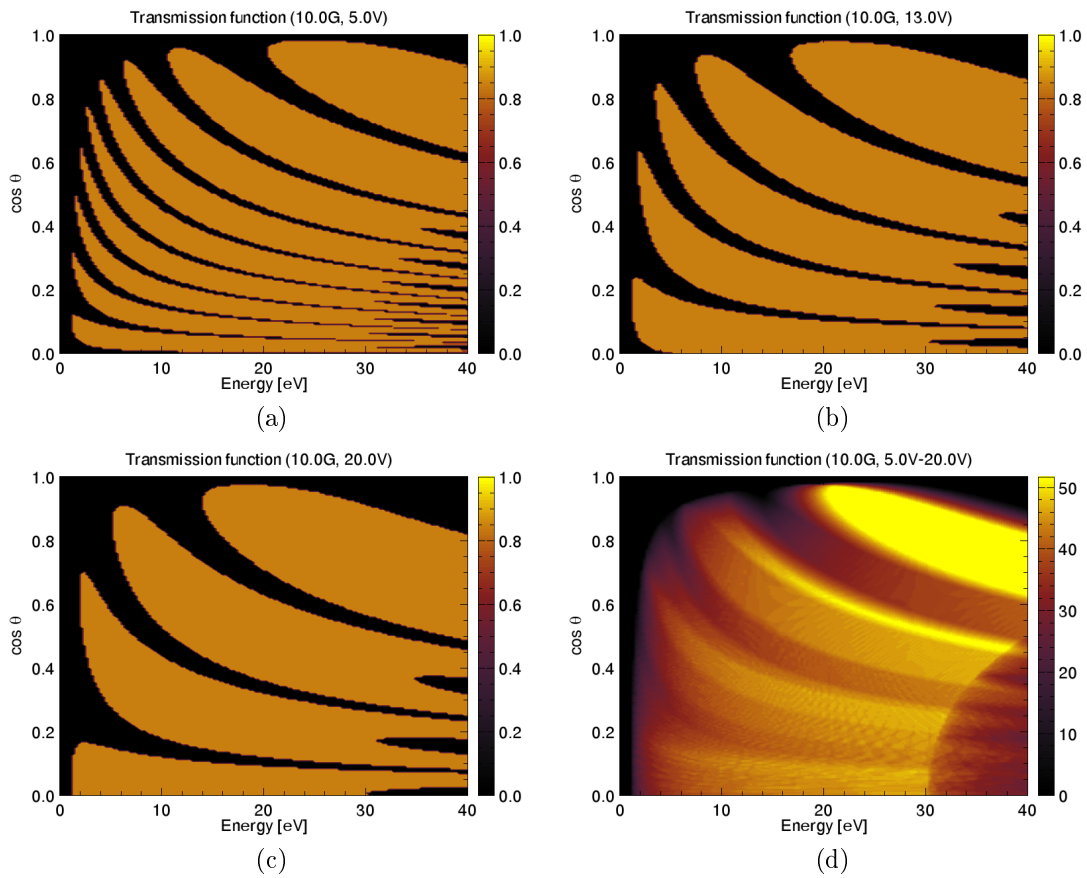


Figure 3.16: (a)-(c): Transmission function of the spectrometer for various electric fields from 19.8 V/m to 79.4 V/m, while the magnetic field stays the same. (d): Cumulative transmission function if the electric field is changed periodically. θ is the polar emission angle.

ical principles MoVES is based on. But the transmission function is highly dependent on the electric and magnetic field and this can be utilized to improve the situation.

Figure 3.16 and 3.15 show several plots of the transmission function if the electric field and the magnetic field are varied respectively. For both series of plots it can be seen that the “bands” of the transmission function “move” with the change of the electric or magnetic field. A possible process to improve the transmission of the spectrometer is to periodically change the electric or magnetic field during the measurement. In consequence, the transmission function changes periodically with the field as well. The overall transmission, which is the weighted sum of the transmission for every single field setting, then covers a maximum range of energy and emission angle. Plot 3.16d and 3.15d present such a cumulative transmission for electric or magnetic field changes respectively.

It is more tedious to evaluate the data for periodic electric field changes, since the time of the ion–solid impact changes as well. The energy of the ion is influenced by the electric field in the spectrometer as well. On the other hand, a change of the magnetic field has no impact on the ion, as long as the ion path is parallel to the magnetic field. Therefore, it seems more promising to periodically change the magnetic field during the measurement in order to improve the transmission function.

3.4. Analysis of recorded Data

3.4.1. Resort algorithm

The delay line anode (DLA) consists of three layers of wires where the angle between adjacent layers is 60° (see figure 3.17). In a perfect case the electron cloud produced by the MCP will lead to two signals on each layer, one at each end (compare figure 3.20). An electric signal can also be recorded at the MCP voltage supply. These signals are amplified and converted to NIM-signals in a constant fraction timing discriminator (CFT). The NIM-signals trigger a time-to-digital converter (TDC) and the timing information is recorded.

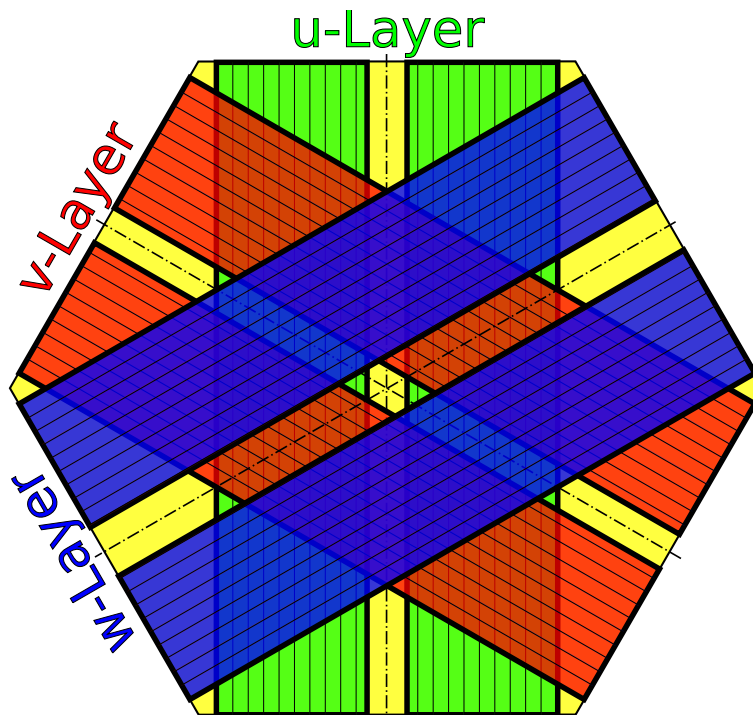


Figure 3.17: This is a schematic drawing of the delay line anode used for this experiment. The DLA consists of three layers of wires u , v and w which provide redundant information for multi-hit capability. Due to the gap in the wiring of the DLA some parts of the MCP are only covered by two layers.

The three layers of the DLA allow to record multiple hits of electrons within a short time period. The time for a signal to travel through a complete wire is about 100 ns. If a second electron is amplified by the MCP within this time, the duration signals can overlap. In addition, due to the dead time of the electronics of about 20 ns, from two signals where the second follows within this dead time, only the first signal will be detected. Also dissipation effects on the anode may weaken the signal below the threshold-level of the CFT. There might be also reflection of signals which needs to be

filtered out. Furthermore, noise may also be amplified and converted by the CFT to NIM-signals. A resort algorithm should be able to discard false signals and recreate true electron events even if not all DLA signals were recorded.

A computer program was written to sort the recorded data and which tries to reconstruct missing signals. If the information provided by the signals is sufficient, the program calculates the position where the electron hit the MCP. Table 3.1 shows the possible combinations of detected signals.

flag	u	v	w	MCP	notes	flag	u	v	w	MCP	notes	
0	2	2	2	1	most reliable	7	2	1	0	1	risky	
1	0	2	2	1			1	2	0	1		
	2	0	2	1			2	0	1	1		
	2	2	0	1			1	0	2	1		
2	1	2	2	1			0	2	1	1		
	2	1	2	1			0	1	2	1		
	2	2	1	1		8	1	1	1	1		
3	2	2	2	0	second most reliable	9	2	1	1	0	unreliable	
4	0	2	2	0			1	2	1	0		
	2	0	2	0			1	1	2	0		
	2	2	0	0			10	2	1	0		0
5	1	2	2	0				1	2	0		0
	2	1	2	0				2	0	1		0
	2	2	1	0				1	0	2		0
6	2	1	1	1				0	2	1		0
	1	2	1	1				0	1	2		0
	1	1	2	1				1	1	1		0

Table 3.1: Not every layer and MCP signal can be detected due to the dead time of the electronics, signal overlapping or attenuation. Since the three layers provide redundant information this table contains the various cases for which signals can be partially reconstructed and for which the impact position of the electron can be calculated. In the columns u, v, w and MCP the number of signals detected are given for all possible cases. The reliability of the various cases is indicated in the column “notes”.

Preparation of signals

Before the algorithm is able to process the signals there is some preparation necessary. The program calculates checksums for the decision if signals belong together. In addition, the checksums can be used to recreate lost signals. The difference in the sum of the time recorded for the layer signals t_1, t_2 and the time recorded for the MCP signal t_e is the same for all signals:

$$(t_1 - t_e) + (t_2 - t_e) = t_t + \Delta + t_{c_1} + t_{c_2} = t_{sum}$$

Here, t_t is the transition time of the electron cloud from the MCP to the DLA wires, Δ is the runtime of a signal from one end of the layer to the other and t_{c_1} and t_{c_2} are the runtimes for the signal from each end of the layer to the TDC. All terms on the right hand side are constant and specific for each layer. Since the algorithm expects this sum to be zero, $\frac{1}{2}t_{sum}$ must be subtracted from t_1 and t_2 .

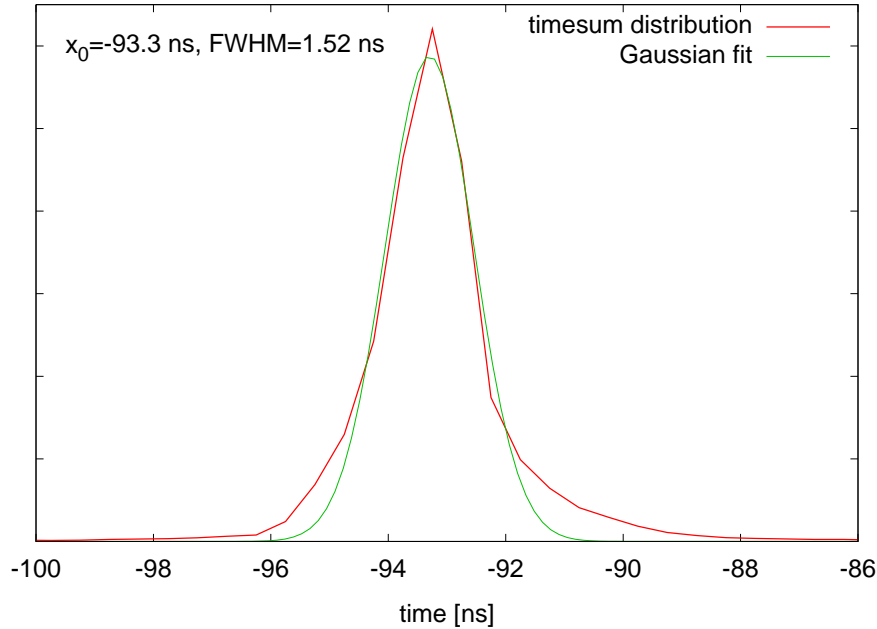


Figure 3.18: This histogram shows the occurrence of the sum $2t_e - (t_1 + t_2)$ for one layer. A Gaussian function is fitted to this distribution to estimate the mean value and the width (FWHM) of the distribution. Both values are needed for the resort algorithm to decide if signal at each end of one layer belong together. Similar histograms are obtained for all three layers.

In order to determine t_{sum} and the acceptance level for the checksums σ_c for each layer, the sum $2t_e - (t_1 + t_2)$ of a number of signals taken from a real experiment has to be determined and plotted (see figure 3.18). A Gaussian curve is fitted into the peak to obtain the peak position (which corresponds to t_{sum}) and the full width half maximum (FWHM) which can be related to the acceptance level σ_c . For the DLA used for MoVES t_{sum} for all layers is about -100 ns and $\sigma_c \approx 1$ ns (compare table 3.2). The difference of t_{sum} for the three layers can be explained due to the different wire lengths of the layers.

The layer offset

If a line for every layer is drawn which divides the layers in half, these three lines won't meet in one point which they should do ideally (see figure 3.19). This is not necessarily due to misalignment of the layers. A offset can also be caused by differences in the cable

	t_{sum}	σ_c
layer u	-93.46ns	0.72
layer v	-93.92ns	0.69
layer w	-100.05ns	0.75

Table 3.2: This tables shows the values t_{sum} and σ_c for all three layers obtained by fitting a Gaussian function to an experimental data set as explained in the paragraph “Preparation of signals”. The consistence of these values needs to be checked for every experiment.

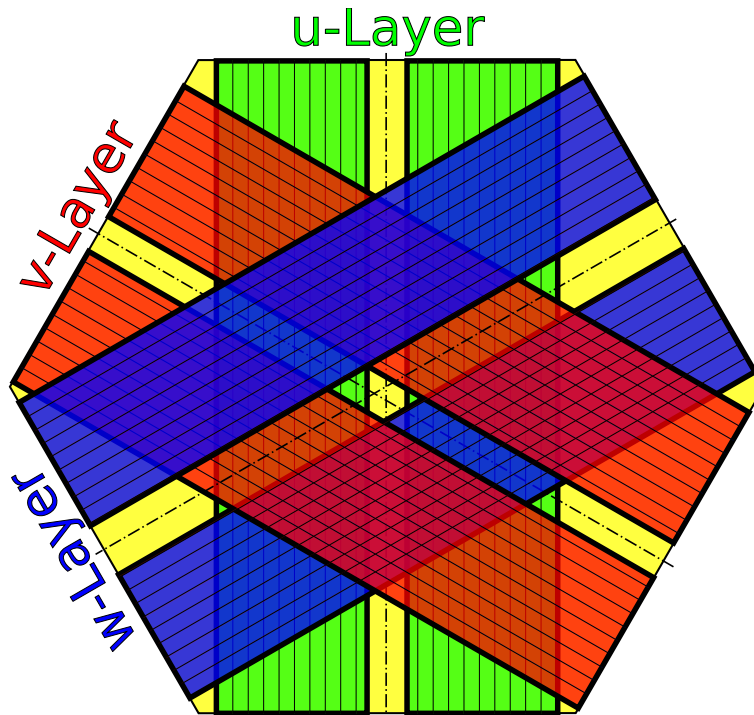


Figure 3.19: For a DLA with three layers the symmetry lines of the layers do not meet in one point in a real application. This offset is due to differences in cable lengths between the TDC and the DLA. The offset parameter can be determined during the calibration of the device.

lengths for both ends of a layer (the velocity of an electric signal in a copper cable is about $v_s \approx 0.3$ m/ns, which is about the speed of light). The offset can be compensated by adding a constant χ to the timing information of one layer

$$t_{w1} = t_{w1} + \chi/2$$

$$t_{w2} = t_{w2} - \chi/2$$

Due to the hole in the DLA this parameter can't be directly determined but the offset χ is one of the parameters established during the calibration of the detector (see section 3.4.2).

Signal speed in layers

Figure 3.20 presents a schematic drawing introducing all quantities considered here. At the time t_1 two signals in either direction are generated. The signals arrive at the end of the wires at different time, t_3 and t_4 respectively, depending on the impact position.

The velocity of the signals in the wire is close to the speed of light. For the determination of the position, the speed of the signals perpendicular to the wire f_u is of interest, which is much slower. The exact knowledge of this velocity f_u enables one to calculate the position x_u of the electron for layer u from the difference of the signal times t_{u1} and t_{u2} at each end

$$x_u = (t_{u2} - t_{u1}) \frac{f_u}{2} + \frac{t_{u2} - t_{u1}}{|t_{u2} - t_{u1}|} \frac{g_u}{2} \quad (3.48)$$

where g_u is the size of the gap due to the hole in the MCP. The second term adds half the gap to the position x_u since the gap is not included in the time difference. Note, that it is not necessary to know when the electron cloud hits the layer. The difference of the signal times provides the information needed, but one must still be sure that the signals belong together. Equation 3.48 is also valid for the layers v and w respectively.

The signal speed can be crudely estimated if the maximum time difference $t_{u2} - t_{u1}$ is determined, which corresponds to hits at the border of the MCP ($x_u = R_{MCP}$). f_u can then be assessed using eq. 3.48. Still, the signal velocities need to be determined during the calibration process as explained later (see section 3.4.2).

Data sorting and evaluation

For the evaluation of the first experiments a program was written which covers the cases 0 and 1 in the table 3.1. The software expects timing information (MCP signal and two signals of each layer) of signals prepared as described before. Together with the offset it is now possible to find signals which belong together. In the following a short description of the sorting algorithm used in the program is given.

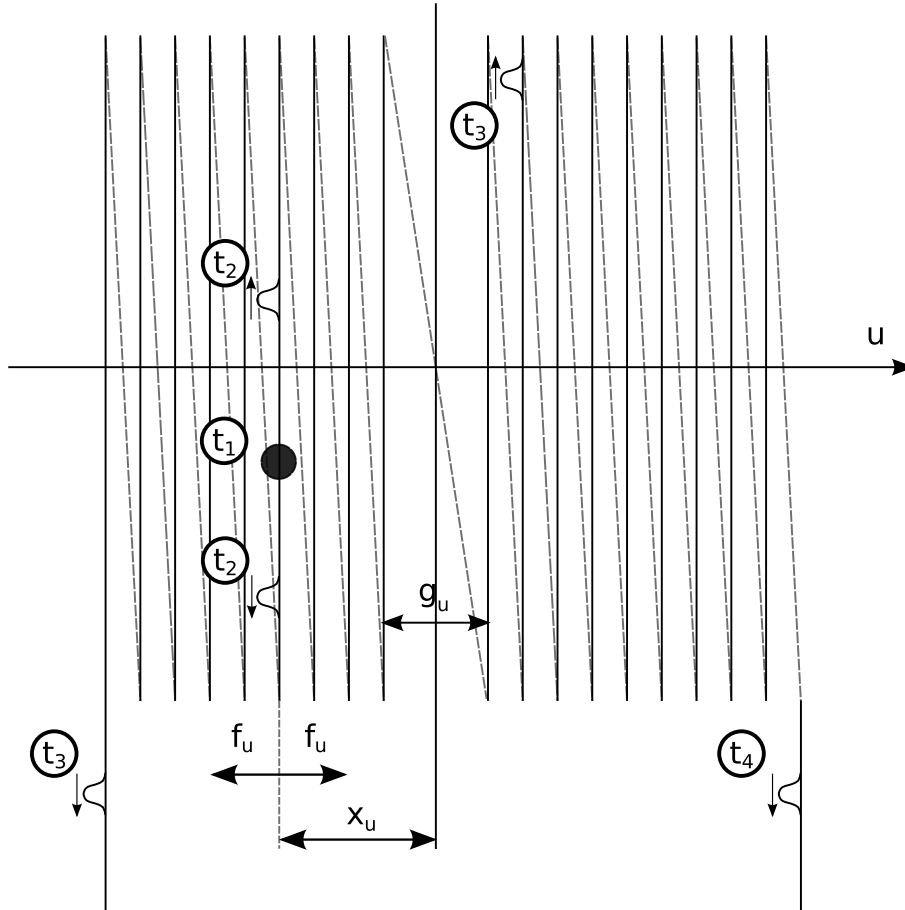


Figure 3.20: Schematic drawing of the wiring of one of the DLA layers. At the time t_1 an electron cloud produced by the MCP hits the wire and causes two pulses to advance to each end of the wire. Since both pulses travel with the same speed, their distance from the point of creation is always equal (e.g. at the time t_2). The signal velocity f_u perpendicular to the wires is much smaller than the speed of electric signals in a conducting wire (which is close to the speed of light). At t_3 and t_4 the signals will be detected at the ends of the wire respectively. The time difference $t_3 - t_4$ together with the knowledge of f_u is used to determine the position x_u where the impact occurred (compare equation 3.48). g_u is the size of the gap for this layer.

- For every MCP signal the layer signals are evaluated.
- For every signal t_1 on one end of the layer the sum $2t_e - (t_1 + t_2)$ with the MCP signal t_e and one other layer end's signal is calculated. If the signals belong together this sum must be close to zero (smaller than the acceptance level σ_c).
- The last step is done for every layer. Signals are assigned to a real event if the last step was successful at least for two layers.

This algorithm disregards all electron events for which the corresponding MCP signal is not recorded.

From this set of signals we can now calculate the impact position on the MCP. For every signal pair the position on the layer axis can be calculated using equation 3.48. We obtain at least two of the three possible positions x_u , x_v and x_w . We can calculate the impact position from either combination of these values.

$$\begin{aligned} X_{uv} &= x_u \\ Y_{uv} &= \frac{x_u - 2x_v}{\sqrt{3}} \end{aligned} \quad (3.49)$$

$$\begin{aligned} X_{uw} &= x_u \\ Y_{uw} &= \frac{-2x_w - x_u}{\sqrt{3}} \end{aligned} \quad (3.50)$$

$$\begin{aligned} X_{vw} &= x_v - x_w \\ Y_{vw} &= \frac{-x_w - x_v}{\sqrt{3}} \end{aligned} \quad (3.51)$$

If only two layers responded to the electron cloud, the position corresponds directly to one of the formulas above. For example, if layer v and w delivered signals belonging to a MCP signal we obtain

$$X = X_{vw} \quad Y = Y_{vw}$$

In case signal pairs could be found for all three layers the impact position can be calculated to

$$X = \frac{X_{uv} + X_{uw} + X_{vw}}{3} \quad Y = \frac{Y_{uv} + Y_{uw} + Y_{vw}}{3}$$

For the last case it is also possible to estimate the quality of the position calculation. We define

$$\delta := X_{uw} - X_{vw} = x_u - x_v + x_w \quad (3.52)$$

which should be close to zero. This quantity can be used to determine the quality of the evaluation, since the lateral resolution can be estimated from it. During the calibration process the algorithm tries to find a minimum of the quantity δ .

3.4.2. Calibration of detector parameters

In order to obtain the best resolution possible various parameters need to be optimized: the signal speed f_1 , f_2 and f_3 in the layers, the layer offset χ and the gap sizes g_u , g_v and g_w . Since all these parameters have an influence on each other, all parameters have to be calibrated in one step.

An algorithm was written to find a minimum of the quality parameter δ (see eq. 3.52) in given parameter ranges. The parameter f_1 has to be estimated using equation 3.48. Here we set x_u to the MCP radius and $t_{u2} - t_{u1}$ equals the maximum time difference of the signals observed (normally around 100 ns). The gap sizes g_u , g_v and g_w are measured directly with a sliding calliper. We then introduce a so called gap factor γ , which scales all gap sizes at once:

$$g'_u = \gamma g_u, \quad g'_v = \gamma g_v, \quad g'_w = \gamma g_w$$

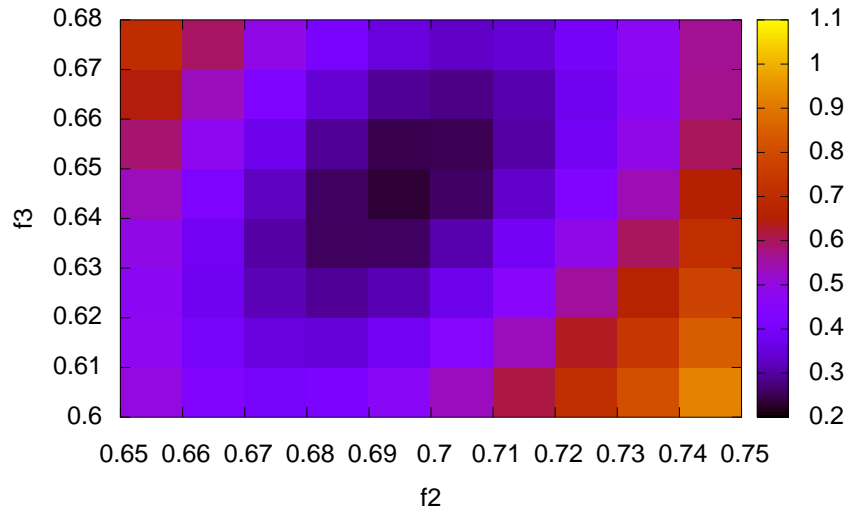
It is not possible to alter the gap sizes independently since one of them would always converge towards zero.

The algorithm then varies f_2 , f_3 , χ and γ in given ranges and determines the mean quality parameter $\bar{\delta}$ for a real data set. This is achieved by using a double loop. In the outer loop χ and γ are varied according to the settings. Inside this loop a second loop varies f_2 and f_3 and the smallest mean quality value $\bar{\delta}(\chi, \gamma)$ is determined (see contour plot 3.21a). For all χ and γ values we then plot $\bar{\delta}(\chi, \gamma)$ in another contour plot (see figure 3.21b) to determine the parameter set, where the best resolution (i.e. minimal quality parameter δ) is achieved.

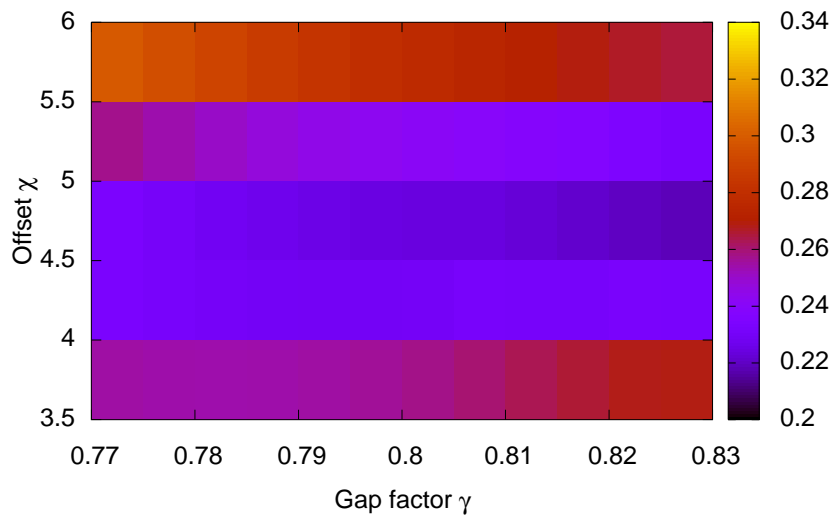
Parameters	Value
f_1	0.71
f_2	0.7
f_3	0.65
γ	0.82
χ	4.5
δ	0.32

Table 3.3: From a real experimental data set f_1 , f_2 , f_3 , γ and χ were determined via the calibration process. For the values presented in this table the quality parameter δ is at a minimum of 0.32.

This procedure needs to be done before any evaluation of real data sets, since changes at the spectrometer (e.g. exchange of cables) might have altered these parameters. Table 3.3 shows parameters determined from a real data set. The lateral resolution reached here is only 0.32 mm, though in the specifications for the MCP/DLA combination 0.15 mm is given. One possible explanation for this difference might be the jitter of the NIM-signals produced by the CFT in the order of some 100 ps induced by noise.



(a)



(b)

Figure 3.21: During the calibration process four quantities (f_2 , f_3 , χ and γ) are varied in given ranges in a double loop. In the inner loop, for a certain set of χ and γ , f_2 and f_3 are set stepwise and the quality parameter is determined for every set. Plot (a) shows the resulting contour plot, from which a minimum $\bar{\delta}(\chi, \gamma)$ can be determined. $\bar{\delta}(\chi, \gamma)$ is now calculated for a certain range of χ and γ and plotted again in a contour plot (figure b). The minimum in this plot corresponds to the best possible choice of f_2 , f_3 , χ and γ .

Two other parameters influence the quality of position detection. The acceptance level σ_c described in the subsection “Preparations of signals” in section 3.4.1 determines which signal pairs are considered as “true” signals produced by electrons. If this parameter is chosen too small, true events might be rejected. On the other hand the lateral resolution decreases if this parameter is too big, since signal pairs of bad quality are accepted as well. Figure 3.22a shows the influence of the acceptance level σ_c . Here measurements were evaluated for various values of this parameter while other parameters were kept constant. It can be seen that the quality parameter δ in general increases with higher σ_c which corresponds to a lower lateral resolution. On the other hand the number of two layer events (N_{e2}) and three layer events (N_{e3}) increases steadily with increasing σ_c . σ_c needs to be chosen in such a way as to achieve a maximum number of events while maintaining an acceptable lateral resolution.

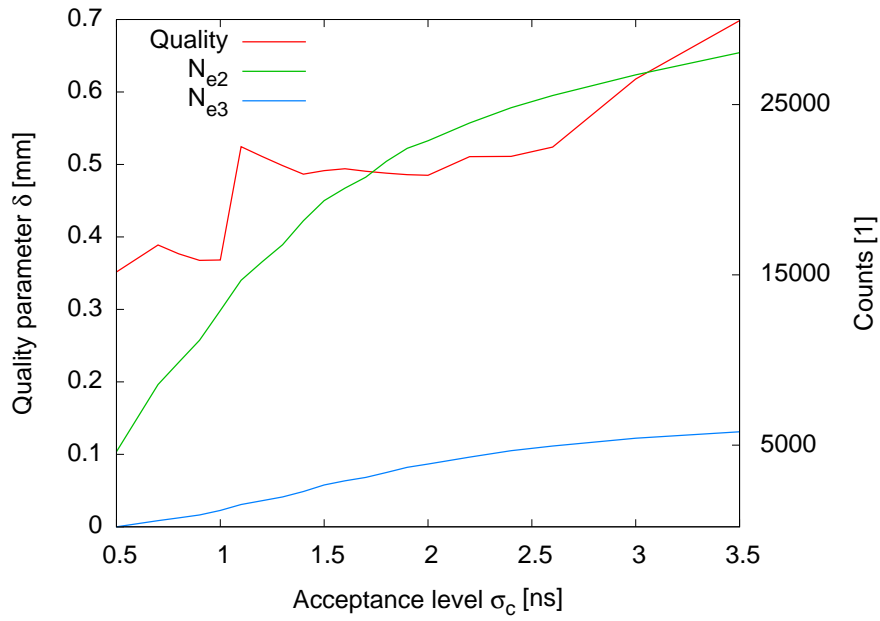
In addition, it turns out that if signals are accepted which were produced close to a gap of a layer, the lateral resolution decreases significantly. This effect can also be seen on a histogram of time difference of signals from each end. One would expect that there is no influence of the gap, since signals just “pass” the gap practically in no time. But in figure 3.23 it can be seen, that between about -10 ns and 10 ns there is a significant drop in the countrate. Therefore, signals which stem from close the gap area are not very reliable and should generally be rejected. Hence, in the algorithm only those signal pairs are accepted, where the time difference is larger than a certain value. An evaluation was done what influence this minimal time difference value has on the lateral resolution. In figure 3.22a it can be clearly seen, that below a certain value for the time difference of about 10 ns the quality parameter δ increases significantly which corresponds to a decrease in lateral resolution. All other parameters were kept constant in this evaluation.

3.4.3. Determination of the time of ion-solid impact

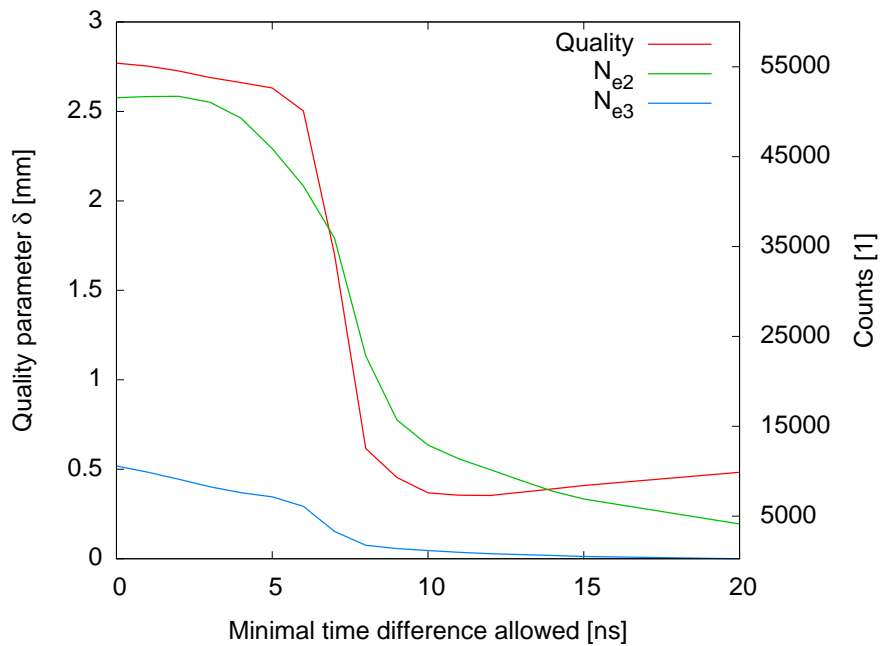
In the first stage of the novel electron spectrometer MoVES, there is no possibility to measure the ion pulses directly at the position of the sample, apart from the current at the sample. But for a chopped ion beam in the best case only about 10^4 ions will reach the sample which can’t be measured even with an pico-Amperemeter. Hence, it is not possible to determine directly the time t_s when the ion pulses hit the sample.

One possible solution used in this work to solve this problem is to use the fact that the cyclotron time t_c is only dependent on the strength of the magnetic field (figure 3.24 and 3.25 show the dependency of the cyclotron time on the magnetic field for fields below 0.5 mT and between 0.5 mT and 2 mT respectively). Therefore, all electrons regardless of their energy cross the spectrometer axis at the times $t_c, 2t_c, 3t_c, \dots$. Similar, all electrons reach the maximum distance to the axis, which is twice the cyclotron radius r_c (compare section 3.3.6), at the times $\frac{1}{2}t_c, \frac{3}{2}t_c, \frac{5}{2}t_c, \dots$

Furthermore it is assumed, that the center of our circular MCP is the origin of our coordinate axis. If one then produces histograms of the length r of the position vectors



(a)



(b)

Figure 3.22: Plot (a) shows the dependence of the quality parameter δ from the acceptance level σ_c while other parameters were kept constant. In general it can be seen that the number of electron events (N_{e2}, N_{e3}) increases and the lateral resolution decreases with increasing σ_c . Plot (b) depicts how the quality parameter δ decreases and therefore the lateral resolution improves if signals are rejected which were produced close to the gap of a layer. From a time difference of 10 ns on the lateral resolution doesn't improve any further.

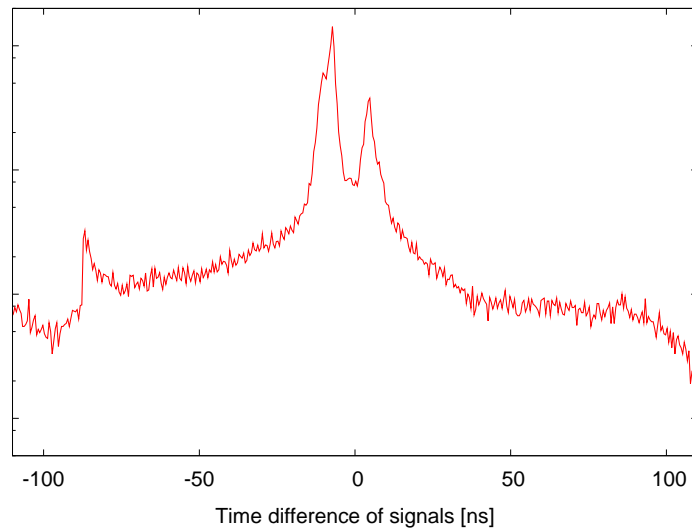


Figure 3.23: Electrons which hit the MCP close to the layer gaps are not reliably detected with the MCP/DLA combination used. The drop in countrate between -10 ns and 10 ns should normally be not experienced since the signals pass the gap in practically no time. Therefore signal pairs are only accepted if the time difference between them is larger than ~ 10 ns.

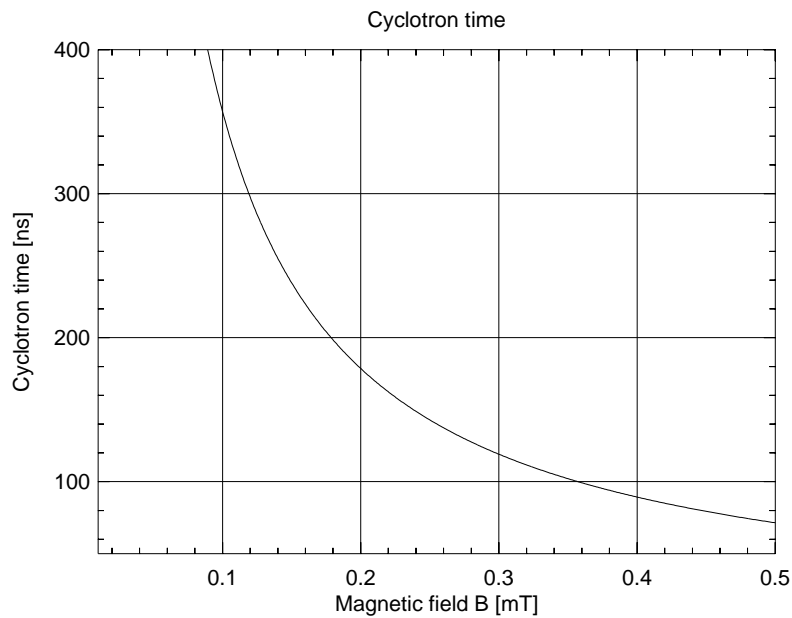


Figure 3.24: Dependence of the cyclotron time t_c on the magnetic field B for field intensities below 0.5 mT.

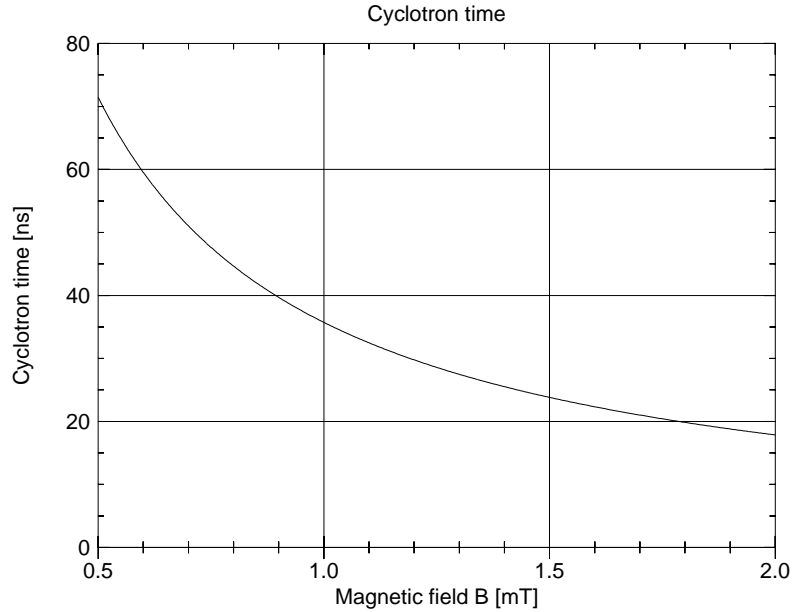


Figure 3.25: Dependence of the cyclotron time t_c on the magnetic field B for field intensities from 0.5 mT to 2.0 mT.

where the electrons hit the MCP over the time of flight t (called r -over- t -histograms), we obtain plots similar to figure 3.26. One can clearly see that the electrons reach their maximum distance from the origin at the same time. It is now possible to determine the cyclotron time t_c , e.g. by determine the position of the maxima of the peaks. It is assumed that t_p is the position of one peak. Hence, for the time t_s when the ion-solid interaction takes place, one finds the expression

$$t_s = \left(t_p - \frac{t_c}{2} \right) - nt_c \quad (3.53)$$

Here, n it is not yet known. For another measurement with a different magnetic field and hence a different cyclotron time t'_c we can again determine the peak position t'_p and obtain

$$t_s = \left(t'_p - \frac{t'_c}{2} \right) - mt'_c \quad (3.54)$$

The time t_s doesn't change if the magnetic field is modified. To determine t_s , values calculated from equation 3.53 and 3.54 for $n = 1, 2, \dots$ and $m = 1, 2, \dots$ are compared in a table. The time which is about the same in all columns is then regarded as the start time t_s (compare table 3.4)

In figure 3.26 four r -over- t -histograms for measurements with different magnetic fields are shown. The peak positions and the cyclotron time were determined. Table 3.4 shows the series of possible start times for all four measurements. We conclude from this evaluation that for these measurements $t_s = 12370$ ns.

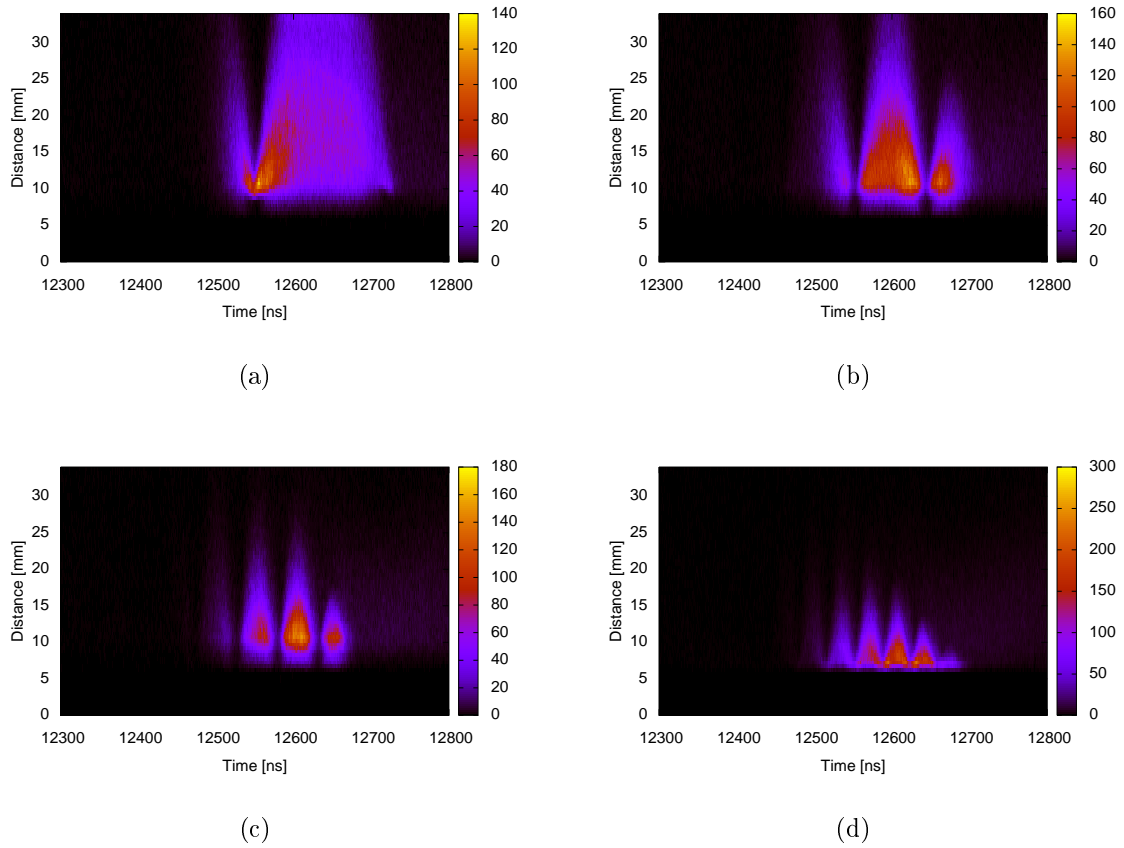


Figure 3.26: Histograms of the distance of the impact position to the MCP center r over the time t for several magnetic fields (2 G, 4 G, 7 G and 10 G). At the times $t_c, 2t_c, 3t_c, \dots$ all electrons regardless their energy or emission direction cross the spectrometer axis. At the times $\frac{1}{2}t_c, \frac{3}{2}t_c, \frac{5}{2}t_c, \dots$ the electrons reach their maximum distance from the axis. From these series of histograms the cyclotron times for the various magnetic fields can be determined, as well the time at which ion–solid interaction takes place.

	2 G	4 G	7 G	10 G
t_c	180.5	91	53.8	36.6
	12550	12551	12525	12516
	12370	12460	12471	12479
	12189	12369	12418	12443
	12009	12278	12367	12406
	11828	12187	12313	12370

Table 3.4: Histograms (see figure 3.26) for different magnetic field intensities (2 G, 4 G, 7 G and 10 G) were evaluated for the cyclotron time t_c and the time of ion–solid interaction t_s . For every measurement a series of possible t_s was determined. Since t_s doesn't depend on the magnetic field, the time which can be found in every series (here, $t_s = 12370$ ns, bold) is the actual time where the ions hit the sample. All times in the table are in ns.

3.4.4. Determination of the spectrometer axis

With the help of the Faraday cup we can determine the position of the continuous beam at the sample. Since the chopped beam can not be measured at the sample we can only assume, that the chopped beam hits the sample close to this position. In addition, although the strength of the magnetic field can be determined by means of the cyclotron time (see section 3.4.3), the exact direction of the magnetic field is not known. But from the position information at the MCP one can determine where the spectrometer axis crosses the front of the MCP.

It is important to understand that the spectrometer axis is defined by the impact position of the ion at the sample and the direction of the magnetic field and not by the electrode axis and therefore not by the electric field (compare section 3.4.5).

To determine the position of the spectrometer axis at the MCP we produce several plots from the position information at the MCP for different thresholds for the count rate of a position. We obtain contour plots where the z value is zero if the count rate at (x, y) is smaller than the threshold and 1 otherwise. The z value at the dead area of the MCP is always set to 1. For all plots generated we can now determine the center of gravity (COG) of the areas where $z = 1$. The mean value of all determined COG is then an estimate for the position where the spectrometer axis crosses the MCP front. This is only true if we expect no dependence on the azimuthal angle ϕ . A program was written to automate this process. Figure 3.27 shows two of the contour plots. The COG are marked with a cross.

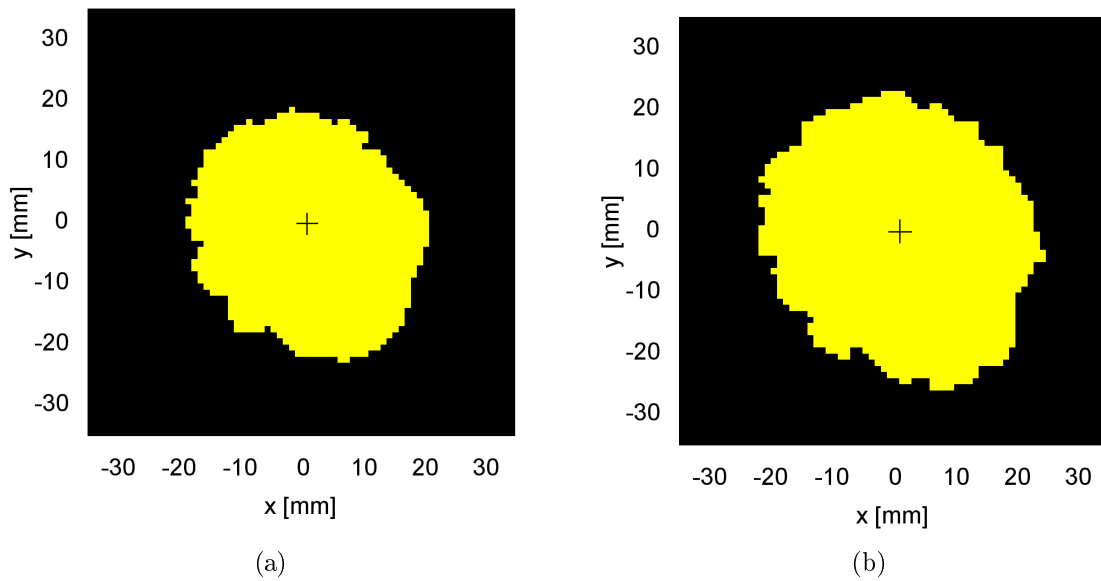


Figure 3.27: In order to determine where the axis of the spectrometer crosses the MCP impact position contour plots are generated where the z value for a position is 0 if the number of hits is below a certain threshold or 1 otherwise. The center of gravity of the obtained areas are determined for several thresholds (here, in plot (a) the threshold is 48 and in (b) 19). The average of the COGs is an estimate of the spectrometer axis position. For this experimental data set the average COG is at $x = 1.2$ mm and $y = -1.5$ mm.

3.4.5. Influence of misalignment between magnetic and electric field - the $\mathbf{E} \times \mathbf{B}$ drift

In case the electric and magnetic field are not perfectly aligned an additional movement of the electrons, the so called $\mathbf{E} \times \mathbf{B}$ -drift, occurs. This effect is easy to understand. It is assumed, that the electron velocity \mathbf{v} and the electric field \mathbf{E} are decomposed in components parallel and normal to the direction of the magnetic field \mathbf{B}

$$\mathbf{v} = \mathbf{v}_{\parallel} + \mathbf{v}_{\perp}, \quad \mathbf{E} = \mathbf{E}_{\parallel} + \mathbf{E}_{\perp}$$

The parallel component of the electric field just leads to an acceleration in the direction of \mathbf{B} , which is addressed in section 3.3.6. The equation of motion for electrons with the mass m_e normal to the magnetic field is

$$m_e \frac{d\mathbf{v}_{\perp}}{dt} = -e(\mathbf{E}_{\perp} + \mathbf{v}_{\perp} \times \mathbf{B}) \quad (3.55)$$

where e is the elementary charge. Equation 3.55 can be solved with the Ansatz

$$\mathbf{v}_{\perp} = \mathbf{v}'_{\perp} + \mathbf{v}_{\mathbf{E}}$$

where

$$\mathbf{v}_{\mathbf{E}} := \frac{\mathbf{E} \times \mathbf{B}}{B^2}$$

is defined as the drift velocity. Equation 3.55 then reduces to

$$m \frac{d\mathbf{v}'_{\perp}}{dt} = -e(\mathbf{v}'_{\perp} \times \mathbf{B})$$

We conclude that if we switch to a new frame of reference moving with the velocity $\mathbf{v}_{\mathbf{E}}$ relative to the laboratory system the electrons again follow a cyclotron movement. Hence, in the laboratory system the electrons move on a cyclotron trajectory with a constant electric drift $\mathbf{v}_{\mathbf{E}}$.

In case the magnetic field compensation is turned on the misalignment of \mathbf{E} and \mathbf{B} is typically not more than $\vartheta = 0.5^\circ$. For a magnetic field strength of $B = 1$ mT and an electric field of $E = 120$ V/m the electric drift amounts to $v_E \approx 2000$ m/s. For a maximal time of flight of 200 ns we obtain a maximal drift of 0.2 mm which is less than the actual lateral resolution achieved in the measurements conducted in this work. Therefore, in a first approximation the electric drift can be disregarded in cases where the magnetic field compensation is turned on.

It is also possible to turn off one of the compensation Helmholtz coils so that the spectrometer axis crosses the MCP front in an area where electrons can be detected. In this case part of the earth magnetic field is not compensated and there is a considerable misalignment between the electric and magnetic field. Here, the $\mathbf{E} \times \mathbf{B}$ -drift has to be taken into account since it is more than two orders of magnitude higher than the lateral resolution.

3.5. Aspects and Design of a Pulsed Ion Source

The MoVE spectrometer is an electron spectrometer where it is possible by design to use electrons, ions or photons as incident radiation. As a first test of this spectrometer it was decided to investigate the ion induced emission of electrons to obtain a better understanding about the kinetic emission of very slow ions. For these experiments a pulsed ion source had to be designed and built which is able to produce ion pulses with a packet length of the order of 1 ns.

3.5.1. Principle of Operation

Singly charged ions are produced with a thermionic ion source. These so emitted thermic ions (about ~ 200 meV) are accelerated to a given energy and focused on collimators. The collimated beam enters the ion chopper which deflects the beam over a slit by a fast clamping of charged deflection plates (see figure 3.35 for a schematic drawing). Depending on the chopper parameters and the ion's mass, packet lengths from 0.5 ns to some ns are possible.

3.5.2. Specifications

Ion source The principle of the thermionic ion source is already known since 1916 [80]. A matrix material on which emitter material is placed is heated up to a temperature where ions are emitted due the thermionic effect. During the emission the atoms of the emitter material are stripped off an electron due to potential effects. Since the ion source usually operates at a temperature of 1100°C the thermal energy of the emitted ions is about $\frac{3}{2}kT = 177$ meV. For this experiment an thermionic ion source of HeatWave Labs was bought with specified current densities of up to 10 mA/cm². This ion source is usually used for SIMS (secondary ions mass spectroscopy) and can be operated with ${}^6\text{Li}^+$, Na^+ , K^+ , Rb^+ , Cs^+ ions over an energy range from 1 to 15 keV.

Chopper The chopper was bought from the Johannes Kepler University in Linz and its features and properties are described elsewhere [10] in great detail. The principle of this chopper is based on the theory presented by J.M.B. Bakker [6, 7]. The electronics of this chopper allow to clamp the deflection plates in only ~ 4 ns. The maximum frequency practically achievable is about 100 kHz. Since the distance between the plates is about 4 mm and the maximum voltage difference between the plates is 200 V, a maximum electric field between the plates of 50 kV/m can be produced.

UHV chamber A UHV chamber was designed and built where the ion chopper and ion gun are mounted. This chamber is connected to the spectrometer chamber via a

bellow, so that the chambers can be moved and rotated in with respect to each other to a certain degree. Since the ion chopper is mounted on the chamber at an ISO-160 flange with a Viton gasket, the pressure in this chamber is limited to $\sim 10^8$ mbar. A Pfeiffer/Balzers turbomolecular drag pump (TPU 330) pumps the chamber. An UHV Bayard-Alpert combination gauge of AML (AlG17G) measures the pressure. The whole chamber can be baked by heat bands. For the chamber only stainless austenitic steel (316 and 304) was used to minimize the influence on the produced magnetic field.

3.5.3. Time resolution of Ion Pulses

The packet length of the ion bunches depends on the energy spread of the ion source, the length differences of the various paths ions can travel through the lenses and the chopping process.

All these time uncertainties add up to the effective time resolution of the ion beam pulse following the rules of error propagation:

$$\Delta t = \sqrt{(\Delta t_e)^2 + (\Delta t_p)^2 + (\Delta t_c)^2}$$

Δt_e is the uncertainty in time due to the energy spread of the ion source; Δt_p is the time spread because of the different path lengths in the lenses and Δt_c is the packet length of the ion bunches due to the chop process. All three aspects will be further explained in the next paragraphs.

Energy resolution of the ion source

The energy resolution of the ion source has a direct impact on the time resolution of the pulsed beam which follows from the propagation of uncertainty. An ion with the Energy E needs the time t to cover a distance s

$$t = \sqrt{\frac{s^2 m}{2E}}$$

For an energy spread ΔE the packet length Δt can be obtained then from

$$\Delta t = \frac{t}{2E} \Delta E$$

Table 3.5 shows the pulse length for various energy spreads of a 5 keV Cs⁺ ion beam for a drift length of 1300 mm. It can be seen that if the time resolution of 60 ps of the

time-to-digital converter should be matched by the packet length of the ion pulse the energy resolution of the ion source must be in the order of 100 meV. Therefore electron cyclotron resonance (ECR) ion sources like SOPHIE [32] of the Institut für Allgemeine Physik can not be used without an energy monochromator, since their energy resolution for 5 keV ion beams would be in the order of some eV.

dE [eV]	dt [s]
0.1	$8.25 \cdot 10^{-11}$
0.5	$4.12 \cdot 10^{-10}$
1.0	$8.25 \cdot 10^{-10}$
2.0	$1.65 \cdot 10^{-9}$
5.0	$4.12 \cdot 10^{-9}$

Table 3.5: Packet length of a 5 keV Cs⁺ ion pulse after a 1.3 m flight length for a range of energy uncertainties.

Thermionic ion sources [80] have typically a far better energy spread. The ion gun is operated at a temperature of 1100°C, hence, the thermal energy of the emitted ions is $\frac{3}{2}kt = 177$ meV which corresponds to the energy spread of such ion sources. It was therefore decided to use a thermionic ion source from HeatWave Labs which is usually applied in SIMS (secondary ions mass spectroscopy) applications.

Packet length of ion bunches

Ion bunches are created if an ion beam is deflected over a slit by a very fast change of a transversal electric field. The deflection process was investigated to a great deal by J.M.B. Bakker [6, 7] and is summarized in the next paragraphs.

The effect on an ion beam by fast clamping of deflection plates can be seen in Figure 3.28. A homogeneous monoenergetic ion beam of the width B , ion mass m and energy eU_1 enters the deflection plates with the length l and separation D from the left side. As long as the ion beam is between the plates an electric field E accelerates the beam perpendicular to the initial motion. After the plates the beam travels the length L until it reaches the slit with the size S . The ions need the time t_1 to pass the plates. At the time t_3 the fast change of the voltages at the deflection plates takes place.

Any ions which passes the deflection plates at a time where no change of electric field takes place will experience either a downward or upward force depending on the direction of the electric field. The trajectories $e_0 - a_0 - a_1 - a_2$ and $e_0 - e_1 - e_2$ exemplify these cases. If the fast clamping of the deflection plates occurs while the ions are between the plates, both upward and downward forces are applied to the ions. The exact position of the ion when the field change at the time T_0 takes place determines the trajectory of the ion after the plates.

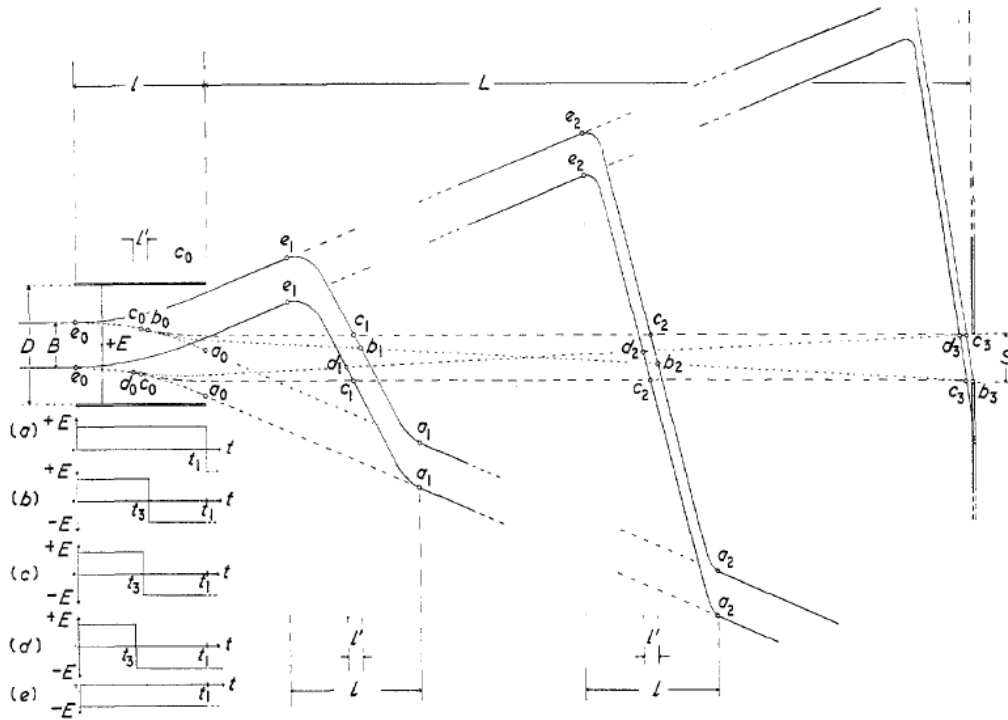


Figure 3.28: All possible ion beam profiles are shown depending on the time when the electric field is switched. For the various cases in the bottom left corner the electric field over time is shown. Ions get through the slit for the cases b, c and d, while for a and e the beam is completely deflected. The boundary cases b and d determine the packet length according to the time interval between them (figure taken from [6]).

Ions at the position c_0 only suffer a small displacement perpendicular to the initial motion, since upward and downward forces are applied the same amount of time ($c_0 - c_1 - c_2 - c_3$). If the slit is placed as in figure 3.28 then these are the ions which will pass the slits. The limiting cases are given by ions at the positions b_0 and d_0 . Ions at the position b_0 experience the downward force a longer time since in that case $t_3 > t_1/2$. Hence, these ions have a small velocity in the downward direction and the path is then $b_0 - b_1 - b_2 - b_3$. Any ions for which the clamping of the plates is later than for the b_0 ions will not enter the slit S . The situation is similar for ions at the position d_0 . Since $t_3 < t_1/2$ they have small velocity component upwards and they are just barely able to enter the slit ($d_0 - d_1 - d_2 - d_3$). All ions which experience a fast field switch earlier than the d_0 ions will not be able to pass the slit.

To put the considerations above in other words, a homogeneous beam of ions passes the deflection plates which produce an electric field forcing the beam downwards. After a fast change of the electric field the beam exhibits a 'kink'. The beam together with the kink continue to travel towards the slit with unchanged velocity in this direction. Since ions at the e position have the greatest upward velocity and ions at the a position have the greatest downward velocity the kink will expand up- and downward. Of all ions affected by the field change only the ions inside the boundary $c_0 - b_0 - c_0 - d_0$ will pass the slit. It is also straight forward to determine the time duration of the ion bunch emerging from the slit. The time difference between the times when b -ions and d -ions pass the slit equals the time duration of the ion bunch, since the b ions enter the slit first, while the d ions pass last.

So far we assumed that the time to change the electric field is zero. Since this can't be achieved, a more realistic concept was developed in [6]. Figure 3.29 shows the basic concept and the terminology used. t_1 is the transit time of the ions in the plates, while t_2 is the time needed to reach the slit from the deflection unit. At the time t_3 the change of the electric field starts to take place. t_4 is the time needed for the fast clamping of the plates. t_1 , t_2 and t_3 are dependent on the ion mass, while t_4 is a constant of the deflection unit. The time duration of the ion bunch Δt_c for a finite clamping time of the deflection plates can be calculated to [6]

$$\Delta t_c = \frac{(B + S) m D}{e V_0 \sqrt{2t_1^2 + 4t_1 t_2 + 4t_2^2 - \frac{1}{3}t_4^2}}$$

where V_0 is the voltage difference of the deflection plates. Note, that Δt_c is proportional to the ion mass m and the inverse of the deflection voltage V_0 .

Since the ion source used for the first experiments can be assembled with different Alkaline metals figures 3.30 to 3.34 show calculated time durations of the ion bunches for ${}^6\text{Li}^+$, Na^+ , K^+ , Rb^+ , Cs^+ ions for an energy range of 1 to 15 keV and several deflection voltages.

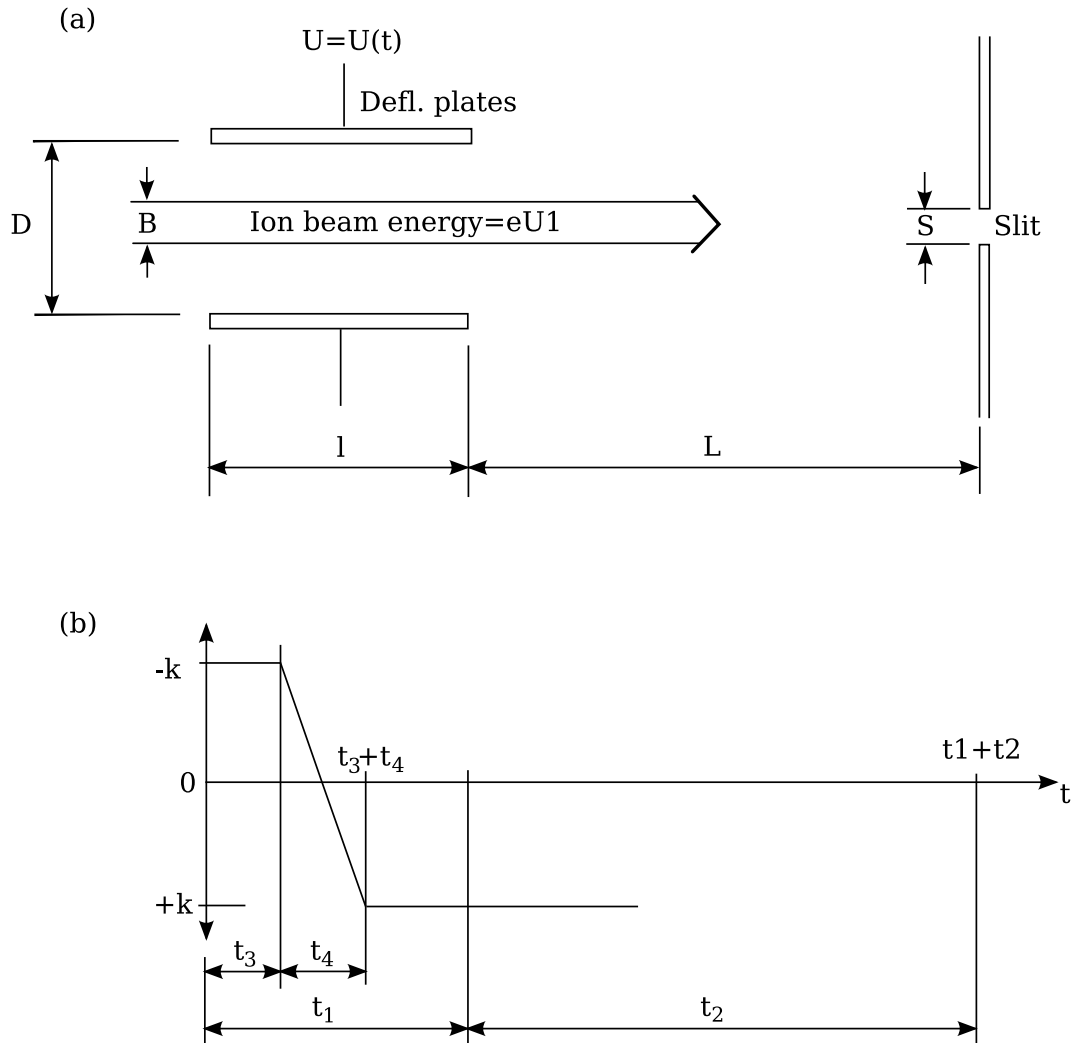


Figure 3.29: Nomenclature used in the theory of ion bunch production. The chopper geometry and the beam properties are indicated in figure (a). Figure (b) shows the electric field over time. t_1 , t_2 and t_3 are directly related to the velocity of the incoming particle. The clamping time t_4 only depends on the electronics and the capacity of the plates [6].

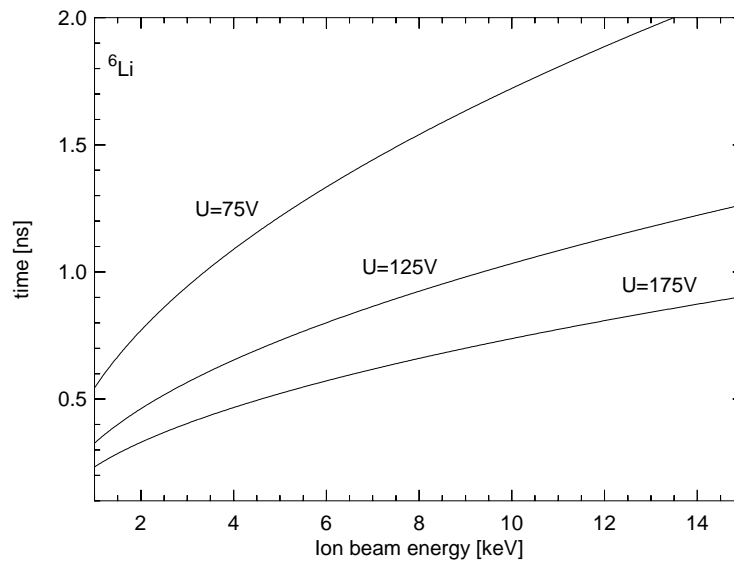


Figure 3.30: Packet length for ${}^6\text{Li}^+$ ions for an energy range from 1 to 15 keV for various deflection plate voltages.

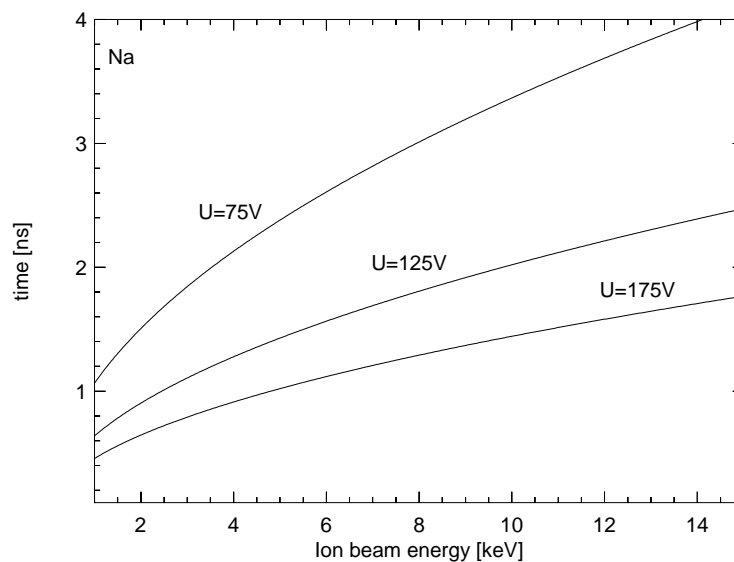


Figure 3.31: Packet length for Na^+ ions for an energy range from 1 to 15 keV for various deflection plate voltages.

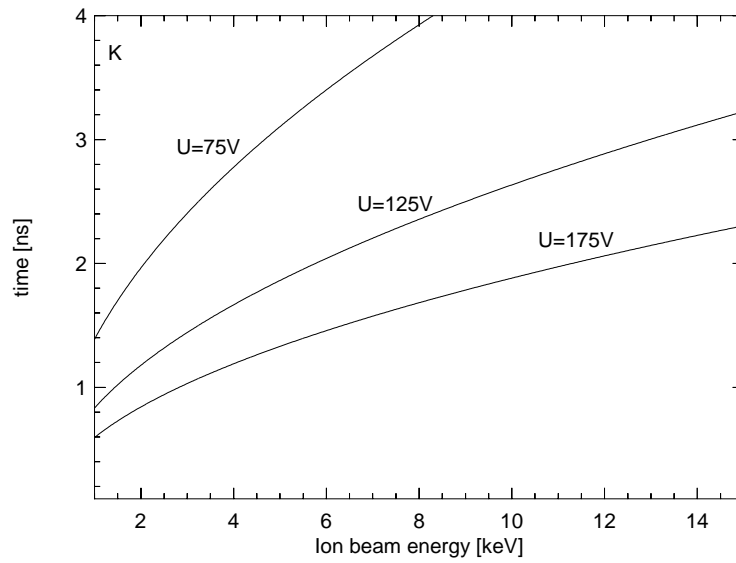


Figure 3.32: Packet length for K^+ ions for an energy range from 1 to 15 keV for various deflection plate voltages.

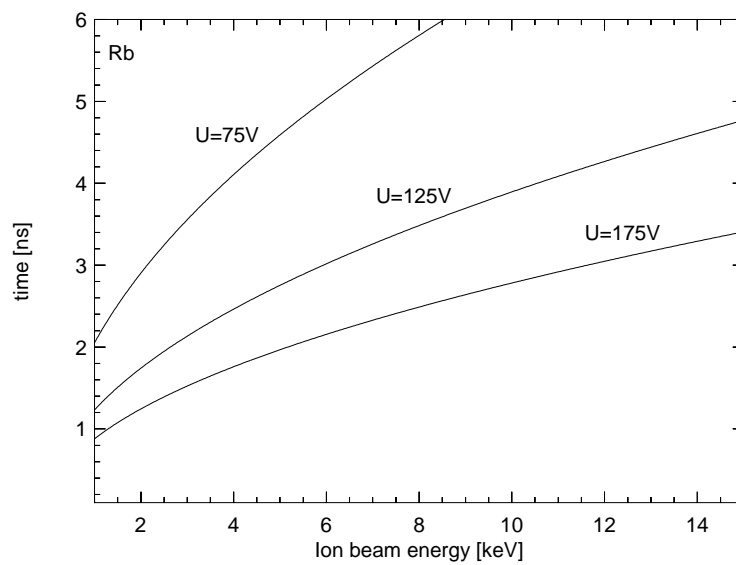


Figure 3.33: Packet length for Rb^+ ions for an energy range from 1 to 15 keV for various deflection plate voltages.

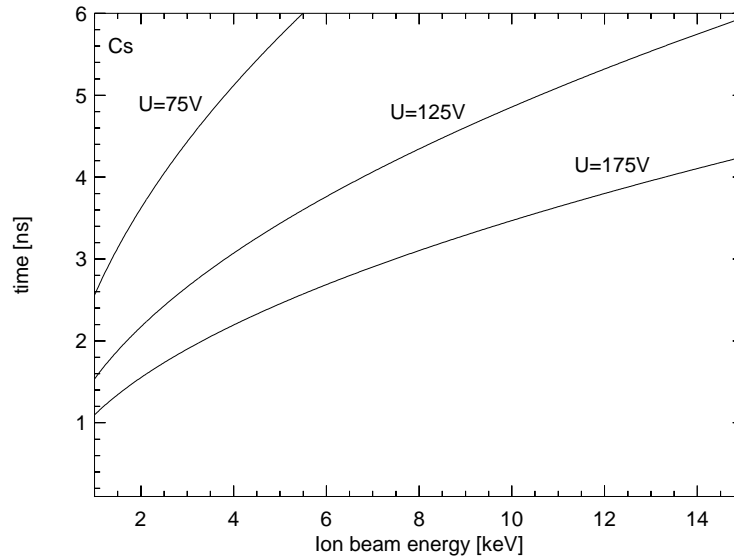


Figure 3.34: Packet length for Cs^+ ions for an energy range from 1 to 15 keV for various deflection plate voltages.

Different path lengths in lenses

In order to focus the ion beam onto the sample two lenses are mounted between the ion gun and the sample. The first one focuses the beam onto a collimator over which the beam is chopped in order to obtain pulses. The second lens is needed to focus the ion pulses on the sample. Hence, ions can take different paths until they reach the sample, and the difference in the path lengths leads to the time uncertainty t_p assuming that all ions have the same energy.

Figure 3.35 shows a very schematic drawing of all the elements used to focus and collimate the ion beam. We can therefore crudely estimate what time uncertainty we obtain due to different path lengths. If we calculate the length of the path ions take which fly on the axis and the path ions take which always have the maximum distance possible to the axis we obtain an estimate for the difference. For lens 1 we assume a maximum distance of about 2 mm and for lens 2 about 1 mm. Calculating both paths we obtain a difference in the path lengths of $\sim 75 \mu\text{m}$. Since 5 keV Cs^+ ions have a velocity of $0.086 \text{ m}/\mu\text{s}$ (see figure 3.4b) the difference in the flight times is somewhat below 1 ns. For Cs^+ ions of more energy or ions with less mass the effect of different path lengths on the time resolution gets more and more negligible.

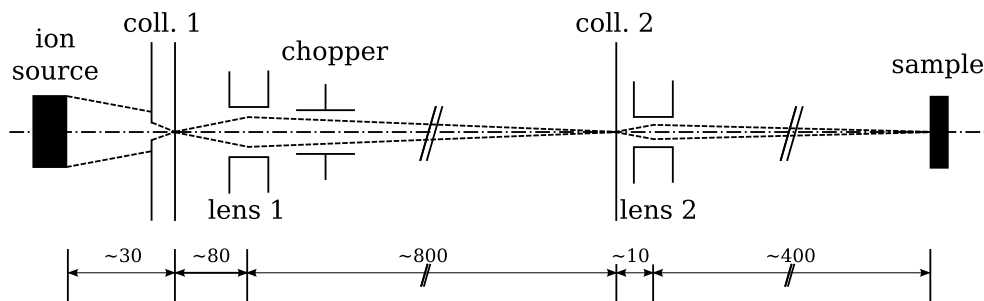


Figure 3.35: A schematic drawing of the different paths the ions can take to reach the sample. The sketch is not drawn to scale. Ions which fly along the axis of the spectrometer have the shortest path length and therefore the shortest time of flight. The longest path ions can take are indicated by the dashed lines.

3.6. First Experiments with MoVES

For the first test of the novel MoVE spectrometer it was decided to investigate the electron emission induced by Cs^+ ions from a Au surface. A series of experiments was conducted for different primary particle energies and various settings of the magnetic and electric field. The experiments were mainly performed in order to calibrate and test the spectrometer. In this section some preliminary results are given.

3.6.1. Cs^+ induced electron emission from a Au surface

r-over-t histograms

In the magnetic field of the spectrometer electrons travel on a cyclotron trajectory from the sample to the MCP (compare section 3.3.6). Figure 3.36 presents a histogram where

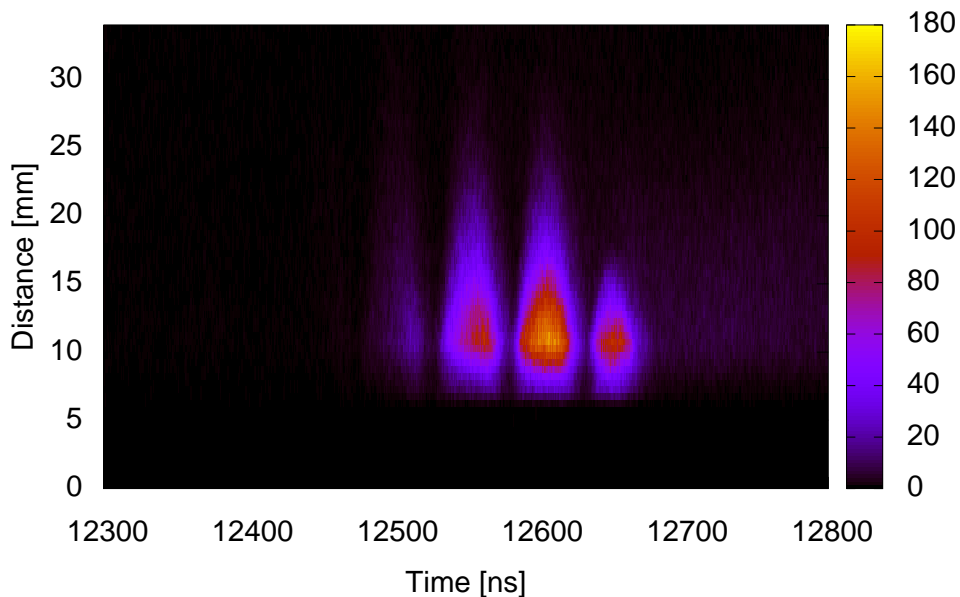


*Figure 3.36: In a so-called *r-over-t* histogram electrons events are mapped regarding their distance to the MCP center and the time, here for a magnetic field of 0.7 mT. The “peaks” correspond to times where the electrons establish the maximum distance to the spectrometer axis only determined by the intensity of the magnetic field.*

electron events are mapped regarding the distance r of the impact position to the MCP center and the time t . These histograms are the so-called *r-over-t* histograms. For this

measurement the magnetic field was set to ~ 0.7 mT. The cyclotron time $t_c = 2\pi m_e/eB$ is only dependent on the magnetic field. Therefore, all electron trajectories regardless of the electron energy and emission direction cross the spectrometer axis at the same time. In addition, all electrons establish their maximum distance to the spectrometer axis at the same time. This periodic behaviour can be clearly seen in figure 3.36. At the times $(n + 1/2)t_c$ peaks can be observed in the r -over- t histogram, while at nt_c no electrons are detected ($n \in \{1, 2, 3, \dots\}$). For values of r up to 7 mm no electron detection takes place due to the hole and the dead zone around this hole.

From the r -over- t histogram the cyclotron time t_c as well as the magnetic field can be determined as explained in section 3.4.3. Here, the accuracy of the so determined magnetic field depends on the time resolution of the spectrometer ($\Delta B/B = \Delta t/t_c$). In case a good time resolution can be achieved ($\Delta t \sim 1$ ns) the spectrometer can be used to determine the magnetic field with a satisfying resolution as well. This can be exploited to determine the dependence of the magnetic field on the Helmholtz-coil current (see section 3.3.3). In addition, a series of measurements with different magnetic fields allows to determine the time of the ion-solid impact with the time resolution of the spectrometer as explained in section 3.4.3.

The r -over- t histogram also allows to estimate the time resolution of the spectrometer, i.e. the width of the ion pulse. It is assumed that the pulse width is the dominant factor of the time resolution. By comparison of figure 3.36 to calculated histograms, where the ion pulse distribution was varied, it was found that the pulse width for this measurement is between 5-10 ns. The main limiting factor was found to be the ion chopper, which was not designed to chop very slow ions. This drastically decreases the energy resolution of this spectrometer where less than 2 ns were required initially. Therefore, all the results presented in the further sections are only to be considered preliminary, since a satisfying time resolution was never obtained. Still, the r -over- t histograms clearly show that the spectrometer works in principle, but further work is necessary to reduce the pulse width and therefore improve the time resolution to an acceptable value.

Energy spectrum of secondary electrons

In section 3.3.7 it was explained how the kinetic properties of the electrons at the time of emission are determined using the impact position x, y and the time of flight t_f . A polycrystalline Au sample was used for all experiments and therefore no azimuthal dependency is expected. In figure 3.37 a histogram is presented where the electron events are mapped regarding their determined energy and emission angle ϑ . Here, the magnetic field intensity was 0.7 mT, the sample was grounded, the last electrode was set to 5 V and the second grid to 2 V. The spectrum clearly resembles the transmission plots in section 3.3.9.

If the spectrum is integrated over the emission angle ϑ we obtain an energy spectrum of the ion-induced electrons (see figure 3.38). The energy distribution resembles the

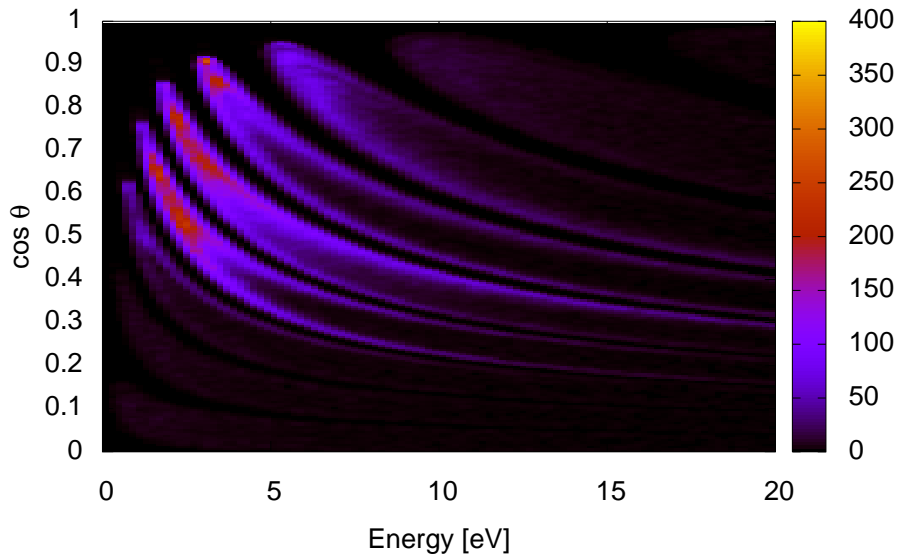


Figure 3.37: In this histogram electron events are mapped using their emission angle ϑ and energy E . The histogram resembles the structure of the transmission function described in section 3.3.9. Here, we integrate over the azimuthal angle φ since there is no dependence on φ for polycrystalline Au.

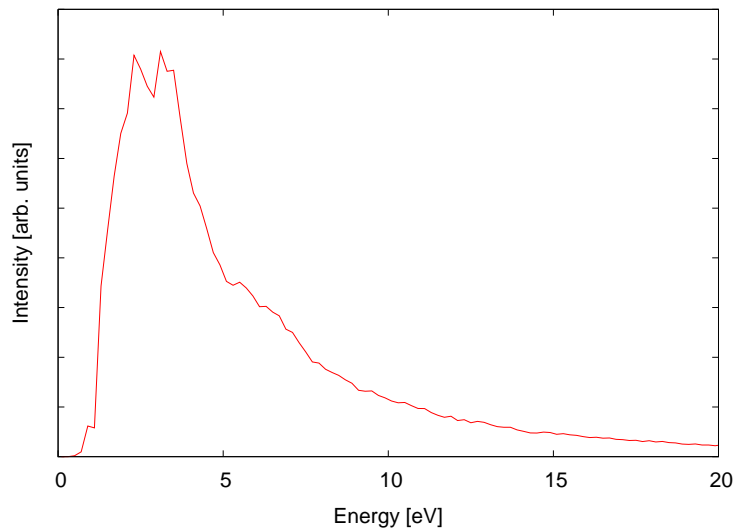


Figure 3.38: Energy distribution of ion induced electrons for Cs^+ on Au. Due to the low energy resolution for this measurement no feature of this spectrum can be verified. For energies below ~ 2 eV the spectrum yields no relevant data, since all electrons in this energy range end up in the hole region of the MCP.

spectra usually obtained in ion-induced electron spectroscopy. All the features seen in this spectra can not be verified due to the low energy resolution. In addition, it is possible that features like the peaks at ~ 3 eV and ~ 4 eV and the shoulder at ~ 7 eV are introduced during the integration of the transmission function. This energy distribution has no relevance for energies below ~ 2 eV since all electrons of this energy are not detected due the hole in the MCP. In order to investigate this energy range the magnetic field needs to be adjusted. Further investigations need to be done to correctly account for the transmission function.

Coincidence measurements

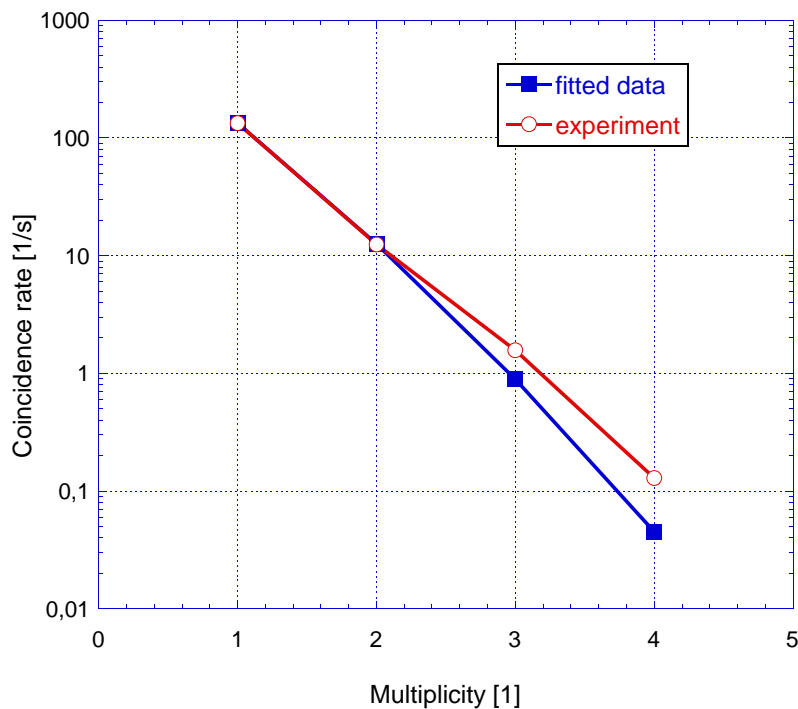


Figure 3.39: Experimentally determined number of n -electron coincidences per second compared to the theoretical model introduced in section 3.2.

From the same data used for the energy spectra shown above coincidence events can be investigated. Figure 3.39 presents the number of n -electron coincidence events per second. Note, that in this measurement over 10 two-electron events per second occurred. This is a considerably high number of coincidences taking into account that for APECS measurements (see section 1.2.3) the coincident rate was below 1 Hz at a synchrotron. This shows the potential of this spectrometer. The electron statistics were also fitted to the theoretical model presented in section 3.2, if a Poisson distribution for the emission process is assumed. There is a qualitatively good agreement between the theoretical

model and the experimental data. The average number of ions per pulse was determined to be ~ 0.1 . The average number of electrons emitted per ion or total electron yield γ was calculated to ~ 0.1 . The values of both quantities are in the expected range. Since there are no reliable results of ion-induced electron emission for Cs^+ on Au, γ could not be compared to existing data.

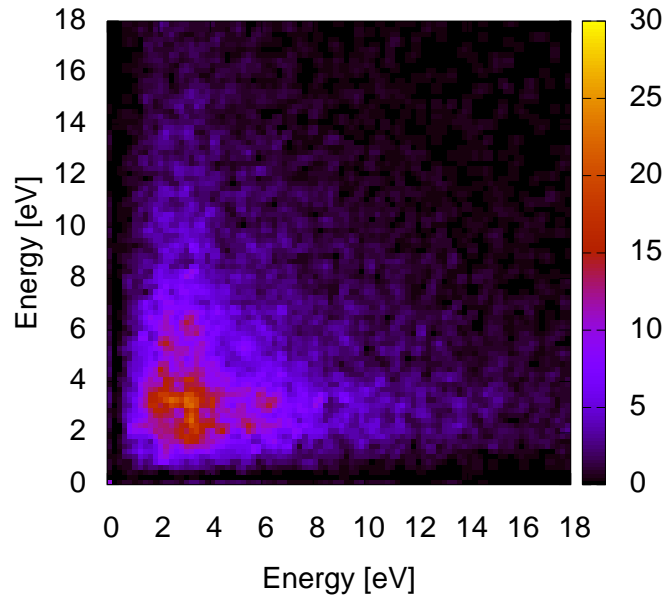


Figure 3.40: Energy coincidence spectra for 2-electron events.

Figure 3.40 shows an energy coincidence spectrum for two-electron events. Here, in case that exactly two electrons were detected, the event was mapped in a histogram using the energies of both electrons. Again, due to the low energy resolution no conclusion can be drawn from this energy spectrum. It should be mentioned though that this spectrum was taken in one hour which is only possible due the considerably high coincidence rate.

4. Conclusions and Outlook

Electron coincidence experiments on solids were conducted for electron emission induced by photons, electrons and ions. It is well known that coincidence experiments allow one to study various types of electron emission mechanisms, such as Auger or photoelectron emission, with a much greater level of discrimination [83, 69, 44, 57, 38, 99, 97, 67, 49, 52, 50]. However, the possibility to use coincidence measurements to study the transport of electrons between their point of emission and escape from the surface has been much less explored, although it is known since the beginning of coincidence measurements of solids [38]. In the present thesis the potential of coincidence measurements to obtain information on the transport of electrons travelling inside a solid is demonstrated.

An Auger Photoelectron Coincidence Spectroscopy (APECS) experiment on Si was conducted to verify a theoretical model considering the surface sensitivity of APECS. It was demonstrated that the emission depth range of individual photoelectrons can be discriminated by measuring them in coincidence with Auger electrons which lost a certain amount of energy.

Furthermore, electron induced electron coincidence spectroscopy experiments (so-called $(e, 2e)$ coincidence spectroscopy) were conducted on an Al (100) surface. Here, the secondary electrons were measured in coincidence with reflected electrons which experienced a characteristic loss either by exciting a surface or a bulk plasmon. If such coincidences are measured, the secondary electrons must originate directly from a plasmon decay. It was clearly demonstrated that such coincidences do indeed exist for both surface and bulk plasmons. From the comparison of experimental data to Monte Carlo simulations it was concluded that most plasmons decay into a single electron-hole pair. This experiment was only possible since a nearly free electron material such as Al exhibits very pronounced loss features, i.e. the surface and bulk plasmon loss peak in the reflected electron energy spectrum can be easily distinguished.

For materials with a more complicated electronic structure, unravelling the secondary electron emission process would imply coincident energy resolved measurements of the secondary electron spectrum, for many energies in the loss spectrum covering the interesting energy loss range between 0 and ~ 50 eV. With a conventional coincidence spectrometer consisting of two separate analyzers, such as the one used for the $(e, 2e)$ -measurements mentioned above, acquiring the required statistics at *one* loss energy takes about a *month* of net measurement time. Therefore, new experimental approaches need to be developed in order to achieve the stated goal.

For this purpose, a novel magnetic field time-of-flight spectrometer was designed and built, where considerably higher coincidence rates are achieved. Here, all electrons emitted into the hemisphere above the sample are projected onto a position sensitive detector by a magnetic field. The impact position and the time of flight are recorded and used to determine the momenta of the electrons at the time of emission, making the spectrometer kinematically complete. Since the spectrometer consists of a detector with a solid angle of detection of 2π for up to 14 emitted electrons, coincidence measurements with unprecedented high coincidence count rates are achievable in this way. The incident radiation traverses the spectrometer along its axis, making it possible to use the spectrometer with charged particles as projectiles. In this way, an $(e, 2e)$ coincidence experiment is also possible for materials which do not exhibit pronounced inelastic loss features.

First experiments on this spectrometer for Cs^+ ions on Au showed that the spectrometer works in principle. It was shown that the experimental data recorded can be used to calibrate the spectrometer. The energy resolution of the spectrometer was unsatisfactorily low due to the insufficient time resolution of the pulsed ion source. There are some possibilities to improve the time resolution of the chopped ion beam. The main problem is the low velocity of the ion beam, since slow heavy Cs^+ ions were used. The thermionic ion source used for this experiment can be assembled with Alkali ions of less mass, e.g. Li or Na. The velocity of these ions would be considerably higher than for Cs^+ at the same energy and it is assumed, that better time resolution can be achieved. Alternatively, the ion chopper could be redesigned to take the low velocity of the ions into account.

A. Acknowledgement

The present work was carried out under supervision of Dr. Wolfgang S.M. Werner at the 'Institut für Allgemeine Physik' - research group 'Surface and Plasma Technology' - of Vienna Technical University. I am very thankful to Dr. Werner for the valuable discussions throughout the course of this work, as well as his critical reading of this manuscript and for introducing me to the field of surface science and electron spectroscopy.

I also acknowledge the help and support of Dr. Herbert Störi, the head of this research group, as well as of the other group members. I am very grateful to the former head of the department, Dr. Hannspeter Winter, for his contribution to this work and his enthusiasm for this new technology.

Paul Berlinger's support, especially concerning all things electrical and electronic, were invaluable for the construction of the MoVE spectrometer. I am also very thankful to Wolfgang Beck, Rainer Gärtner and Herbert Schmidt of the workshop whose machining skills were an essential contribution to the experiment. I thank Dr. Peter Bauer for his suggestions and advice concerning the ion chopper.

Finally, I really appreciate all the support from my father and my sister over the last years. I am especially thankful to my wife Elisabeth for her assistance and encouragement during the years of study and I am very grateful to my son David who shows me every day what the spirit of research really is.

B. Acronyms

AES	Auger electron spectroscopy
ALOISA	Advanced Line for Overlayer, Interface and Surface Analysis
APECS	Auger photoelectron coincidence spectroscopy
CFT	Constant fraction discriminator
COG	Center of gravity
DDF	Depth distribution function
DLA	Delay–line–anode
EMFP	Elastic mean free path
FWHM	Full width half maximum
HMA	Hemispherical mirror analyzers
IMFP	Inelastic mean free path
KE	kinetic emission of electrons
MC	MonteCarlo
MCP	Micro–channel plate
MoVES	Momentum vector electron spectroscopy
NIM	Nuclear Instrumentation Methods
PE	Potential emission of electrons
PES	Photoemission spectroscopy
QDE	Quantum Detection Efficiency
RHEED	Reflection high energy electron diffraction
SE	Secondary electrons
TDC	Time–to–digital converter
TMFP	Transport mean free path
UHV	Ultra–high vacuum
XPS	X–ray photoelectron spectroscopy

C. Curriculum vitae

Personal:

Name: Werner Smekal
Date of birth: January, 28th 1974
Place of birth: Wien, Austria
Citizenship: Austria

Education:

1980 – 1984 Primary school, 1040 Wien
1984 – 1988 Gymnasium – BRG Waltergasse, 1040 Wien
1988 – 1993 Polytechnical Institute - TGM, 1200 Wien
1993 – 2001 Studies of “Technische Physik”, Vienna Technical University
1993 – Studies of “Technische Mathematik”, Vienna Technical University
2002 – 2003 Civil service at the “Lebenshilfe Wien”
2003 – 2007 Ph.D. Student, Vienna Technical University

Persönliches:

Name: Werner Smekal
Geburtsdatum: 28. Jänner 1974
Geburtsort: Wien, Österreich
Staatsbürgerschaft: Österreich

Bildungsweg:

1980 – 1984 Volksschule, 1040 Wien
1984 – 1988 Gymnasium – BRG Waltergasse, 1040 Wien
1988 – 1993 Höhere Technische Lehranstalt - TGM, 1200 Wien
1993 – 2001 Diplomstudium der “Technischen Physik”,
Technische Universität Wien
1993 – Diplomstudium der “Technischen Mathematik”,
Technische Universität Wien
2002 – 2003 Zivildienst bei der “Lebenshilfe Wien”
2003 – 2007 Doktoratsstudium, Technische Universität Wien

Bibliography

- [1] E.V. Alonso, R.A. Baragiola, J. Ferrón, M.M. Jakas, and A. Oliva-Florio. z_1 dependence of ion-induced electron emission from aluminium. *Phys. Rev.*, B22:80–87, 1980.
- [2] U. Amaldi, A. Egidi, R. Marconero, and G. Pizzelly. *Rev. Sci. Instr.*, 40:1001, 1969.
- [3] K.L. Aminov and J.B. Pederson. *Phys. Rev.*, 63:125412, 2001.
- [4] P. Auger. *J. Physique Radium*, 6:205, 1925.
- [5] F. Aumayr and H. Winter. Potential electron emission from metal and insulator surfaces. *Springer Tracts in Modern Physics*, 225:79–112, 2007.
- [6] J. M. B. Bakker. A beam-modulated time-of-flight mass spectrometer. i. theoretical considerations. *Journal of Physics E: Scientific Instruments*, 6(8):785–789, 1973.
- [7] J. M. B. Bakker. A beam-modulated time-of-flight mass spectrometer. ii. experimental work. *Journal of Physics E: Scientific Instruments*, 7(5):364–368, 1974.
- [8] R.A. Baragiola, E.V. Alonso, and A. Oliva-Florio. Electron emission from clean metal surfaces induced by low-energy light ions. *Phys. Rev.*, B19:121–129, 1979.
- [9] R.A. Bartynski, E. Jensen, and S.L. Hulbert. *Phys. Scr.*, T41:168–174, 1992.
- [10] M. Bergsmann. Bau eines flugzeitspektrometers für energieverlustmessungen von ionen. Master’s thesis, Johannes Kepler University, Linz, Austria, 1995.
- [11] R. Bongeler, U. Golla, L. Kussens, M. und Reimer, B. Schendler, R. Senkel, and M. Spranck. *Scanning*, 15:1, 1993.
- [12] I.M. Bronstein and B.S. Fraiman. Nauka, 1969.
- [13] H. Bruining and J.M. de Boer. *Physica*, V:17, 1938.
- [14] Y.Q. Cai, M. Vos, P. Storer, A.S. Kheifets, and I.E. McCarthy. *Phys. Rev.*, B51:3449, 1995.
- [15] R. Camelloni, A. Guardini-Guidoni, R. Tiribelli, and G. Stefani. *Phys. Rev. Lett.*, 29:618, 1972.

-
- [16] K.M. Case and P.F. Zweifel. *Linear Transport Theory*. Addison-Wesley, Reading, MA, 1967.
- [17] C.J. Tung , Y.F. Chen , C. M. Kwei and T.L. Chou. *Phys. Rev.*, B49:16684, 1994.
- [18] D. Coster and R.D.L. Kronig. A new type of auger effect and its influence on the x-ray spectrum. *Physica*, 2:13, 1935.
- [19] W. Czaja. *J. Appl. Phys.*, 37:4236, 1966.
- [20] D.A. Dahl. Simion for the personal computer in reflection. *Int. J. Mass Spectrom.*, 200:3, 2000.
- [21] M. Delaunay, M. Fehringer, R. Geller, D. Hitz, P. Varga, and HP. Winter. Electron emission from a metal surface bombardment by slow highly charged ions. *Phys. Rev.*, B35:4232–4235, 1987.
- [22] W. Demtröder. *Experimentalphysik 2 - Elektrizität und Optik*, volume 2.
- [23] C. Denton, J.B. Gervasoni, R.O. Barrachina, and N.R. Arista. *Phys. Rev.*, A57:4498, 1998.
- [24] D.R. Penn. Electron mean free path calculations using a model dielectric function. *Phys. Rev.*, B35:482, 1987.
- [25] A. Dubus, J. Devooght, and J.C. Dehaes. *Phys. Rev.*, B36:5110, 1987.
- [26] E.D. Palik. *Handbook of optical constants of solids*. Academic Press, New York, 1985.
- [27] H. Eder. *On Novel Mechanisms of Slow Ion Induced Electron Emission*. PhD thesis, Vienna University of Technology, Vienna, Austria, 2001.
- [28] H. Eder, F. Aumayr, P. Berlinger, H. Störi, and HP. Winter. Excitation of plasmons by impact of slow ions on clean mono- and polycrystalline aluminum. *Surf. Sci.*, 472:195–204, 2001.
- [29] A. Einstein. *Ann. Physik*, 17:132, 1905.
- [30] T.E. Everhart, N. Saeki, R. Shimizu, and T. Koshikawa. *J. Appl. Phys.*, 47:2941, 1976.
- [31] M. Galassi, J. Theiler, B. Gough, G. Jungmann, M. Booth, and F. Rossi. *GNU Scientific Library Reference Manual - Revised Second Edition (v1.8)*. August 2006.
- [32] E. Galutschek, R. Trassl, E. Salzborn, F. Aumayr, and Hp Winter. Compact 14.5 ghz all-permanent magnet ecris for experiments with slow multicharged ions. *Journal of Physics: Conference Series*, in print, 2007.
-

-
- [33] J.P. Ganachaud and M. Cailler. *Surf. Sci.*, 83:498, 1979.
- [34] J.P. Ganachaud and M. Cailler. *Surf. Sci.*, 83:519, 1979.
- [35] R. Gotter, A. Ruocco, A. Morgante, D. Cvetko, L. Floreano, F. Tommasini, and G. Stefani. The aloisa end station at elettra: a novel multicoincidence spectrometer for angle resolved apecs. *Nuclear Instruments and Methods in Physics Research Section A: Accelerators, Spectrometers, Detectors and Associated Equipment*, 467-468(Part 2):1468–1472, July 2001.
- [36] A. Gumbsch. Aufbau eines flugzeitdetektionssystems für die “momentum vector spectroscopy” (moves) zur untersuchung der ioneninduzierten sekundärelektronen-emission. Master’s thesis, Vienna University of Technology, Vienna, Austria, 2005.
- [37] H.W. Haak. *Auger-photoelectron coincidence spectroscopy: a study of correlation effects in solids*. PhD thesis, Rijksuniversiteit te Groningen University, Netherlands, 1983.
- [38] H.W. Haak, G.A. Sawatzky, and T.D. Thomas. Auger–photoelectron coincidence measurements in copper. *Phys. Rev. Lett.*, 41:1825, 1978.
- [39] H.W. Haak, G.A. Sawatzky, L. Ungier, J.K. Gimzewski, and T.D. Thomas. *Rev. Sci. Instrum.*, 55:696, 1984.
- [40] H.D. Hagstrum. Theory of auger ejection of electrons from metals by ions. *Phys. Rev.*, 96:336–365, 1954.
- [41] H.D. Hagstrum. Effect of monolayer adsorption on the ejection of electrons from metals by ions. *Phys. Rev.*, 104:1516–1527, 1956.
- [42] D. Hasselkamp, H. Rothard, K. O. Groeneveld, J. Kemmler, P. Varga, and Hp Winter. *Particle induced electron emission II*, volume 123/1992. Springer tracts in modern physics edition.
- [43] V. Heine. Pergamon, Oxford, 1960.
- [44] R. Hermann, S. Samarin, H. Schwabe, and J. Kirschner. *Phys. Rev. Lett.*, 81:2148, 1998.
- [45] H. Hertz. *Ann. Phys.*, 33:983, 1887.
- [46] N. Hilleret, J. Bojko, O. Grobner, B. Henrist, C. Scheuerlein, and M. Taborelli. Vienna, 2000.
- [47] S. Hüfner. *Photoelectron spectroscopy*. Springer, Berlin, Heidelberg, New York, 1995.
- [48] A. Jablonski, F. Salvat, and C.J. Powell. *J. Phys. Chem. Ref. Data*, 33:409, 2004.
-

-
- [49] E. Jensen, R.A. Bartynski, R. Garrett, S.L. Hulbert, E.D. Johnson, and C.C. Kao. Origin of the low-energy tail in the $al_2, 3v$ auger spectrum studied with apecs. *Phys. Rev.*, B45:13636, 1992.
- [50] E. Jensen, R.A. Bartynski, S.L. Hulbert, and E.D. Johnson. *Rev. Sci. Instrum.*, 63:3013, 1992.
- [51] E. Jensen, R.A. Bartynski, S.L. Hulbert, E.D. Johnson, and R. Garrett. *Phys. Rev. Lett.*, 62:71, 1989.
- [52] E. Jensen, R.A. Bartynski, S.L. Hulbert, E.D. Johnson, and R. Garrett. Line narrowing in photoemission by coincidence spectroscopy. *Phys. Rev. Lett.*, 62:71, 1989.
- [53] D.C. Joy. *Scanning*, 17:270, 1995.
- [54] D.C. Joy. <http://pciserver.bio.utk.edu/metrology/download/E-solid/database.doc>, 2003.
- [55] K. Kanaya and M. Kawakatsu. *J. Appl. Phys.*, D5:1727, 1972.
- [56] M. Kanter. *Phys. Rev.*, 121:1677, 1961.
- [57] J. Kirschner, O.M. Artamonov, and A.N. Terekhov. *Phys. Rev. Lett.*, 69:1711, 1992.
- [58] L.M. Kishinevsky. Estimation of electron potential emission yield dependence on metal and ion parameters. *Rad. Effects*, 19:23–27, 1973.
- [59] G. Kowarik. Investigations on ion induced electron emission from fusion-relevant surfaces. Master's thesis, Vienna University of Technology, Vienna, Austria, 2007.
- [60] J. CH. Kuhr and H.J. Fitting. Monte carlo simulation of electron emission from solids. *J. Electron Spectrosc. Rel. Phen.*, 105:257, 1999.
- [61] H. Kurz, F. Aumayr, C. Lemell, K. Töglhofer, and HP. Winter. Neutralization of slow multicharged ions at a clean gold surface: Total electron yields. *Phys. Rev.*, A48:2182–2191, 1993.
- [62] H. Kurz, K. Töglhofer, HP. Winter, F. Aumayr, and R. Mann. Electron emission from slow hollow atoms at a clean metal surface. *Phys. Rev. Lett.*, 69:1140–1143, 1992.
- [63] G. Lakits, F. Aumayr, M. Heim, and HP. Winter. *Phys. Rev.*, A42:5780–5783, 1990.
- [64] L.D. Landau and E.M. Lifshitz. *Quantum Mechanics: Non Relativistic Theory*. Pergamom Press, Oxford, New York, 1977. 3rd edition.
-

-
- [65] Y. Lin and D.C. Joy. *Surf. Interface Anal.*, 37:895–900, 2005.
- [66] B. Lohmann and E. Weigold. *Phys. Rev.*, A86:139, 1981.
- [67] C.P. Lund and S.M. Thurgate. *Phys. Rev.*, B50:17166, 1994.
- [68] K. Mase, E. Kobayashi, and K. Isari. *Correlation Spectroscopy of Surfaces, Thin Films, and Nanostructures*. Wiley edition, 2004.
- [69] I.E. McCarthy and E. Weigold. Electron momentum spectroscopy of atoms and molecules. *Rep. Prog. Phys.*, 54:789, 1991.
- [70] E.J. McGuire. Atomic m-shell coster-kronig, auger, radiative rates, and fluorescence yields for ca–th. *Phys. Rev.*, A 5:1043, 1972.
- [71] L. Meitner. *Z. Phys.*, 17:54, 1923.
- [72] M.O. Krause. Atomic radiative and radiationless yields for K and L shells. *J.Phys.Chem.Ref.Data*, 8(2):307–327, 1979.
- [73] D.A. Moncrieff and P.R. Barker. *Scanning*, 1:195, 1976.
- [74] M. Ohno. *J. Electron Spectrosc. Relat. Phenom.*, 124:53.
- [75] E.S. Parilis, L.M. Kishinevsky, N.Yu. Turaev, B.E. Baklitzky, F.F. Umarov, V.Kh. Verleger, S.L. Nizhnaya, and I.S. Bitensky. Elsevier Science, 1993.
- [76] A. Pernalci and M. Cini. *J. Electron Spectrosc. Rel. Phen.*, 82:79, 1996.
- [77] N.M. Persiantseva, N.A. Krasil'nikova, and V.G. Neudachin. *Sov. Phys. JETP*, 49:530, 1979.
- [78] D.E. Ramaker, F.L. Hutson, N.H. Turner, and W.N. Mei. *Phys. Rev.*, B 33:2574, 1986.
- [79] L. Reimer and C. Tolkamp. *Scanning*, 3:35, 1980.
- [80] O. W. Richardson. *The Emission Of Electricity From Hot Bodies*. Longmans Green And Company, 1916.
- [81] G.A. van Riessen. *Auger photoelectron coincidence spectroscopy: implementation of parallel detection and surface studies*. PhD thesis, Murdoch University, Perth, Western Australia, 2005.
- [82] R.H. Ritchie. *Phys. Rev.*, 106:874, 1957.
- [83] A.L. Ritter, J.R. Dennison, and R. Jones. Spectral momentum density of amorphous carbon from (e,2e) spectroscopy. *Phys. Rev. Lett.*, 53:2054, 1984.
- [84] D. Roptin. PhD thesis, University of Nantes, Nantes, France, 1975.
-

-
- [85] M. Rösler and W. Brauer. *Phys. Stat. Sol.*, 148:213, 1988.
- [86] M. Rösler and W. Brauer. Theory of electron emission from nearly-free-electron metals by proton and electron bombardment. *Springer Tracts in Modern Physics*, 122:1–65, 1992.
- [87] A. Ruocco, M. Milani, S. Nannarone, and G. Stefani. *pr*, B59:13359, 1999.
- [88] S. Tanuma, C.J. Powell and D.R. Penn. *Surf. Interface Anal.*, 21:165, 1994.
- [89] J. Schou. Transport theory for kinetic emission of secondary electrons from solids. *Phys. Rev.*, B22:2141–2174, 1980.
- [90] R. Shimizu. *J. Appl. Phys.*, 45:2107, 1974.
- [91] H.L. Skriver. Springer, New York, 1984.
- [92] W. Smekal, W.S.M. Werner, and C.J. Powell. Simulation of electron spectra for surface analysis (sessa): a novel software tool for quantitative auger-electron spectroscopy and x-ray photoelectron spectroscopy. *Surf. Interface Anal.*, 37:1059–1067, 2005.
- [93] V.V. Sobolev. *A Treatise on radiative transfer*. van Nostrand, Princeton, NJ., 1963.
- [94] G. Stefani, S. Iacobucci, A. Ruocco, and R. Gotter. Electron–electron coincidence spectroscopies at surfaces. *J. Electron Spectrosc. Rel. Phen.*, 127:1–10, 2002.
- [95] E.A. Stern and R.A. Ferrel. *Phys. Rev.*, 120:130, 1960.
- [96] P. Storer, S.A.C. Clark, R.C. Caprari, M. Vos, and E. Weigold. *Rev. Sci. Instr.*, 65:2214, 1994.
- [97] S.M. Thurgate. *Surf. Interface Anal.*, 20:627–636, 1993.
- [98] S.M. Thurgate and Z.-T. Jang. *Surf. Sci.*, 466:L807, 2000.
- [99] S.M. Thurgate, B. Todd, B. Lohmann, and A. Stelbovics. *Rev. Sci. Instrum.*, 61:3733–3737, 1990.
- [100] P. Unsworth, J.E. Evans, P. Weightman, A. Takahashi, J.A.D. Matthew, and Q.C. Herd. *Phys. Rev.*, B 54:286, 1996.
- [101] P.A.W. van der Heide. *Nucl. Instr. Meth. Phys. Res.*, B229:35–45, 2005.
- [102] M. Vicanek. *Surf. Sci.*, 400:1–40, 1999.
- [103] M. Vos and I.E. McCarthy. *Rev. Mod. Phys.*, 67:713, 1995.
-

-
- [104] M. Vos, P. Storer, Y.Q. Cai, A.S. Kheifets, and I.E. McCarthy. *J. Phys. Condens. Matter*, 7:279, 1995.
- [105] E. Weinryb and J. Philibert. *Comp. Rend. Acad. Sci.*, 258:4535, 1964.
- [106] W.S.M. Werner. *Surface Analysis by Auger and Photoelectron Spectroscopy*. IM-Publications, Chichester, UK, 2003.
- [107] W.S.M. Werner. Photon and electron induced electron emission from solid surfaces. *Springer Tracts in Modern Physics*, 225:39–77, 2007.
- [108] W.S.M. Werner and P. Schattschneider. On the energy dissipation process in incoherent electron scattering. *J. Electron Spectrosc. Rel. Phen.*, 143:65–80, 2005.
- [109] W.S.M. Werner, W. Smekal, H. Störi, HP. Winter, G. Stefani, A. Ruocco, F. Offi, R. Gotter, A. Morgante, and F. Tommasini. Emission–depth–selective auger photoelectron coincidence spectroscopy. *Phys. Rev. Lett.*, 94:038302, 2005.
- [110] W.S.M. Werner, W. Smekal, C. Tomastik, and H. Störi. *Surf. Sci.*, 486:L461, 2001.
- [111] W.S.M. Werner, H. Störi, and HP. Winter. *Surf. Sci.*, 518:L569, 2002.
- [112] N.R. Whetten. Academic Press, New York, 1962.
- [113] H. Winter and HP. Winter. Classical model of kinetic electron emission near threshold induced of atomic projectiles on a free–electron gas metal. *Europhys. Lett.*, 62:739–745, 2003.
- [114] D.B. Wittry. Hermann, Paris, 1966.
- [115] J.L. Wiza. Microchannel plate detectors. *Nucl. Instr. and Meth.*, 162:587–601, 1979.
- [116] W.S.M. Werner. Partial intensity analysis for quantitative electron spectroscopy. *Surf. Interface Anal.*, 23:737, 1995.
- [117] W.S.M. Werner. Slowing down of medium energy electrons in solids. *Phys. Rev.*, B55:14925, 1997.
- [118] W.S.M. Werner. Electron transport in solids of quantitative surface analysis. *Surf. Interface Anal.*, 31:141–176, 2001.
- [119] F. Yubero and S. Tougaard. *Phys. Rev.*, B46:2486, 1992.
- [120] Z-J. Ding. *Fundamental studies on the interactions of kV electrons with solids for application to electron spectroscopies*. PhD thesis, Osaka University, Japan, 1990.
-

List of Figures

1.1.	Schematic drawing which shows the relation between the energy levels in the solid (in this case a metal) and energy distribution of the electrons emitted due to photons of the energy $h\nu$. The kinetic energy E_{kin} of the electrons is zero at the vacuum level of the sample. Alternatively one can use the so-called binding energy of the electrons E_b , which in solids is generally referred to the Fermi level and in free atoms to the vacuum level. For the emitted electrons the photoelectric equation $E_{kin} = h\nu - E_b(i) - \phi$ is valid [47].	4
1.2.	Emission of a $KL_{2,3}L_{2,3}$ -Auger electron. The discrete energy levels are represented by the horizontal lines. A core electron is emitted from the atom due the interaction with the energetic incoming electron or X-ray radiation. A possible process for the decay of the excited atom is the Auger transmission: an electron from a higher energy level fills the hole in the core level and the energy difference between the level is transferred to another electron of the same level. This electron is transferred to a higher energy level or, if the energy transfer is sufficient, is emitted from the atom [36].	6
1.3.	Relative probability of K -shell and L_3 -subshell fluorescence compared to the competing Auger process as a function of atomic number Z . For low Z the Auger transition is dominant [72].	6
1.4.	Double-differential APECS spectrum for two model peaks, which were simulated with Monte Carlo simulation using the straight line approximation. Surface excitations were neglected in these calculations. Near the region of the peaks marked with a grey band the image was scaled by a factor of 0.1. On the right side a singles Auger spectrum and the coincidence spectra of the Auger peak with the photopeak (full line), with the first plasmon loss (dotted line) and with the second plasmon loss (dashed line) can be seen. At the bottom a singles photoelectron spectrum is depicted, as well as the coincidence spectra of the photopeak with the Auger peak (full line), with the first plasmon loss (dotted line) and with the second plasmon loss (dashed line) [111].	11

-
- 1.5. The effective countrate ν_{eff} is plotted against the ratio ν_A/ν_T , which is proportional to the incident flux. For a high incident flux ν_{eff} converges against a certain limit ν_{eff}^0 . Hence, there is no improvement in the countrate if the incident flux is increased above a certain limit (figure taken from [50]). 15
- 1.6. In panel (a) the photoexcitation process and the following Auger process of an inhomogeneous solid comprised of two types of atoms, A and B, are considered. Panel (b) shows the conventional photoemission spectrum consisting of valence level (VL), core level (CL), and Auger (CVV) electrons. Panel (c): If the CVV Auger region is measured in coincidence with particular core level photoelectrons (“A” and “B”) we only obtain the Auger spectrum from the decay of that core hole [9]. 17
- 1.7. Seven electron energy analyzer are installed in the experimental chamber. The rotation axis of the bimodal analyzers (6, 7) can be rotated in the z, y -plane, while the rotation axis of the axial analyzers (1–5) is identical to the chamber axis [94]. 19
- 1.8. The dash-dotted line shows the experimental Si-LVV singles spectrum. The spectrum where the background is removed via the the Partial Intensity Analysis [92] is shown by the open circles [109]. 20
- 1.9. Singles and coincidence spectra of the Si-2p peak are shown in this plot. The singles spectrum is represented by closed circles. Open triangles show the coincidence spectrum of the Si-2p photopeak with the Si-LVV Auger peak (marked with “peak” in fig. 1.8), while the open circles show the coincidence spectrum of the photopeak with the background of the Auger line (marked with “background” in fig. 1.8). The SESSA software [92] was used to conduct model calculations represented by solid and dotted lines. The data were normalized at the peak maximum. An expanded view of the BG and PK spectra is shown in the inset [109]. 21
- 1.10. (a) Partial escape distribution, or depth distribution function (DDF), $\phi_{n_X}(z, \theta_0)$ for the Si $2p_{1/2}$ transition. These data were simulated by means of a Monte Carlo model [92] for normal x-ray incidence, and with the Auger and photoelectron detected at an off-normal emission angle of 60° , as indicated in the inset. (b) Same as (a), for Si-LVV Auger electrons. (c) Reduced double differential partial intensities for bulk inelastic scattering $\gamma_{n_X, n_A} = C_{n_X, n_A}/C_{n_X=0, n_A=0}$ calculated from the curves in (a) and (b) using Eq. 1.7. The dashed curve represents the Si $2p$ singles partial intensities for bulk scattering [109]. 22
-

- 2.1. (a) Contribution of different excitations mechanisms in Al are revealed for the secondary electron spectrum (in reciprocal Rydbergs) at a primary electron energy of 1 keV [85]: (1) excitation of core levels; (2) electron-electron scattering; (3) decay of plasmons. (4) is the sum of all contributions. (b) A comparison of different theoretical calculations [86, 25, 89, 60] of the secondary electron spectrum of Al for 1 keV primary electrons with experimental results [84, 30]. All curves are normalized to the maximum of the peak [107]. 27
- 2.2. Experimental results on the primary energy dependence of the number of secondary electrons emitted, i.e. the secondary electron yield, for Al compared to the “universal” yield curve. Data points represent values from experiments taken from several sources [79, 73, 11, 90, 56, 19, 105, 13, 55, 114, 112, 12, 46], which show substantial discrepancies. The “universal” yield is calculated from eq. 2.2 using $E_m = 0.4$ eV and $\delta_m = 2.05$ and is indicated by the solid curve [107]. 28
- 2.3. (a) shows a comparison of experimental and theoretical results of the differential cross section for atomic Hydrogen. The momentum density $|\phi(\epsilon, \mathbf{q})|^2$ was determined experimentally (data points) for several energies and arbitrarily normalized. It can be seen that the energy of the primary particles has no influence on the momentum density as expected. The exact theoretical solution is represented by the solid line and agrees well with the experiment [66]. In (b) the different momentum components involved in an $(e, 2e)$ -experiment are presented [103]. 30
- 2.4. Comparison between theoretical and experimental spectral momentum density for amorphous Si (top figure) and amorphous SiC (bottom figure). Top row: (a) is a grey-scale plot of the measured spectral momentum density of amorphous Silicon. The shading is proportional to the intensity. (b) is the calculated spectrum for polycrystalline Silicon. (c) shows the comparison of experimental and theoretical dispersion relations [104]. The bottom row presents a similar comparison of experimental and theoretical data for SiC. A band gap around 10 eV binding energy can be observed [14]. Figures taken from ref. [103]. 31
- 2.5. This drawing shows the apparatus used for the $(e, 2e)$ -coincidence experiment. The electron gun can provide electrons of an incident energy between 50 and 600 eV. The hemispherical electron analyzers have an angular resolution of 1.5° and an energy resolution of 400 meV (for a pass energy of 20 eV). The angle between surface normal and incident electrons is 30° . In the experiment presented in this work spectrometer A measures the elastic peak and the near energy loss region in specular reflection, while the secondary electrons are measured with spectrometer B. The angle between surface normal and the axis of spectrometer B is 60° . All devices are mounted in an UHV chamber. 34
-

-
- 2.6. Plot (a) shows the experimental singles spectrum of the the elastic peak and its inelastic tail for Al (100). The inelastic features are enlarged in the inset at the top left. The surface plasmon peak and the bulk plasmon peak can be clearly distinguished. The secondary electron energy distribution is presented in plot (b). At ~ 9 eV a shoulder can be recognized. The shape of the spectrum compares well to the spectra shown in figures 2.1a and 2.1b. 35
- 2.7. Experimental secondary electron spectrum (dashed curve) for 100 eV electrons incident on an Al (100) surface. The solid line represents the corresponding Reflection Electron Energy Loss Spectrum (REELS). The energy offset for the energy loss scale of the latter spectrum is the work function of the spectrometer, which is taken to be 5.5 eV. The open circles and diamonds represent the secondary electrons that are emitted in coincidence with the single volume and bulk plasmon loss features in the REELS. 36
- 2.8. Comparison of the experimental data with results of model calculations. Short dashed curve: experimental singles secondary electron spectrum. Solid curve: simulated secondary electron spectrum. Data points with error bars: experimental secondary electron spectra measured in coincidence with the surface (plot a) and volume loss features (plot b) in the REELS spectra. Long dashed curved: corresponding simulated coincidence secondary electron spectra. 38
- 3.1. In the left plot the probability for particles to cross the surface barrier are shown. The escape probability is shown as a function of the energy of the particle inside the solid ϵ and as a function of the kinetic energy outside the solid E . Both energies are set in relation to the work function ϕ_W . At the right a schematic drawing shows the basic kinetic relations of the particle movement inside and outside the solid (figures taken from [59]). 45
- 3.2. Schematic drawings of possible transitions of electrons for ions moving in front of a surface. Figure (a) shows resonant and quasi resonant transitions, while Auger transitions are shown in (b) – Auger neutralisation, (c) – Auger de–excitation and (d) – auto ionisation. Solid arrows indicate the direction of the transition. The valence band is depicted by the horizontal lines up to the Fermi Level E_F . W_ϕ is the work function. Energy level of the ions are shifted with decreasing distance to the surface due to image charge effects (Figure taken from [5]). 48
-

-
- 3.3. A schematic drawing of the novel momentum vector electron spectrometer (MoVES). Very short (~ 1 ns) ion pulses enter the spectrometer from the top and travel through the delay line anode shielded from high voltages by a tube. When the ions hit the sample, electrons are emitted which are forced on a cyclotron trajectory due to the magnetic field (produced by Helmholtz coils) while the electric field (generated by the electrodes) accelerates the electrons towards the MCP. Impact position on the MCP and the time of flight of the electrons are recorded. From these data the momentum of the electrons at the time of emission can be reconstructed. 56
- 3.4. In order to understand certain aspects of the spectrometer and to be able to estimate how much time particles need for a certain distance, the velocity of electrons and Cs^+ ions over an energy range is plotted. Note that different ranges of both velocity and energy are shown in the plots. The insets in the plots show the velocity dependence for the lower energy region respectively. 58
- 3.5. An infinitesimal part $d\mathbf{l}(\mathbf{R})$ of the loop with the current I and the radius R contributes $d\mathbf{B}$ at the position $\mathbf{a} = (x, 0, z)$ to the magnetic field according to the law of Biot-Savart (eq. 3.10). \mathbf{r} is the distance vector between $d\mathbf{l}$ and \mathbf{a} 60
- 3.6. Two coils in Helmholtz configuration. The distance between the coils is equal to the radius r of a coil. If the same current I flows in both coils in the same direction a homogeneous magnetic field will be produced in between. 61
- 3.7. Two coils ($R = 1.09$ m) are mounted in Helmholtz configuration with 84 windings each. Figure (a) shows the dependence of the magnetic field intensity B between the coils of the current I . Figure (b) depicts the magnetic field intensity B in dependence of the position. The current through one coil was 14.43 A and therefore a field of 1 mT was produced in the drift region. The homogeneity of the magnetic field in the drift region (0.25 m \times 0.18 m) for this configuration is below 0.1%. 63
- 3.8. The electric field of the electrodes was calculated with SIMION 7.0 [20]. For the calculation an overall potential difference of 30 V was chosen. The potential difference between two adjacent electrodes is of the same order of magnitude to obtain a homogeneous electric field. The bounds of the drift region perpendicular to the spectrometer axis was determined by the size of the MCP (indicated by the solid horizontal lines). 64
- 3.9. An electron with the initial momentum \mathbf{p} emitted from the sample is forced on a cyclotron trajectory if a magnetic field \mathbf{B} is applied in the drift region of the length l . The electric field \mathbf{E} accelerates the electron towards the MCP with the radius R_{MCP} . The impact position of the electron at the MCP is given by \mathbf{R} . If the time of flight t is a multiple of the cyclotron time t_c the electron passes the axis of the spectrometer shown with black dots at the directory. 65
-

- 3.10. Both Figures show projections of the electron trajectory on a plane parallel to the MCP. The electron hits the MCP at the location \mathbf{R} . r_c denotes the cyclotron radius of the electron, \mathbf{p}_\perp the transversal momentum and l_f the trajectory length in the projected plane. The angles indicated are described in the text. Figure (a) shows the case where the flight time t_f is less than half the cyclotron time t_c , while figure (b) depicts the case where $t_f > \frac{t_c}{2}$ 67
- 3.11. Notation if one (a) or two (b) electric fields are used for the spectrometer. 70
- 3.12. An electron passes the grid with an angle ϑ with respect to the grid normal. l is the grid spacing and d the thickness of the grid. The transmission of the grid decreases with ϑ 73
- 3.13. The shape of the MCP (black solid lines) has an influence on the transmission function. Projections of three possible kinds of electron trajectories are shown here. Such a trajectory represents electrons with the same cyclotron radius and all possible momenta p_\parallel along the spectrometer axis. Trajectory 1 is always outside of the MCP area, therefore there is no transmission. Electrons on trajectory 2 will most of the times hit the MCP, while some will end up in the hole of the MCP. This is determined by their energy and direction of emission. Electrons, which have sufficient momentum perpendicular to the spectrometer axis might miss the MCP (trajectory 3). For trajectory 4 only electrons are accepted which have about the maximum distance from the spectrometer axis. For these electrons a good energy resolution is obtained. 75
- 3.14. Transmission function $T(E, \vartheta)$ versus the cosine of the emission angle θ and the electron energy E . This particular transmission was calculated for an magnetic field of 1 mT and an electric field of 39.68 V/m. The size of the MCP ($R_{MCP} = 37$ mm, $R_{hole} = 7$ mm) and the length of the analyzer ($l = 0.262$ m) were taken into consideration. Since all electrons were accepted for this transmission function regardless their time of flight (compare 3.3.9) the structure of this transmission function is only based on the size of the MCP and its hole. 76
- 3.15. (a)-(c): Transmission function of the spectrometer for various magnetic fields from 9 to 11 G, while the electric field stays the same. (d): Cumulative transmission function if the magnetic field is changed periodically. θ is the polar emission angle. 79
- 3.16. (a)-(c): Transmission function of the spectrometer for various electric fields from 19.8 V/m to 79.4 V/m, while the magnetic field stays the same. (d): Cumulative transmission function if the electric field is changed periodically. θ is the polar emission angle. 80
- 3.17. This is a schematic drawing of the delay line anode used for this experiment. The DLA consists of three layers of wires u, v and w which provide redundant information for multi-hit capability. Due to the gap in the wiring of the DLA some parts of the MCP are only covered by two layers. 82

-
- 3.18. This histogram shows the occurrence of the sum $2t_e - (t_1 + t_2)$ for one layer. A Gaussian function is fitted to this distribution to estimate the mean value and the width (FWHM) of the distribution. Both values are needed for the resort algorithm to decide if signal at each end of one layer belong together. Similar histograms are obtained for all three layers. . . . 84
- 3.19. For a DLA with three layers the symmetry lines of the layers do not meet in one point in a real application. This offset is due to differences in cable lengths between the TDC and the DLA. The offset parameter can be determined during the calibration of the device. 85
- 3.20. Schematic drawing of the wiring of one of the DLA layers. At the time t_1 an electron cloud produced by the MCP hits the wire and causes two pulses to advance to each end of the wire. Since both pulses travel with the same speed, their distance from the point of creation is always equal (e.g. at the time t_2). The signal velocity f_u perpendicular to the wires is much smaller than the speed of electric signals in a conducting wire (which is close to the speed of light). At t_3 and t_4 the signals will be detected at the ends of the wire respectively. The time difference $t_3 - t_4$ together with the knowledge of f_u is used to determine the position x_u where the impact occurred (compare equation 3.48). g_u is the size of the gap for this layer. 87
- 3.21. During the calibration process four quantities (f_2, f_3, χ and γ) are varied in given ranges in a double loop. In the inner loop, for a certain set of χ and γ , f_2 and f_3 are set stepwise and the quality parameter is determined for every set. Plot (a) shows the resulting contour plot, from which a minimum $\bar{\delta}(\chi, \gamma)$ can be determined. $\bar{\delta}(\chi, \gamma)$ is now calculated for a certain range of χ and γ and plotted again in a contour plot (figure b). The minimum in this plot corresponds to the best possible choice of f_2, f_3, χ and γ 90
- 3.22. Plot (a) shows the dependence of the quality parameter δ from the acceptance level σ_c while other parameters were kept constant. In general it can be seen that the number of electron events (N_{e2}, N_{e3}) increases and the lateral resolution decreases with increasing σ_c . Plot (b) depicts how the quality parameter δ decreases and therefore the lateral resolution improves if signals are rejected which were produced close to the gap of a layer. From a time difference of 10 ns on the lateral resolution doesn't improve any further. 92
- 3.23. Electrons which hit the MCP close to the layer gaps are not reliably detected with the MCP/DLA combination used. The drop in countrate between -10 ns and 10 ns should normally be not experienced since the signals pass the gap in practically no time. Therefore signal pairs are only accepted if the time difference between them is larger than ~ 10 ns. . . . 93
- 3.24. Dependence of the cyclotron time t_c on the magnetic field B for field intensities below 0.5 mT. 93
-

3.25. Dependence of the cyclotron time t_c on the magnetic field B for field intensities from 0.5 mT to 2.0 mT.	94
3.26. Histograms of the distance of the impact position to the MCP center r over the time t for several magnetic fields (2 G, 4 G, 7 G and 10 G). At the times $t_c, 2t_c, 3t_c, \dots$ all electrons regardless their energy or emission direction cross the spectrometer axis. At the times $\frac{1}{2}t_c, \frac{3}{2}t_c, \frac{5}{2}t_c, \dots$ the electrons reach their maximum distance from the axis. From these series of histograms the cyclotron times for the various magnetic fields can be determined, as well the time at which ion–solid interaction takes place.	95
3.27. In order to determine where the axis of the spectrometer crosses the MCP impact position contour plots are generated where the z value for a position is 0 if the number of hits is below a certain threshold or 1 otherwise. The center of gravity of the obtained areas are determined for several thresholds (here, in plot (a) the threshold is 48 and in (b) 19). The average of the COGs is an estimate of the spectrometer axis position. For this experimental data set the average COG is at $x = 1.2$ mm and $y = -1.5$ mm.	97
3.28. All possible ion beam profiles are shown depending on the time when the electric field is switched. For the various cases in the bottom left corner the electric field over time is shown. Ions get through the slit for the cases b, c and d , while for a and e the beam is completely deflected. The boundary cases b and d determine the packet length according to the time interval between them (figure take from [6]).	102
3.29. Nomenclature used in the theory of ion bunch production. The chopper geometry and the beam properties are indicated in figure (a). Figure (b) shows the electric field over time. t_1, t_2 and t_3 are directly related to the velocity of the incoming particle. The clamping time t_4 only depends on the electronics and the capacity of the plates [6].	104
3.30. Packet length for ${}^6\text{Li}^+$ ions for an energy range from 1 to 15 keV for various deflection plate voltages.	105
3.31. Packet length for Na^+ ions for an energy range from 1 to 15 keV for various deflection plate voltages.	105
3.32. Packet length for K^+ ions for an energy range from 1 to 15 keV for various deflection plate voltages.	106
3.33. Packet length for Rb^+ ions for an energy range from 1 to 15 keV for various deflection plate voltages.	106
3.34. Packet length for Cs^+ ions for an energy range from 1 to 15 keV for various deflection plate voltages.	107
3.35. A schematic drawing of the different paths the ions can take to reach the sample. The sketch is not drawn to scale. Ions which fly along the axis of the spectrometer have the shortest path length and therefore the shortest time of flight. The longest path ions can take are indicated by the dashed lines.	108

-
- 3.36. In a so-called r -over- t histogram electrons events are mapped regarding their distance to the MCP center and the time, here for a magnetic field of 0.7 mT. The “peaks” correspond to times where the electrons establish the maximum distance to the spectrometer axis only determined by the intensity of the magnetic field. 109
- 3.37. In this histogram electron events are mapped using their emission angle ϑ and energy E . The histogram resembles the structure of the transmission function described in section 3.3.9. Here, we integrate over the azimuthal angle φ since there is no dependence on φ for polycrystalline Au. 111
- 3.38. Energy distribution of ion induced electrons for Cs^+ on Au. Due to the low energy resolution for this measurement no feature of this spectrum can be verified. For energies below ~ 2 eV the spectrum yields no relevant data, since all electrons in this energy range end up in the hole region of the MCP. 111
- 3.39. Experimentally determined number of n -electron coincidences per second compared to the theoretical model introduced in section 3.2. 112
- 3.40. Energy coincidence spectra for 2-electron events. 113
-

List of Tables

3.1.	Not every layer and MCP signal can be detected due to the dead time of the electronics, signal overlapping or attenuation. Since the three layers provide redundant information this table contains the various cases for which signals can be partially reconstructed and for which the impact position of the electron can be calculated. In the columns u, v, w and MCP the number of signals detected are given for all possible cases. The reliability of the various cases is indicated in the column “notes”.	83
3.2.	This tables shows the values t_{sum} and σ_c for all three layers obtained by fitting a Gaussian function to an experimental data set as explained in the paragraph “Preparation of signals”. The consistence of these values needs to be checked for every experiment.	85
3.3.	From a real experimental data set $f1, f2, f3, \gamma$ and χ were determined via the calibration process. For the values presented in this table the quality parameter δ is at a minimum of 0.32.	89
3.4.	Histograms (see figure 3.26) for different magnetic field intensities (2 G, 4 G, 7 G and 10 G) were evaluated for the cyclotron time t_c and the time of ion–solid interaction t_s . For every measurement a series of possible t_s was determined. Since t_s doesn’t depend on the magnetic field, the time which can be found in every series (here, $t_s = 12370$ ns, bold) is the actual time where the ions hit the sample. All times in the table are in ns. . . .	96
3.5.	Packet length of a 5 keV Cs ⁺ ion pulse after a 1.3 m flight length for a range of energy uncertainties.	101